Search for Neutrino-induced Cascades in IceCube

Masterarbeit in Physik

von

Marcel Usner

angefertigt im

Physikalischen Institut
Nussallee 12
53115 Bonn

vorgelegt der

Mathematisch-Naturwissenschaftlichen Fakultät

der Universität Bonn

im

September 2012

Marcel Usner

E-Mail: usner@physik.uni-bonn.de

Erster Gutachter:

Herr Prof. Dr. Marek Kowalski

Zweiter Gutachter:

Herr Prof. Dr. Jochen Dingfelder

Abstract

The IceCube neutrino observatory at the geographical South Pole was built to measure high-energy neutrinos from cosmic sources. A total volume of about 1 km^3 of the deep and ultra-transparent Antarctic ice is instrumented with 5160 optical modules. In the IceCube event topology muon tracks are distinguished from cascades. Cascades have a signature which can in general be well separated from the background of atmospheric muons. Seen with a field of view of 4π, cascades can significantly contribute to the measurement of the diffuse neutrino flux. However, there are some muons which undergo catastrophic energy losses in the form of secondary cascades while traversing the detector. These catastrophic energy losses can contain a significant part of the overall deposited energy. Due to the relatively small amount of energy losses along the remaining muon track, these events look cascade-like and are the main background for neutrino-induced cascades at high cut levels. The study presented in this thesis introduces an event classification using the distribution of the specific energy losses. It is quantified by the novel cascade factor which relates the maximum to the total energy loss along a track. Both muons and cascades are reconstructed more precisely using the Igelfit as a new hybrid reconstruction tool which consists of a track and a cascade reconstruction algorithm. It yields the cascade factor, the zenith angle, the total deposited energy and a likelihood ratio of the track and cascade hypotheses as new cut parameters. These can be used to improve the signal and background cut efficiencies in the search for neutrino-induced cascades. Further potentially interesting applications of the cascade factor are neutrino flavor identification and composition studies of the cosmic ray flux.

Zusammenfassung

Das IceCube Neutrino-Observatorium am geographischen Südpol dient dem Nachweis hochenergetischer Neutrinos aus kosmischen Quellen. Dazu ist ein Volumen von ca. 1 km^3 des sehr transparenten antarktischen Eises mit 5160 optischen Modulen instrumentiert. In der Ereignistopologie wird zwischen Myonspuren und Kaskaden unterschieden. Kaskaden besitzen eine Signatur, die vom Untergrund der atmosphärischen Myonen gut zu unterscheiden ist. Sie können bei einem Gesichtsfeld von 4π einen wesentlichen Beitrag zur Erforschung des diffusen Neutrinoflusses liefern. Einige Myonen strahlen jedoch beim Durchgang durch den Detektor katastrophale Energieverluste in Form von Sekundärkaskaden ab, die einen signifikanten Anteil der im Detektor deponierten Gesamtenergie ausmachen. Aufgrund der vergleichsweise geringen Energiedeposition entlang der restlichen Myonspur sehen diese Ereignisse stark kaskadenartig aus und stellen somit den wesentlichen Untergrund für Neutrino-induzierte Kaskaden auf hohem Schnittlevel dar. Die in dieser Arbeit vorgestellte Studie führt eine Ereignisklassifizierung über die Verteilung der Energieverluste ein. Sie wird durch den neuartigen Kaskadenfaktor quantifiziert, der den maximalen Energieverlust in Relation zur totalen Energiedeposition setzt. Mithilfe einer neuartigen Hybridrekonstruktion, die sich aus einer Spur- und Kaskadenrekonstruktion zusammensetzt, können sowohl Kaskaden wie auch Myonen mit verbesserter Präzision rekonstruiert werden. Daraus erhält man den Kaskadenfaktor, den Zenitwinkel, die totale Energiedeposition und ein Likelihood-Verhältnis bezüglich der Spur- und Kaskadenhypothesen als potentielle neue Schnittparameter. Diese können für verbesserte Signal- und Untergrundeffizienzen bei der Suche nach Neutrino-induzierten Kaskaden verwendet. Weitere potentiell interessante Anwendungsgebiete sind die Neutrino Flavor Identifizierung und Studien zur Komposition der kosmischen Strahlung.

Contents

1. Introduction

In 1930, Wolfgang Pauli proposed the existence of the neutrino to explain how energy and momentum are conserved during beta decay [Pau30]. The neutrino is a very light, electrically neutral and weakly interacting elementary particle. Because of that it was only in 1956 that Clyde Cowan and Frederick Reines claimed its experimental discovery in the Poltergeist experiment [CLR$^+$56]. Ever since then the properties and interactions of neutrinos have been studied in a multitude of experiments at nuclear reactors and particle colliders.

The existence of cosmic rays, a constant flux of charged particles with energies up to 10^{20} eV coming from extra-terrestrial sources, was first discovered by Victor Hess in 1912 [Hes12]. In the course of the twentieth century, it became evident that interactions of cosmic rays with nuclei in the atmosphere cause particle showers in which the decay of pions and muons produces neutrinos. This atmospheric neutrino flux is one of the major neutrino sources on Earth. Along with the discovery of neutrinos and cosmic rays, it was assumed that there are also extra-terrestrial neutrino sources and thus began the advancement of neutrino astronomy.

Neutrinos from the Sun were first observed by Raymond Davis in the Homestake experiment in 1968 [DHH68]. Nineteen years later, neutrinos from the supernova SN1987A were observed by the Kamiokande II detector (among two other neutrino observatories) two to three hours before the first visible light reached the Earth [H$^+$87]. Neutrinos from the Sun and SN1987A are the only extra-terrestrial neutrinos that have been detected so far but it was a tremendous success to understand the interior of the respective sources.

One of the major goals of neutrino astronomy is to find the sources of highly energetic neutrinos which are assumed to be produced along with cosmic rays. Neutrinos are ideal cosmic messengers as depicted in Fig. 1.1. Cosmic rays such as protons are expected to be created in cosmic accelerators like gamma ray bursts or active galactic nuclei. On their way from the source to the Earth they can be deflected by strong magnetic fields from galaxy clusters. Hence, the detection of a cosmic ray proton on Earth does not disclose its source. Photons are not deflected by magnetic fields but may be absorbed by dust clouds. Neutrinos are assumed to be created along with cosmic rays in a *beam dump*, i.e. in interactions of protons with neutrons, photons and also heavier nuclei. Since neutrinos virtually only interact weakly, they travel over cosmic distances without being scattered or absorbed, pointing back to their sources.

However, neutrinos are hard to detect *because* they rarely interact with matter. In addition, cosmic source candidates such as gamma ray bursts do not happen often enough to be able to find them easily. Another approach to find cosmic sources is to study the *diffuse astrophysical neutrino flux* which is the sum of all cosmic sources without considering the direction. The flux is isotropic and expected to follow the cosmic ray energy spectrum. Since high-energy neutrino sources are generally located at cosmic distances from Earth, the expected flux is very low and its normalization unknown. The discovery potential is only at the highest energies where there is no background of muons and neutrinos created in the atmosphere in cosmic ray air showers.

The construction of kilometer-scale neutrino detectors has been motivated by the possibility of opening a new window on the universe by using neutrinos as cosmic messengers. Their size is needed to detect neutrinos at the highest energies in statistically significant numbers. The IceCube neutrino observatory is located at the geographic South Pole and utilizes 1 km^3 of the glacial ice in a depth between 1 500 m and 2 500 m to form a Cherenkov detector. The main goal is to detect astrophysical neutrinos. Muons leave long *tracks* in the detector due to the specific energy losses while passing through the ice whereas neutrinos induce particle showers, the so-called *cascades*. The optical modules of IceCube detect Cherenkov light created by secondary particles in these interactions. The challenges of neutrino detection are that the event rate is expected to be very low that there is a large background of atmospheric muons and atmospheric neutrinos. Atmospheric muons are restricted to the Southern Hemisphere, since muons cannot penetrate the Earth. Since IceCube has a field of view of 4π, the Earth can be used as a filter for atmospheric muons. Atmospheric neutrinos are distributed isotropically and thus a challenging background in the search for astrophysical neutrinos.

The work presented in this thesis aims to expand the set of analysis tools used for in search for neutrino-induced cascades. The *Igelfit* is a new hybrid reconstruction tool which combines existing track and cascade reconstruction algorithms. It employs the distribution of energy losses to classify the type of event via the *cascade factor*. This quantity relates the maximum energy loss to the total energy loss along a track. For the majority of muons the energy losses are evenly distributed along the track. However, some muons have catastrophic energy losses which can make up a significant amount of the total deposited energy. Compared to neutrino-induced cascades which only have a single energy deposition along the incident neutrino direction these muon events look cascade-like and are thus the major background at high cut levels. The Igelfit yields new potential cut parameters and increases the directional resolution of muons and neutrinos thus allowing a discrimination of signal and background.

In chapter 2 the theoretical foundation of high-energy neutrino astronomy is introduced. The cosmic ray flux and possible sources are discussed and the mechanisms of neutrino production, propagation and detection are explained. In chapter 3 the IceCube detector is sketched. In particular, the optical modules and the properties of the antarctic ice are discussed with respect to the detection of Cherenkov photons. The preconditions of the cascade and track analyses are explained in chapter 4. The different event signatures from the light distributions are used to distinguish the interaction type. The simulation properties and the existing reconstruction algorithms used for a first event selection prior to this study are explained in detail. In chapter 5 the implementation of the Igelfit as a new reconstruction tool is presented. The energy, vertex and directional resolutions are determined. In chapter 6 the results of the Igelfit are presented. A custom event selection is used to discuss signal and background efficiencies of the cut parameters derived from the Igelfit. Further applications utilizing the cascade factor with respect to neutrino flavor identification and composition studies of the cosmic ray flux are proposed in the last section. Finally, chapter 7 provides a summary and an outlook.

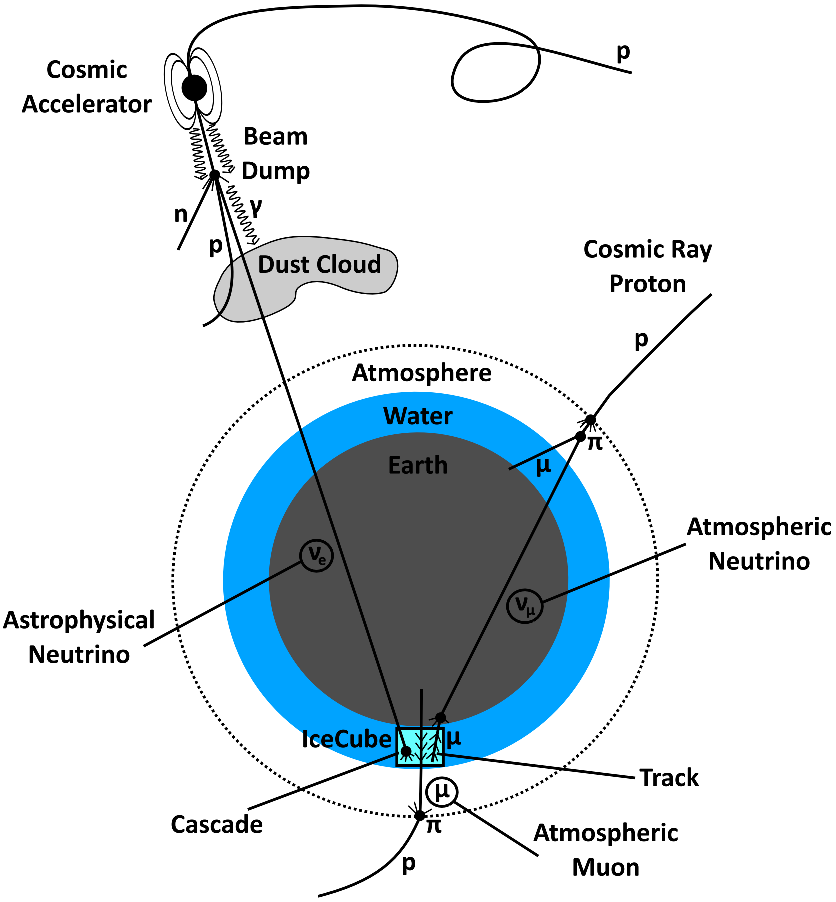

Figure 1.1: Overview of neutrinos as cosmic messengers with respect to the IceCube detector: Cosmic rays are accelerated and create hadrons, photons and neutrinos in a beam dump. Only neutrinos can travel cosmic distances without being deflected or absorbed in dust clouds. IceCube is located at the South Pole and detects neutrino-induced cascades and muon tracks. Muons and neutrinos created in the atmosphere in cosmic ray air showers are the background in the search for astrophysical neutrinos. The interactions shown for specific neutrino flavors are only exemplary.

2. High-Energy Neutrino Astronomy

Neutrino astronomy has been an advancing field of research for the last decades. So far, extra-terrestrial neutrinos from the Sun and from supernova 1987A were detected with large Cherenkov detectors [DHH68, H^+87]. The solar neutrino puzzle was solved by the existence of neutrino oscillations and the model of supernovae was established [MP98, GGM08, H^+87]. Atmospheric neutrinos have been measured to increasingly higher energies confirming the correlation to the cosmic ray flux and providing early hints of neutrino oscillations [Ice11]. However, there are still many unknown properties such as the absolute mass of the neutrinos and astrophysical neutrinos have yet to be detected [KAT01, HK10]. Due to their feeble interactions neutrinos are important astrophysical messengers, propagating over cosmic distances and pointing back to their source. However, astrophysical neutrinos can only be identified at very high energies where the background of atmospheric neutrinos is suppressed, implying the need for km^3-scaled detectors such as IceCube and KM3NeT [Ice01, Mig08].

This chapter covers the theoretical foundation for detecting high-energy neutrinos. The first section treats the cosmic ray flux and possible source candidates. The cosmic and the atmospheric neutrino fluxes are discussed in the second section. The variation of the flavor ratio due to neutrino oscillations is calculated at the source and the observer. The last section explains how to detect neutrinos. The interaction types and their cross sections are discussed. Different processes of energy losses for particles propagating through matter and the development of particle showers are needed to understand how the neutrino energy is measured. Since IceCube is a Cherenkov detector this chapter concludes with the generation of Cherenkov photons.

2.1 Cosmic Rays

In 1912, Victor Hess discovered an unexpected flux of charged particles hitting the Earth's atmosphere by conducting a series of balloon-flight measurements [Hes12]. Today it is well known that these *cosmic rays* (CR) mainly consist of protons and other atomic nuclei, whereas electrons and positrons make up only two percent [BG99]. Although the cosmic ray flux has been measured quite well, it is still not clear what the sources at different energies are.

2.1.1 Cosmic Ray Flux

The cosmic ray flux is well-described by a sequence of three power laws over a wide range of energies with $100\ \mathrm{GeV} \leq E \leq 100\ \mathrm{EeV}$ as shown in Fig. 2.1 [Hö3, Bec08]. The spectral index changes with the cosmic ray energy

$$\frac{\mathrm{d}N}{\mathrm{d}E} \sim \begin{cases} E^{-2.7} & \text{for} \quad 100\ \mathrm{GeV} \leq E < 1\ \mathrm{PeV}, \\ E^{-3.1} & \text{for} \quad 1\ \mathrm{PeV} \leq E < 1\ \mathrm{EeV}, \\ E^{-2.8} & \text{for} \quad E > 1\ \mathrm{EeV}. \end{cases} \tag{2.1}$$

The first power law follows a spectral index of -2.7 up to the so-called *knee* at an energy of $E_{\text{knee}} \simeq 1$ PeV. The energy spectrum softens to a spectral index of -3.1 up to the so-called *ankle* at an energy of $E_{\text{ankle}} \simeq 1$ EeV. Above the spectrum hardens to an index of -2.8 and at even higher energies above at $E_{\text{GZK}} \simeq 50$ EeV an indication of a cutoff is observed. It is assumed that this flux suppression is caused by the interaction of cosmic rays with the cosmic microwave background (CMB) via the Δ^+ resonance

$$\text{p} + \gamma_{\text{CMB}} \quad \rightarrow \quad \Delta^+ \quad \rightarrow \quad \text{p} + \pi^0 \quad \text{or} \quad \text{n} + \pi^+, \tag{2.2}$$

which was described by Greisen, Zatsepin and Kuzmin [Gre66, ZK66].

At low energies up to $E \leq 100$ TeV it is possible to measure the energy, charge and mass of the cosmic rays directly via satellite or balloon experiments, since the flux is large enough [HRR03]. From these measurements it is known that cosmic rays consist of nuclei with an element distribution that is consistent with the ones observed in the solar system [Per09]. At higher energies the flux is too low to be measurable with sufficient statistics by the relatively small detectors that can be carried by satellites or balloons. Instead cosmic rays at these energies are observed via extensive air showers (EAS). The primary particles interact with nuclei in the atmosphere and transfer their energy through subsequent collisions to a cascade of secondary particles. These cascades of charged particles are either measured directly or via the produced Cherenkov radiation by interacting with the atmosphere (see Sec. 2.3) by large detector arrays at sea level.[1] Cosmic rays at high energies above the knee are, therefore, only measured indirectly.

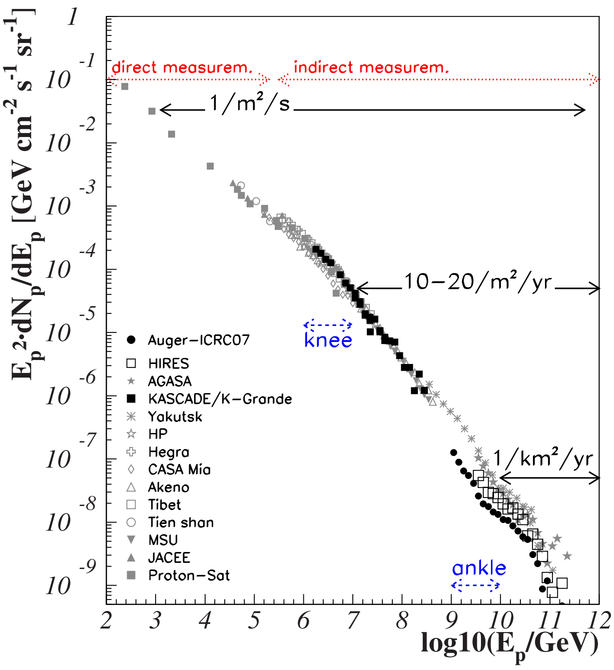

Figure 2.1: The cosmic ray flux: It follows a sequence of three power laws over a wide range of energy. Cosmic rays with energies below the knee are measured directly at a flux of about 1 $\text{m}^{-2}\text{s}^{-1}$. At energies above the knee measurements are indirect and the flux drops to about $10 - 20\ \text{m}^{-2}\text{yr}^{-1}$ and above the ankle to about 1 $\text{km}^{-2}\text{yr}^{-1}$ (Ref. [Bec08]).

---

[1] Example for direct air shower measurements are the KASCADE/KASCADE-Grande experiments in Karlsruhe [KAS12] and for air shower Cherenkov measurements the MAGIC I/II experiments on La Palma [MAG12].

2.1.2 Source Candidates

Depending on the energy there are many conceivable origins for cosmic rays. It is well known that the Sun produces a flux of low-energy protons and other nuclei. The origin of high-energy cosmic rays, however, is still unclear. It is assumed that they are generated in massive bulk flows of relativistic charged particles. These large currents produce high magnetic fields, powered by vast gravitational forces in the vicinity of neutron stars or black holes.

Fermi suggested a mechanism for particle acceleration by moving shock fronts [Fer49]. The process is similar to what happens in solar flares. The first order Fermi acceleration requires a shock front moving with a velocity v_f in a moving plasma. A charged particle with an initial energy E_0 enters the shock front from upstream to downstream and scatters collision-less at moving magnetic inhomogeneities before and after the shock front. With each scattering it gains an energy $\Delta E = \delta E_0$. After n scattering processes the particle can acquire a net gain in energy of $E = (1+\delta)^n E_0$. This process only works if the extension of the shock front is large compared to the gyro-radius of the charged particle in the magnetic inhomogeneities. Otherwise the particle would escape the acceleration process too quickly [Gai90].

The fractional energy gain δ depends linearly on the velocity of the moving plasma. The number of scattering processes n is dependent on the probability p_esc that the particle escapes again in the upstream direction.[2] It was shown by Fermi and Gaisser that this acceleration process indeed generates an energy spectrum following a power law

$$\frac{\mathrm{d}N}{\mathrm{d}E} = \frac{1}{p_\mathrm{esc}}\left(\frac{E}{E_0}\right)^{-1-\kappa} \qquad \text{with} \qquad \kappa \approx p_\mathrm{esc}/\delta \approx 1 + 4c_\mathrm{s}/v_\mathrm{f}. \tag{2.3}$$

The energy spectrum is anti-proportional to the escape probability, since the acceleration to higher energies needs many scattering processes. The coefficient κ is approximated in the kinetic gas theory if the shock velocity v_f is a few times larger than the speed of sound c_s in the plasma. If it is much larger the contribution of the second term can be neglected which gives $\kappa \approx 1$ and generates an E^{-2} spectrum according to Eq. (2.3).

It has been supposed that supernova remnants can account for an acceleration up to energies of a few hundred TeV [Per09] which compares to the observed cosmic ray flux of $E^{-2.7}$ below the knee. The difference could be explained by a steepening of the spectrum if the escape probability is energy dependent. Also, the observed spectrum appears softer due to a lack of high energy particles from the galaxy. Consequently, due to the Fermi acceleration of cosmic rays the astrophysical neutrino flux is modeled as an E^{-2} spectrum (see Sec. 2.2.1).

There are several suitable source candidates that are assumed to have shock fronts with large magnetic fields as discussed for the Fermi acceleration. These are supernova remnants (SNR) [K$^+$95], active galactic nuclei (AGN) [PS92] and gamma-ray bursts (GRB) [WRM08].

A supernova remnant consists of ejected material from the explosion of a supermassive star. It is bounded by an expanding shock wave which absorbs interstellar medium along the way. SNRs are assumed to account for the galactic cosmic rays below the knee [HK10].

An active galactic nucleus is a highly luminous region at the center of a galaxy. It emits energy in a broad electromagnetic spectrum from radio to gamma-rays. The radiation is assumed to be produced through the vast accretion of matter from nearby stars and gas clouds around a supermassive black hole at the center of the host galaxy. In contrast to GRBs, AGNs are persistent sources of highly luminous electromagnetic radiation [Pet97].

---

[2] In first order Fermi acceleration, the particle can only gain energy if it enters from upstream to downstream and escapes from downstream to upstream, whereas in second order Fermi acceleration the particle gains energy depending on the squared velocity of randomly moving magnetic inhomogeneities [Gai90].

A gamma-ray burst is a very bright and short flash of electromagnetic radiation associated with extremely energetic explosions in distant galaxies. They last from milliseconds to several minutes (typically just a few seconds) and are the most luminous events known to occur in the universe [Mal12]. The initial burst is usually followed by a longer-lasting *afterglow* with an emission spectrum in a longer waveband from X-ray to radio. There are hints that GRBs are associated with relativistic beams of intense radiation (jets) released during a supernova as a rapidly rotating, massive star collapses to form a neutron star or a black hole [BDM12].

The source candidates of the cosmic rays can be classified according to their energy. The argument is that charged particles only escape from the source if their gyro-radius is much larger than the size of the source. For example, the gyro-radius of a proton in the galactic magnetic field with an energy above the ankle exceeds the size of our galaxy. Therefore, it is assumed to originate from an extra-galactic source that accelerates to energies beyond 100 EeV. The maximum energy that a source of size L with a magnetic field B and a shock velocity $\beta = v/c$ (with c being the speed of light) can transfer onto a cosmic ray particle with charge number z is given by

$$E_{\text{max}} = \beta z \frac{B}{\mu\text{G}} \frac{L}{\text{km}} 10^{18}\ \text{eV}, \tag{2.4}$$

which was described by Hillas [Hil84]. This relation is depicted in Fig. 2.2. It shows that the low-energy cosmic rays are most likely produced in galactic supernova remnants, whereas the ultra high-energy cosmic rays are produced in neutron stars and GRBs. It is thus assumed that cosmic rays below the knee are of galactic origin and above the ankle of extra-galactic origin. Although cosmic rays in the intermediate region are most likely of galactic origin as well, their sources are still very uncertain [HK10].

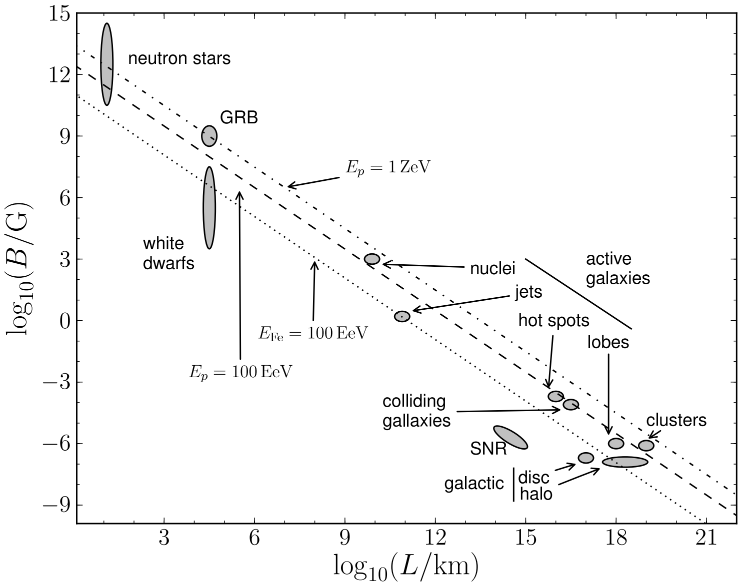

Figure 2.2: The Hillas plot: The relation between the magnetic field strength B and size L of a source is plotted for different source candidates. The isocontours show the maximal energy that an accelerator can generate for different nuclei. It supports the assumption that the low-energy cosmic rays are most likely produced in galactic supernova remnants whereas the ultra-high energy cosmic rays are produced in neutron stars and GRBs (Ref. [Pan11]).

2.2 Neutrino Sources

There are many different natural sources for neutrinos depending on their energies. Fig. 2.3 shows the spectra of the different contributions. A first classification can be made by separating the sources into a low-energy and a high-energy branch.

The low-energy neutrino sources contain a theoretical prediction from the relics of the Big Bang. Similar to the existence of the CMB, it is expected that there is a cosmic neutrino background (CνB) at an energy of $E_\nu \simeq 1.68 \cdot 10^{-4}$ eV from the decoupling of the neutrinos roughly two seconds after the Big Bang [Wei08]. Due to the very low energy, however, the CνB could not be measured yet.

It is well-known that the Sun produces low-energy neutrinos in vast numbers. Their energy depends on the production processes. Neutrinos from the pp-chain $4\mathrm{p}+2\mathrm{e}^- \rightarrow {}^4\mathrm{He}+2\nu_\mathrm{e}$ have an energy of $E_\nu \simeq 0.5$ MeV and from the boron decay ${}^8\mathrm{B} \rightarrow {}^8\mathrm{Be}^* + \mathrm{e}^+ + \nu_\mathrm{e}$ of $E_\nu \simeq 5$ MeV.

Neutrinos from core-collapse supernovae typically have energies of $E_\nu = 10 \ldots 100$ MeV. They are produced in the weak reaction $\mathrm{p} + \mathrm{e}^- \rightarrow \mathrm{n} + \nu_\mathrm{e}$ during the core-collapse and via thermal electron-positron collisions $\mathrm{e}^+ + \mathrm{e}^- \rightarrow \nu_\mathrm{e} + \bar{\nu}_\mathrm{e}$ as for burning stars. Supernova neutrinos are also produced in vast numbers but the difference is that the Sun generates a constant flux over time whereas neutrinos from supernovae are produced in short bursts.

The low-energy neutrinos from the Sun have been measured for many years now and are well understood. In addition, in this energy regime up to a few GeV neutrinos can be produced artificially in colliders and reactors. This allows a much more precise measurement of their properties and cross sections. At higher energies, however, neutrinos cannot be produced with current experiments so the only source is associated with cosmic accelerators.

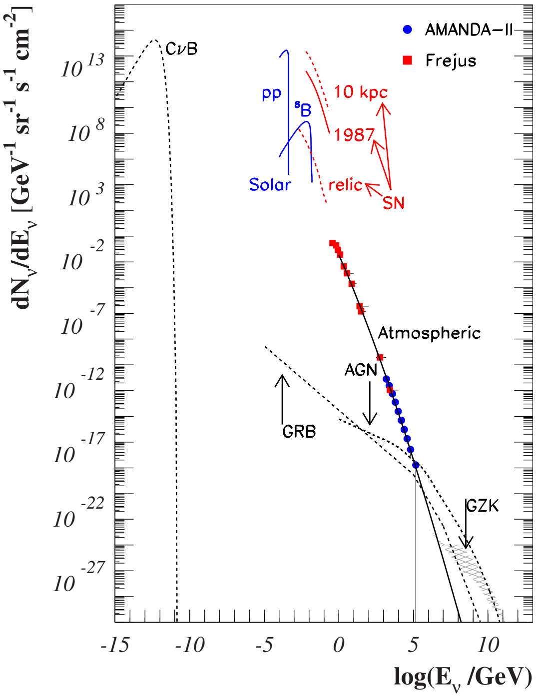

Figure 2.3: The neutrino flux: There are many neutrino sources over a wide range of energies. Compared to atmospheric neutrinos only astrophysical neutrinos from GRBs, AGNs or the GZK cutoff are assumed to reach the highest energies beyond 100 TeV (Ref. [HK10]).

The high-energy neutrino sources are separated into cosmic and atmospheric parts. Fig. 2.3 shows that the predicted sources for astrophysical neutrinos such as GRBs and AGNs are equivalent to the cosmic ray sources. The typical energy range is $E_\nu = 100\ \text{TeV} \dots 10^8\ \text{TeV}$. Atmospheric neutrinos are also associated with the cosmic ray flux, since they are generated in the reaction processes of cosmic rays with nuclei in the atmosphere. The typical energy range is $E_\nu = 10\ \text{GeV} \dots 100\ \text{TeV}$. Since both cosmic and atmospheric neutrinos are strongly associated with cosmic rays, the energy spectrum follows a similar sequence of power laws:

$$\frac{\mathrm{d}N}{\mathrm{d}E} \sim \begin{cases} E^{-2.0} & \text{for astrophysical neutrinos} \\ E^{-3.7} & \text{for conventional atmospheric neutrinos} \\ E^{-2.8} & \text{for prompt atmospheric neutrinos} \end{cases} \tag{2.5}$$

The astrophysical neutrinos are expected to follow a rather hard energy spectrum with a spectral index of -2.0 due to the association to the cosmic sources (c.f. Sec. 2.1.2). Depending on the interaction of the cosmic rays with the atmospheric nuclei there are different reaction products such as pions, kaons and heavier charmed mesons. The light mesons interact with the atmosphere before decaying which causes a flux damping and steepens the incoming cosmic ray spectrum of a spectral index from -2.7 to -3.7 for the produced neutrino spectrum. This is the so-called *conventional neutrino flux*. The heavy mesons have a very short lifetime and thus decay before interacting with the atmosphere. This generates a much harder neutrino flux with a spectral index of -2.8. Due to the immediate decay this is the so-called *prompt neutrino flux*. The cosmic neutrino flux and the atmospheric neutrino flux will be discussed in more detail in the following two sections.

2.2.1 Cosmic Neutrino Flux

The sources and production mechanisms of astrophysical neutrinos are still uncertain. However, when constructing models one assumes that these high-energy neutrinos are produced in cosmic accelerators in the so-called *beam dump scenario*. Cosmic rays, in particular protons, gain a vast amount of energy in cosmic accelerators (c.f. Sec. 2.1.2) and interact with the surrounding matter. Typical interaction processes are the scattering of protons, neutrons and photons which yield the generation of pions as the lightest meson.[3] The following processes describe the dominant proton-proton and proton-neutron interactions of cosmic rays with nuclei in plasma as it is expected to happen in supernova shocks [HK10]:

$$\mathrm{p} + \mathrm{p} \rightarrow \pi^0 + \mathrm{p} + \mathrm{p} \tag{2.6}$$
$$\mathrm{p} + \mathrm{p} \rightarrow \pi^+ + \mathrm{p} + \mathrm{n} \tag{2.7}$$

$$\mathrm{p} + \mathrm{n} \rightarrow \pi^- + \mathrm{p} + \mathrm{p} \tag{2.8}$$
$$\mathrm{p} + \mathrm{n} \rightarrow \pi^+ + \mathrm{p} + \mathrm{n} \tag{2.9}$$

The following processes describe the dominant proton-photon and neutron-photon interactions of cosmic rays with photons in radiation jets as it is expected to happen in GRBs:

$$\mathrm{p} + \gamma \rightarrow \Delta^+ \rightarrow \pi^0 + \mathrm{p} \tag{2.10}$$
$$\mathrm{p} + \gamma \rightarrow \Delta^+ \rightarrow \pi^+ + \mathrm{n} \tag{2.11}$$

$$\mathrm{n} + \gamma \rightarrow \Delta^0 \rightarrow \pi^0 + \mathrm{n} \tag{2.12}$$
$$\mathrm{n} + \gamma \rightarrow \Delta^0 \rightarrow \pi^- + \mathrm{p} \tag{2.13}$$

---

[3] The abundances of the produced mesons depend on the cross section and the available center of mass energy of the process. The generation of the pion is the most abundant process, since it is the lightest meson. Others such as kaons and D mesons are produced in smaller numbers but the reaction processes are similar.

The neutrinos are produced in the decays of the charged pions[4] and muons:

$$\pi^\pm \quad \rightarrow \quad \mu^\pm + \overset{(-)}{\nu}_\mu \tag{2.14}$$

$$\mu^\pm \quad \rightarrow \quad e^\pm + \overset{(-)}{\nu}_e + \overset{(-)}{\nu}_\mu \tag{2.15}$$

It can be argued that the energies between the generated neutrinos are evenly distributed if the muon does not lose energy due to interactions [HK10]. This is true if the muon interaction length is much longer than the decay length [Gai90]. This implies that the muon decays before interacting and that it transfers its initial energy to the neutrinos. Consequently, the neutrino flux follows the parental cosmic ray flux of E^{-2} in the source region, as argued in Sec. 2.1.1.

An upper limit for the expected neutrino flux for all flavors including the anti-neutrinos is given by the Waxman-Bahcall bound [WB99]. It is calculated by assuming a pure E^{-2} proton flux in the cosmic accelerators which is estimated by cosmic ray measurements above the ankle. Another assumption is that all protons generate charged pions through (2.11) which then decay into neutrinos through (2.14) and (2.15). The neutron produced in this interaction escapes the source and decays into a proton via the β-decay, thus yielding the observed cosmic ray flux. One arrives at an upper limit for the total astrophysical neutrino flux of

$$E^2\Phi = 6.8 \cdot 10^{-8}\ \mathrm{GeV\,cm^{-2}\,sr^{-1}\,s^{-1}}. \tag{2.16}$$

In addition to this flux estimation derived from CR measurements, a limit can also be obtained from measurements of the gamma-ray spectrum [HK10, Ice12a]. The argument is that all photons in a GRB interact via (2.10) and (2.11). The π^0 decay reproduces the gamma ray flux and the π^+ decay generates the neutrino flux. Taking the fractional momentum transfers during the decays into account, the prediction for an upper limit of the neutrino flux associated with GRBs follows the gamma ray flux scaled down by a factor of about 1/16 [HK10].

Another contribution comes from the GZK-cutoff in the cosmic ray spectrum above a primary energy of $E_{\mathrm{GZK}} = 50$ EeV (see Sec. 2.1.1). A proton interacts with a photon from the CMB and generates a charged pion via the Δ^+ resonance as in Eq. (2.2). The pion decays and produces neutrinos. Since hints of the GZK-cutoff have already been observed as a suppression of the cosmic ray flux by the Auger and HiRes experiments [Pie10, Sok10], the GZK-cutoff is assumed to generate a guaranteed neutrino flux at very high energies.

Whether the pions are produced in proton-proton or proton-photon interactions depends on the source. They are, however, generated in all processes (2.6) - (2.13). Charged pions are produced in equal amounts and only they contribute to the neutrino production.[5] It follows form the decays (2.14) and (2.15) that one electron neutrino, two muon neutrinos and no tau neutrino is produced. Therefore, the flavor ratio at the source is:

$$\nu_e : \nu_\mu : \nu_\tau = 1 : 2 : 0. \tag{2.17}$$

This statement is, in general, equally true for anti-neutrinos. There are, however, cases where the ratio between the neutrino and anti-neutrino of a certain flavor is not equal to one. For example, the beam dump could be radiation dominated such that the proton-photon interactions dominate and the neutron interaction length is large enough to neglect neutron-photon interactions. Then only (2.10) and (2.11) contribute and the production of π^- is suppressed. Consequently, the generation of anti-electron neutrinos from the subsequent muon decay (2.15) would be suppressed for this source [HMWY10].

---

[4] Due to helicity-suppression the decay of a charged pion into a muon is favored with a branching ratio of over 99% compared to the decay into the much lighter electron [Par08].

[5] The neutral pion decays purely electromagnetically $\pi^0 \rightarrow \gamma + \gamma$ with a branching ratio of over 99% [Par08].

Another aspect is that the flavor ratio is not necessarily $\nu_e : \nu_\mu : \nu_\tau = 1 : 2 : 0$ for all sources. For example, if the muon from the pion decay interacts in the source it loses a non-negligible amount of energy. Consequently, the neutrino energy spectrum would be different and the flavor ratio would change to $\nu_e : \nu_\mu : \nu_\tau = 0 : 1 : 0$, since one could only observe the muon neutrino from the pion decay but none from the low-energetic and thus invisible muon decay. However, this distinction is irrelevant for two reasons. Firstly, for a diffuse flux analysis the sum of all contributions causes this effect to be negligible [Pan11]. Secondly, the flavor ratio is altered anyway due to neutrino oscillations over cosmic distances (see Sec. 2.2.3).

2.2.2 Atmospheric Neutrino Flux

The sources and production mechanisms of neutrinos produced in the atmosphere are much better known than for astrophysical neutrinos. Cosmic rays hit the atmosphere and create particle showers containing charged mesons which then decay, among other particle, into neutrinos. Again, the proton-nucleon interactions produce predominantly charged pions which then decay into muons and muon neutrinos as depicted in (2.14). Since the atmosphere is very dense compared to most cosmic sources, the generated pions will interact and lose energy before they decay. This steepens the incoming cosmic ray spectrum from $E^{-2.7}$ to about $E^{-3.7}$ for the generated neutrino spectrum as stated in Eq. (2.5). Also, at high energies the Lorentz boost of the muons is large enough that they reach sea level and penetrate the Earth before decaying. Consequently, there is a flux suppression of electron neutrinos at high energies. These are then predominantly produced in the decay of the long-lived state of the neutral kaon:[6]

$$\mathrm{K}_\mathrm{L}^0 \;\rightarrow\; \pi^\pm \;+\; \mathrm{e}^\mp \;+\; \overset{(-)}{\nu}_\mathrm{e}. \tag{2.18}$$

Another feature in the atmospheric neutrino flux arises at energies above the threshold for the production of charmed mesons such as the D and the $\mathrm{D_s}$. Due to their large mass and available phase space for decay, they are very short-lived. The charmed mesons decay immediately (the lifetime is of the order of 10^{-12} s [Par08]) without interacting in the atmosphere. Consequently, they preserve the parental cosmic ray energy spectrum for the generated neutrinos of $E^{-2.8}$. Because of the immediate decay, this is called the atmospheric prompt neutrino flux. Typical decays including neutrinos in the final state are:[7]

$$\mathrm{D}^\pm \;\rightarrow\; \mathrm{e}^\pm \;+\; \overset{(-)}{\nu}_\mathrm{e} \;+\; \mathrm{X} \qquad \text{and} \qquad \mathrm{D}_\mathrm{s}^\pm \;\rightarrow\; \tau^\pm \;+\; \overset{(-)}{\nu}_\tau. \tag{2.19}$$

Tau neutrinos are only created in these charmed meson decays [PR99]. This is the reason why there are no tau neutrinos in the atmospheric flux at low energies.

Fig. 2.4 summarizes the measurement results from Frejus, AMANDA and IceCube as well as the model predictions for the conventional and the prompt fluxes. The measured muon neutrino flux follows the expectation from the model for conventional neutrinos. It is expected that the harder prompt neutrino flux can only be observed at higher energies but has yet to be observed. This region also marks the discovery range for astrophysical neutrinos crossing the atmospheric spectrum, i.e. the atmospheric neutrino flux falls below the expected flux of astrophysical neutrinos with an E^{-2} spectrum (see Sec. 2.2.1). The atmospheric electron neutrino flux at energies above 10 GeV is not measured well yet, which furthermore stresses the strong motivation for the study presented in this thesis.

---

[6] The short-lived state of the kaon does not produce electrons in the immediate decay. It commonly decays via $\mathrm{K_S^0} \rightarrow \pi^+ + \pi^-$ or $\mathrm{K_S^0} \rightarrow \pi^0 + \pi^0$, which would then give another contribution to the conventional atmospheric neutrino flux by the decay of the charged pions [Par08].

[7] The decay of the charged D is given as an inclusive decay where X stands for a variety of particles of different numbers and types. The given branching ratios are approximately 16% and 6%, respectively [Par08].

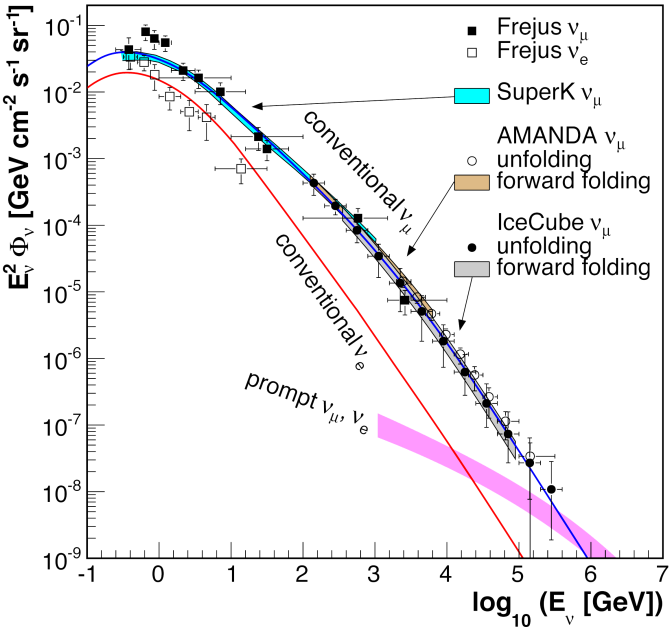

Figure 2.4: The atmospheric neutrino flux: The muon neutrino flux was measured by Frejus, AMANDA and IceCube while electron neutrinos above 10 GeV still need to be measured (Ref. [Wos11]).

2.2.3 Neutrino Oscillations and Flavor Ratios

The IceCube neutrino observatory has different sensitivities for different neutrino flavors. Hence, it is useful to know the expected flavor ratio at the detector. In Sec. 2.2.1 It has already been stated that the flavor ratio at the source generated by the decay of the charged pions is:

$$\nu_e : \nu_\mu : \nu_\tau = 1 : 2 : 0 \qquad \text{(source)} \tag{2.20}$$

Experiments like SNO [SNO01], Super Kamiokande [Sup98] and KamLAND [Kam08] observed solar, atmospheric and reactor neutrinos, respectively, oscillating from one flavor into another. Consequently, neutrino oscillations are well established and cause the given flavor ratio of astrophysical neutrinos to change over cosmic distances on their way to the Earth.

The theoretical assumption is that the neutrino flavor eigenstates $|\nu_\alpha\rangle$ with the flavor $\alpha = e, \mu, \tau$ are superpositions of the three mass eigenstates $|\nu_i\rangle$ with $i = 1, 2, 3$:[8]

$$|\nu_\alpha\rangle = \sum_{i=1}^{3} U_{\alpha i}^{*} \, |\nu_i\rangle \,, \tag{2.21}$$

where $U_{\alpha i}$ denotes the element of the leptonic mixing or the Pontecorvo-Maki-Nakagawa-Sakata (PMNS) matrix [Pon57, Pon68, MNS62]. It can be approximated as [Bec08]:[9]

$$\begin{pmatrix} U_{e1} & U_{e2} & U_{e3} \\ U_{\mu 1} & U_{\mu 2} & U_{\mu 3} \\ U_{\tau 1} & U_{\tau 2} & U_{\tau 3} \end{pmatrix} = \begin{pmatrix} \frac{\sqrt{3}}{2} & \frac{1}{2} & 0 \\ -\frac{1}{2\sqrt{2}} & \frac{\sqrt{3}}{2\sqrt{2}} & \frac{1}{\sqrt{2}} \\ \frac{1}{2\sqrt{2}} & -\frac{\sqrt{3}}{2\sqrt{2}} & \frac{1}{\sqrt{2}} \end{pmatrix} . \tag{2.22}$$

---

[8] For this calculation the normal mass hierarchy is assumed. The phase commonly introduced to describe leptonic CP-violation is neglected and thus the oscillation of neutrinos and anti-neutrinos are equivalent.

[9] It should be stressed that particularly the recent measurement results of $\sin^2 2\theta_{13} = 0.092 \pm 0.017$ at Daya Bay clearly show that $U_{e3} \neq 0$ [Day12].

It can be shown that the oscillation probability of a neutrino with energy E and flavor α into another flavor β over the distance l is given by [Kay81]:

$$P_{\alpha\to\beta}(E,l) = \sum_{i=1}^{3} U_{\beta i}^2 U_{\alpha i}^2 + \sum_{j\neq i}^{3} U_{\beta i} U_{\alpha i} U_{\beta j} U_{\alpha j} \cos\left(\frac{l}{l_{ij}}\right), \tag{2.23}$$

with the oscillation length $l_{ij} = 2E/\Delta m_{ij}^2$. The parameter Δm_{ij} is the squared mass difference between two neutrino mass eigenstates which needs to be determined experimentally. Taking $\Delta m_{12} \simeq 8\cdot 10^{-5}\ \mathrm{eV}^2$ and $\Delta m_{32} \simeq \Delta m_{13} \simeq 2\cdot 10^{-3}\ \mathrm{eV}^2$ [Par06] and assuming a maximum energy of $E \simeq 100$ EeV for astrophysical neutrinos one obtains for the oscillation lengths $l_{12} \simeq 16$ pc and $l_{32} \simeq l_{13} \simeq 1$ pc, respectively.[10] These are in the order of 1 pc and thus much shorter than cosmic distances of the order of 1 Gpc. Consequently, over cosmic distances the oscillating term in Eq. (2.23) averages to zero and only the first constant part remains.

Using the mixing matrix from Eq. (2.22) one can calculate the probability matrix:

$$\begin{pmatrix} P_{\mathrm{e}1} & P_{\mathrm{e}2} & P_{\mathrm{e}3} \\ P_{\mu 1} & P_{\mu 2} & P_{\mu 3} \\ P_{\tau 1} & P_{\tau 2} & P_{\tau 3} \end{pmatrix} = \frac{1}{32} \begin{pmatrix} 20 & 6 & 6 \\ 6 & 13 & 13 \\ 6 & 13 & 13 \end{pmatrix}. \tag{2.24}$$

Using Eq. (2.20) and (2.24) one obtains the altered flavor ratio at the detector:

$$\nu_{\mathrm{e}} : \nu_{\mu} : \nu_{\tau} = 1:1:1 \qquad \text{(observer)}. \tag{2.25}$$

So, due to neutrino oscillations over cosmic distances the astrophysical neutrino flux is equally shared between all flavors and without distinction between neutrinos and antineutrinos.

2.3 Neutrino Detection

The sources and production mechanisms of astrophysical and atmospheric neutrinos have been discussed so far. Another important part of high-energy neutrino astronomy is the detection of these neutrinos along with the measurement of their flavor and energy. The neutrino detection rate in a certain detector material is calculated as

$$R = \int \mathrm{d}\Omega \int_{E^{\mathrm{thr}}} \mathrm{d}E\, A(E,\Omega)\, P(E)\, \frac{\mathrm{d}N}{\mathrm{d}E}, \tag{2.26}$$

with the neutrino energy E and flux $\mathrm{d}N/\mathrm{d}E$, the energy threshold E_{thr} and the solid angle Ω of the detector as well as the effective area A and the interaction probability P of the individual process. The interaction probability can be approximated as

$$P(E) = 1 - \mathrm{e}^{-\frac{l}{l_{\mathrm{int}}(E)}} \simeq \frac{l}{l_{\mathrm{int}}(E)}, \tag{2.27}$$

if the interaction length l_{int} is much longer than the length l that the neutrino travels through the detector. For neutrinos this condition is fulfilled due to the small cross sections. The interaction length is given by

$$l_{\mathrm{int}}(E) = \left[\frac{\rho N_{\mathrm{A}}}{m_{\mathrm{mol}}} \sigma_{\nu\mathrm{X}}(E)\right]^{-1}, \tag{2.28}$$

where N_{A} is the Avogadro constant, ρ is the density and m_{mol} the molar mass of the detector material. The cross section $\sigma_{\nu\mathrm{X}}$ depends on the neutrino energy E and the scattering process, e.g. elastic scattering with an electron or deep-inelastic scattering with a nucleus of the target. These processes will be discussed in more detail in the following section.

---

[10] For this calculation one needs to multiply the given oscillation length l_{ij} by a factor $\hbar c \simeq 197$ MeV fm to convert the number from natural to SI units.

2.3.1 Neutrino Interactions

In the standard model neutrinos only interact via the weak force. The weak force is mediated by the charged W bosons and the neutral Z boson. The corresponding processes are called *charged current* (CC) and *neutral current* (NC) interactions, respectively (see e.g. Ref. [HM84]). At high energies deep-inelastic neutrino-nucleon scattering becomes dominant.[11] The interaction processes for high-energy neutrinos in water or ice Cherenkov detectors are

$$\overset{(-)}{\nu}_l + N \rightarrow l^\pm + X \quad \text{(CC)} \tag{2.29}$$

$$\text{and} \quad \overset{(-)}{\nu}_l + N \rightarrow \overset{(-)}{\nu}_l + X \quad \text{(NC)}. \tag{2.30}$$

The corresponding Feynman graphs are depicted in Fig. 2.5. In the CC interaction a neutrino ν_l creates the corresponding lepton $l = e, \mu, \tau$ by emitting a W boson. The exchange particle breaks up the nucleus N and creates a particle shower X. The NC interaction is similar except that there is no charged lepton. Instead the incoming neutrino ν_l of arbitrary flavor l survives and emits a Z boson, which also breaks up the nucleus. The processes of the NC interactions look the same and the cross sections are equal for all flavors [GQRS98].

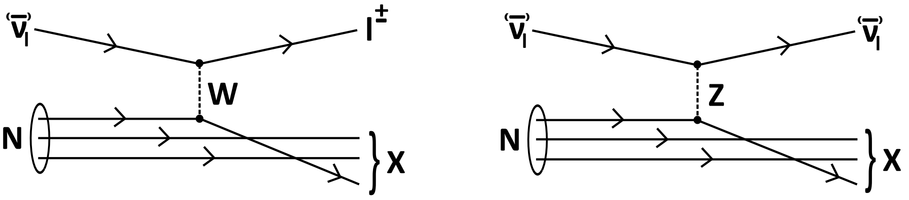

Figure 2.5: Feynman graphs of the deep-inelastic CC (left) and NC (right) neutrino interactions.

In general, the neutrino-nucleon cross section can be calculated using the Feynman rules emerging from quantum field theory (QFT). It is approximately given by [GQRS98]:

$$\sigma_{CC/NC} = \frac{2G_F^2}{\pi} m_N E_\nu \left(\frac{m_{W/Z}^2}{Q^2 + m_{W/Z}^2} \right)^2 , \tag{2.31}$$

where G_F is the Fermi constant, $m_{W/Z}$ are the masses of the W and Z bosons, respectively, and Q^2 is the invariant momentum transfer. This is only a simplified picture, since for a correct treatment one has to take into account the quark and anti-quark parton density functions, both being dependent on the momentum transfer.

Although never measured directly, the neutrino-nucleon cross section could be calculated up to energies of 50 TeV from measurements at HERA [Ren06]. However, particularly for higher energies they can only be extrapolated but not measured anymore, since the necessary energies are far beyond anything accessible in modern collider experiments. At these energies the cross section in Eq. (2.31) becomes incorrect due to various effects. Only in regions where the momentum transfer is small compared to the boson mass, the cross section scales linearly with the neutrino energy. At higher energies the momentum transfer dampens the cross section which decreases the energy scaling to approximately $E^{0.4}$ [GQRS98]. At ultra-high energies the cross section has further corrections arising from perturbative quantum chromodynamics (QCD), where the heavy quarks need to be included in the quark sea.

---

[11] Deep-inelastic scattering becomes dominant at neutrino energies above the typical binding energy per nucleon of approximately 10 MeV. Below this energy threshold, neutrino detection processes include the elastic electron scattering $\bar{\nu}_e + e^- \rightarrow \bar{\nu}_e + e^-$ and the inverse β-decay $\bar{\nu}_e + p \rightarrow n + e^+$ [Sup98].

The correct parametrization of the neutrino-nucleon cross section for CC and NC interactions and for neutrinos and anti-neutrinos in dependence of the energy is depicted in Fig. 2.6. At low energies the cross sections for anti-neutrinos are, in general, smaller since the contribution from sea quark scattering is negligible. Only at higher energies they become approximately equal for both neutrinos and anti-neutrinos, since then the contribution from the valence quark scattering is negligible. Furthermore, the CC and NC cross sections have the same shape and only differ by a constant factor. In this region the neutrino-nucleon cross sections can be parametrized for energies $E_\nu = 10^6 \ldots 10^{12}$ GeV as follows [GQRS98]:[12]

$$\sigma_{\mathrm{CC}}^{\nu\mathrm{N}} = 5.53 \cdot 10^{-36}\,\mathrm{cm}^2 \left(\frac{E_\nu}{\mathrm{GeV}}\right)^{0.363} \tag{2.32}$$

$$\text{and} \quad \sigma_{\mathrm{NC}}^{\nu\mathrm{N}} = 2.31 \cdot 10^{-36}\,\mathrm{cm}^2 \left(\frac{E_\nu}{\mathrm{GeV}}\right)^{0.363} . \tag{2.33}$$

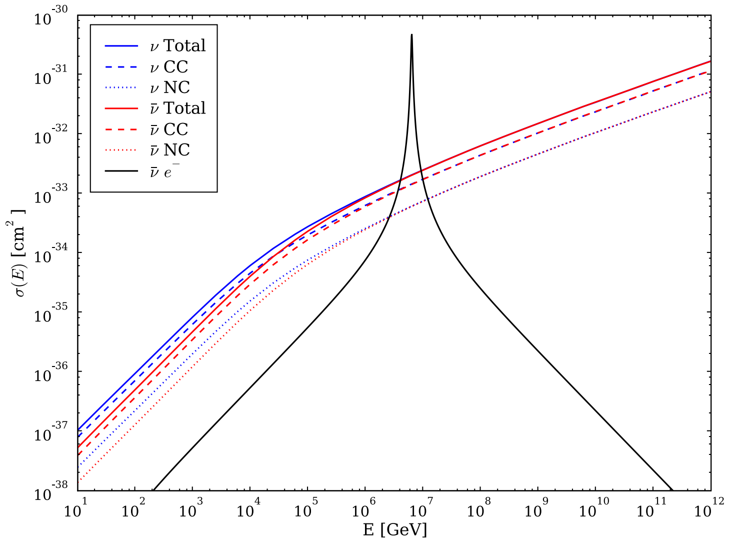

Figure 2.6: The neutrino-nucleon cross sections: They are depicted for a neutrino energy range of 10 GeV to 100 EeV. The total cross section for neutrinos and anti-neutrinos is approximately equal for energies above 10^6 GeV where the CC and NC contributions are parameterized via Eq. (2.32) and (2.33), respectively. The *Glashow resonance*, where a real W boson is produced in resonance from the inelastic $\bar{\nu}_e\, e^-$ scattering, is expected at an energy of approximately 6 PeV (Ref. [Voi08]).

2.3.2 Energy Losses and Particle Showers

In the previous section it became clear that a CC neutrino interaction creates a charged lepton and a particle shower and the NC neutrino interaction only creates a particle shower. The charged leptons (electrons, muons and taus) predominantly interact via the electromagnetic force while propagating through matter. The particle shower is a cascade of charged and neutral particles of all sorts, which interact via different forces. In the first part of this section the propagation of charged particles in matter and the corresponding energy losses are discussed. The second part is about the development of electromagnetic and hadronic cascades.

---

[12] The anti-neutrino-nucleon cross sections for the CC and NC interactions are approximately equal [GQRS98].

Propagation of Charged Particles in Matter

There are many different interaction processes of charged particles with matter. Most of them cause the particle to lose some of its energy and others cause a change of direction. Mostly, these interactions are mediated by the electromagnetic force. There is, however, an important distinction between the types of energy losses. Ionization of target atoms causes a continuous energy loss of the propagating particle. Other processes like bremsstrahlung, pair production and photo-nuclear interactions are of stochastic nature, i.e. these energy losses are randomly distributed along the path of the particle. The probability of these stochastic energy losses scales linearly with the particle energy.

Ionization is caused by the collision of the traversing particle with atomic electrons of the target. This causes an ionization of the atoms. The energy loss $\mathrm{d}E$ of the particle along the path length $\mathrm{d}X$ in matter is given by the Bethe-Bloch formula [Per09]:

$$\left\langle \frac{\mathrm{d}E}{\mathrm{d}X} \right\rangle_{\mathrm{ion}} = -\frac{4\pi N_{\mathrm{A}} z^2 e^4}{m_{\mathrm{e}}\beta^2}\frac{Z}{A}\left[\ln\left(\frac{2m_{\mathrm{e}}\beta^2\gamma^2}{I}\right) - \beta^2\right], \tag{2.34}$$

where N_{A} is the Avogadro constant, e the elementary charge and m_{e} the electron mass. The target medium is characterized by the atomic number Z and the mass number A of the nucleus and by the ionization potential $I \simeq 10\,\mathrm{eV}\cdot Z$, averaged over all electrons in the atom. The traversing particle is given by its charge number z, velocity $\beta = v/c$ and Lorentz boost $\gamma = 1/\sqrt{1-\beta^2}$. The path length X is usually measured in $\mathrm{g\,cm^{-2}}$ to account for the length and the target density. The ionization loss does not depend much on the material, since $Z/A \simeq 1/2$ except for hydrogen and the very heavy elements. Furthermore, it is only dependent on the velocity and charge of the traversing particle and not on its mass. Consequently, the ionization losses are equal for electrons, muons and taus. Also, since the velocity is limited to $\beta \simeq 1$, the ionization energy loss reaches a constant value for high energies of about 2 $\mathrm{MeV\,g^{-1}\,cm^2}$. Therefore, high-energy particles continuously lose a constant energy of approximately 0.2 $\mathrm{GeV\,m^{-1}}$ due to the ionization in ice.[13]

Coulomb scattering is caused by the electromagnetic interaction between a charged particle and the target atom. The single scattering process is described by the Rutherford formula. Multiple scatterings cause a Gaussian distribution of the deflection from the incident direction of the particle. The radiation length is defined as the average length until a charged particle scatters. In general, it is dependent on the target material as well as on the traversing particle and can be parameterized by [Per09]:

$$\frac{1}{X_0} = \frac{4\alpha^3 N_{\mathrm{A}}}{m^2}\frac{Z(Z+1)}{A}\ln\left(\frac{183}{Z^{1/3}}\right), \tag{2.35}$$

which is valid for a particle with mass m and charge e traversing a target with atomic number Z and mass number A. As before, N_{A} is the Avogadro constant and α the electromagnetic fine structure constant. The deflection is dependent on the energy of the particle. More important, however, is the associated energy loss due to bremsstrahlung.

Bremsstrahlung is emitted when a charged particle is deflected by either the nucleus or an electron of the target atom (Coulomb scattering). It loses energy according to [Per09]:

$$\left\langle \frac{\mathrm{d}E}{\mathrm{d}X} \right\rangle_{\mathrm{brems}} \simeq -\frac{E}{X_0}, \tag{2.36}$$

---

[13] In this case the density of ice is approximated as $\rho \simeq 1\,\mathrm{g\,cm^{-3}}$.

which is transferred to the emitted photons. The radiation length X_0 is given in Eq. (2.35) and can, in this case, be interpreted as the distance where the energy loss has decreased to $1/e$ of its original value. Converting to SI-units and using the electron mass one obtains a radiation length of $X_0 \simeq 36.08\,\mathrm{g\,cm^{-2}}$ in ice [Voi08]. This corresponds to an interaction length of approximately 36 cm. In most cases the energy losses of heavier particles can be neglected, since the electron is the lightest charged particle and $X_0 \sim m^2$. The radiation length for a muon as the next heavier particle is a factor $(m_\mu/m_e)^2$ larger than for an electron. With $m_\mu \simeq 106$ MeV and $m_e \simeq 0.511$ MeV [Par08] this gives an interaction length of approximately 15 km for muons in ice. However, it can also be seen from Eq. (2.36) that the bremsstrahlung energy losses scale linearly with the particle energy. Consequently, at very high energies the bremsstrahlung losses are not negligible for muons and, in fact, become the main source for Cherenkov light detected in IceCube (see Sec. 2.3.3).

Pair production refers to the process where a high-energy photon creates an electron positron pair. This only happens in the vicinity of the Coulomb field of a nucleus due to momentum conservation and if the photon energy is above the production threshold of $E_\gamma > 2m_e$. Similar to the radiation length there is a conversion length which describes the mean free path before a photon converts into an electron positron pair. At high energies above a few GeV it has a constant value of $(9/7)\,X_0$ [Per09]. The energy loss due to pair production also scales linearly with the particle energy and is thus given by:

$$\left\langle \frac{\mathrm{d}E}{\mathrm{d}X} \right\rangle_{\mathrm{pair}} \simeq -\frac{7}{9}\frac{E}{X_0}, \tag{2.37}$$

Other processes that cause a particle to lose energy include *Cherenkov radiation*, *photo-nuclear interactions*, the *(inverse) Compton scattering* and the *decay* of particles. If certain conditions are fulfilled, a charged particle can lose energy by emitting Cherenkov radiation. This is a very important effect for detecting particles in IceCube and will be discussed in more detail in Sec. 2.3.3. Photo-nuclear interactions do not contribute to the total energy loss of a particle as much as bremsstrahlung and pair production. The (inverse) Compton scattering is only relevant when the charged particle interacts with a present photon or vice versa. The decay of a particle is the extreme situation where it loses all its energy and thus ceases to exit. In the IceCube detector a muon will most likely decay after having lost most of its energy. Consequently, the electron or positron produced in the decay will be of low energy and thus invisible for the detector. The decay of particles, therefore, does not contribute significantly to the total energy deposition in the detector.

Development of Electromagnetic and Hadronic Cascades

In the previous section the different processes which cause a charged particle to lose energy while propagating through matter have been discussed. For each of these processes there are specific energy thresholds. For pair production the photon must have an energy $E_\gamma > 2m_e$. For the bremsstrahlung (as the most dominant process) this energy threshold is given by the critical energy E_c where its energy loss is equal to the ionization energy loss [Per09]:

$$\left\langle \frac{\mathrm{d}E}{\mathrm{d}X} \right\rangle_{\mathrm{brems}} = \left\langle \frac{\mathrm{d}E}{\mathrm{d}X} \right\rangle_{\mathrm{ion}} . \tag{2.38}$$

Consequently, at energies above this threshold the particle suffers energy losses due to mentioned interactions. It is $E_c = 78.99$ MeV for ice [Voi08].

For example, a highly energetic electron produced in the CC neutrino interaction undergoes stochastic energy losses many times and creates many secondary particles like photons, electrons and positrons. Depending on the transferred energy, these secondaries can also be highly energetic so that they undergo energy losses as well until their energy drops below E_c. This so-called *particle shower* or *cascade* creates lots of particles in exponentially increasing numbers with decreasing energies. Depending on the processes involved one separates an electromagnetic from a hadronic cascade.

Electromagnetic cascades are particle showers where the secondary particles only interact via the electromagnetic force. The principle is depicted in Fig. 2.7. An incident electron of energy E_0 radiates off a bremsstrahlung photon, which then converts into an electron positron pair and so on. This process can be described in a simple way by the Heitler model [Per09]. In this model one assumes that each particle interacts after propagating one radiation length. After each interaction the number of secondary particles increases by a factor of 2 and the energy per particle is reduced by a factor of 1/2.

The shower depth t, defined as the longitudinal shower length in units of the radiation length, describes the number of particles and the energy per particle after each interaction:

$$N(t) = \frac{E_0}{E(t)}, \tag{2.39}$$

$$E(t) = \frac{E_0}{2^t}. \tag{2.40}$$

The maximum number of particles is simply given by $N_{\max} = E_0/E_c$ and the maximum shower depth $t_{\max} = \ln(E_0/E_c)/\ln 2$, i.e. both are limited by the critical energy where ionization losses become dominating.

There are two important conclusions from Eq. (2.39) and (2.40). First, the number of shower particles increases linearly with the primary energy $N_{\max} \sim E_0$. This is important for the IceCube detector, since it measures Cherenkov light produced by all charged particles of the cascade (see Sec. 2.3.3). Second, the maximum shower depth increases logarithmically with the primary energy $t_{\max} \sim \ln E_0$. This is important for the upper energy threshold of a detector. Only a fully contained cascade allows an energy measurement with a good resolution.

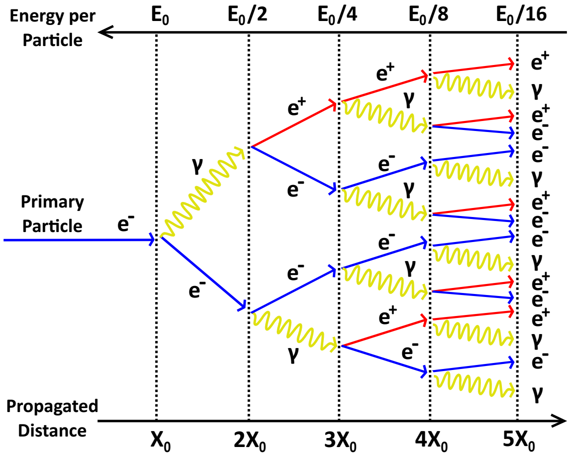

Figure 2.7: The principle of an electromagnetic shower: An incoming electron of energy E_0 interacts with the target atom via bremsstrahlung after one radiation length X_0. After each propagated distance of one radiation length the number of particles is increased by a factor of 2 and the energy per particle is reduced by a factor of 1/2.

The dimension of the cascades typically measured in IceCube are of the order of a few meters (see Sec. 4.1). Since IceCube has a volume of about 1 km^3, neutrino-induced cascades which have their interaction vertex inside the detector are de facto fully contained. The very high energetic cascades can, however, produce so much Cherenkov light that it illuminates the complete detector and escapes partly.

Hadronic cascades are much more complicated to describe than electromagnetic cascades, since there is a variety of generated particles and interaction channels. The principle of shower development is the same as for electromagnetic cascades, however, a mixture of leptons, baryons and mesons are produced. In the shower mostly pions are produced which either interact again via the strong interaction producing all kinds of hadrons or, more likely, they decay.

A neutral pion immediately decays into two high-energy photons and the charged pion decays into muons and electrons. These secondary particle then cause an electromagnetic cascade within the surrounding hadronic cascade. The electromagnetic and the hadronic particle showers cannot be separated from each other. However, the higher the energy the more pions are produced. Therefore, the contribution of the electromagnetic cascade within the hadronic cascade increases with the primary energy [Pan11]. If a charged pion decays it creates neutrinos which most likely escape the detector without interacting. If a neutron is produced it will either interact or decay. In any case it produces further secondary particles which can be detected. The total amount of neutral particles which are not detected is, hence, relatively small.

There are, however, some problems with hadronic cascades. The binding energy needed to break up hadrons reduces the kinetic energy of the secondary particles, i.e. there is less energy available for secondary particle generation to be detected. In the energy measurement this is accounted for using a form factor. Also, the heavier hadrons are slow compared to electrons and muons and thus might not fulfill the condition to emit Cherenkov radiation (see Sec. 2.3.3). Consequently, these particles cannot be measured with the IceCube detector.

In conclusion, the energy resolution for hadronic cascades is worse than for electromagnetic cascades, since there are different contributions which are not detectable and the overall transference into detectable secondary particles is reduced. It has already been stated a couple of times throughout the chapter that secondary particles which are produced in electromagnetic and hadronic cascades can be detected via their Cherenkov radiation. Since this is the detection technique used in IceCube, it will be discussed in more detail in the next section.

2.3.3 Cherenkov Photons

Cherenkov radiation is produced when charged particles traverse a dielectric medium faster than the phase velocity of light in this medium. The charged particle couples to the molecular dipoles via the electromagnetic force while passing through the medium. The atoms of the medium are excited and return into their ground state by emitting light.

This light is emitted isotropically and interferes destructively with the emission from neighboring atoms. Only if the particle traverses the medium faster than the phase velocity of light in the medium, the light is emitted coherently in a shock front similar to a sonic boom. It interferes constructively and produces a light cone. This cone has an opening angle given by

$$\cos\theta_{\text{Ch}} = \frac{1}{n\beta}. \tag{2.41}$$

This can be seen from the simple trigonometric relation depicted in Fig. 2.8. Both the opening angle of the cone and the wavelength of the light depend on the refractive index $n = c/v_{\text{phase}}$ of the material. It can be concluded that Cherenkov radiation is only emitted if $n\beta > 1$.

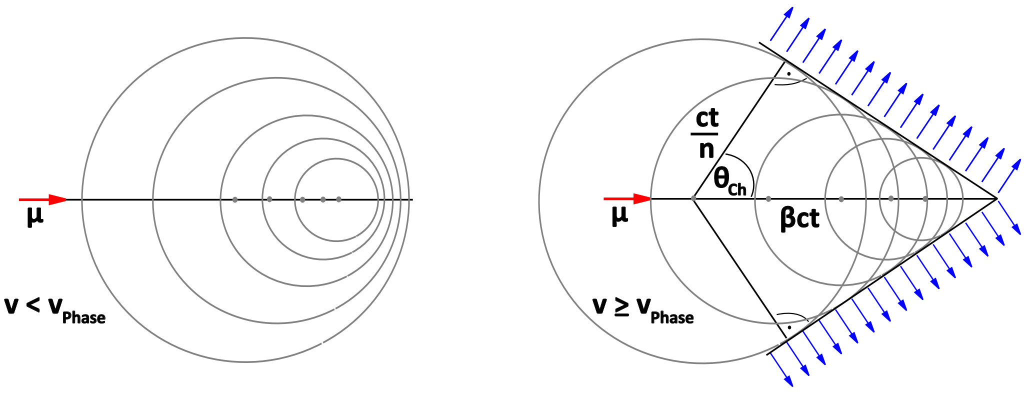

Figure 2.8: The Cherenkov effect: A muon traverses a dielectric medium with refractive index n at a speed $v = \beta c$. The circles represent wave fronts of equal phase. The phase velocity of the light is reduced by $1/n$ compared to the speed of light in vacuum. If the velocity is less than the phase velocity, the light emission is isotropic and interferes destructively (left). If it is greater the light emission builds a wave front which interferes constructively (right).

The refractive index for ice, which is the dielectric medium in the IceCube detector, is $n_{\mathrm{ice}} = 1.33$ [Voi08]. Consequently, the threshold velocity for charged particles to create Cherenkov radiation in ice is $\beta_{\mathrm{Ch}} \simeq 0.75$, corresponding to threshold energies of 0.26 MeV and 54 MeV for electrons and muons, respectively. These are far below the detection threshold of IceCube. All high-energy particles basically have a velocity of approximately $\beta \simeq 1$ and thus the opening angle of the Cherenkov cone is $\theta_{\mathrm{Ch}} \simeq 41°$ in ice. The wavelength of the emitted Cherenkov spectrum peaks in the waveband between ultraviolet and blue light.

The number of Cherenkov photons that a single-charged particle emits along a distance $\mathrm{d}x$ within a waveband $\mathrm{d}\lambda$ is given by the Frank-Tamm formula [Jac75]:

$$\frac{\mathrm{d}^2 N}{\mathrm{d}x\mathrm{d}\lambda} = \frac{2\pi\alpha}{\lambda^2}\left(1 - \frac{1}{\beta^2 n^2}\right). \tag{2.42}$$

For ice this gives approximately 300 photons/cm in a waveband of $\lambda = 300 \ldots 600$ nm [Pan11].

In conclusion, high-energy neutrinos interact with nuclei in the detector material and create cascades of charged particles. These secondary particles mainly lose energy via bremsstrahlung, pair production and photo-nuclear interactions. They also emit Cherenkov photons while propagating through the ice. The task of the detector is to measure these photons and to deduce the energy and direction of the cascades and, thereby, of the incident neutrino.

However, there are certain obstacles when trying to measure the Cherenkov photons. First, they scatter at dust particles in the ice and they can be absorbed. This decreases the number of photons arriving at the detector and it deteriorates the directional information. The ice has to be modeled and the propagation of the Cherenkov photons needs to be simulated to understand the detector response precisely. Second, the actual detection strongly depends on the quantum efficiency and the noise of the detection devices. The IceCube detector and its properties will be discussed in more detail in the following chapter.

3. The IceCube Detector

The era of high-energy neutrino astronomy began with the construction of large neutrino detectors. The need for kilometer-scaled detectors is based on the low flux of high-energy neutrinos. Two important high-energy neutrino telescopes are the ANTARES detector in the Mediterranean Sea and the shut down AMANDA detector at the geographical South Pole in Antarctica [ANT12, AMA12]. Both are Cherenkov detectors and use water or ice as detection medium. Today, IceCube with an instrumented volume of about 1 km^3 is the biggest neutrino detector in the world. Its development and construction was supported by the technical knowledge and experience acquired particularly with its precursor AMANDA.

In the first section of this chapter the layout of the IceCube detector and its properties are covered. The optical sensors are the main detector component. Their design and the signal digitization are briefly described in the subsequent sections. In the last section the properties of the antarctic ice and corresponding models are discussed.

3.1 Detector Layout

The IceCube neutrino observatory is located at the Amundsen-Scott South Pole station in Antarctica. It employs 1 km^3 of the antarctic ice to form a particle detector. A gigaton of deep and ultra-transparent glacial ice is instrumented with a total of 5160 optical sensors. They detect Cherenkov light emitted by secondary particles which are produced in the interaction of neutrinos with the nuclei in the ice. The sensors are attached to a total of 86 strings which were deployed into the ice by drilling 2.5 km deep holes with hot water. After the insertion of the strings the water froze again and sealed the optical sensors irreversibly. The construction lasted from January 2005 to December 2010. The detector has been taking data in its full capacity ever since [Ice12b].

The basic detector layout is depicted in Fig. 3.1 from the side and in Fig. 3.2 from the top. It consists of three different parts: *IceCube*, *DeepCore* and *IceTop*.

IceCube is the large detector array consisting of 78 strings with 60 optical sensors each. The horizontal distance between two strings is 125 m and the vertical distance between two optical sensors is 17 m [Ice01]. The optical sensors are deployed inside the ice between a depth of 1450 m and 2450 m below the surface. The instrumentation density limits the lower energy threshold to about 200 GeV. Horizontally, the strings are laid out in a hexagonal pattern. The deployment of the strings was stretched over several seasons which resulted in different detector geometries. Depending on the number of deployed strings they are called IC22, IC40, IC59 and IC79 for the years 2007 until 2010 and IC86 since the completion of the detector [Ice12b]. The study that is presented in this thesis is performed with the IC79 dataset from the season 2010/11. This detector geometry lacks the strings 1, 7, 14, 22, 31, 79 and 80 which does not influence the shape of the detector significantly (c.f. Fig. 3.2).

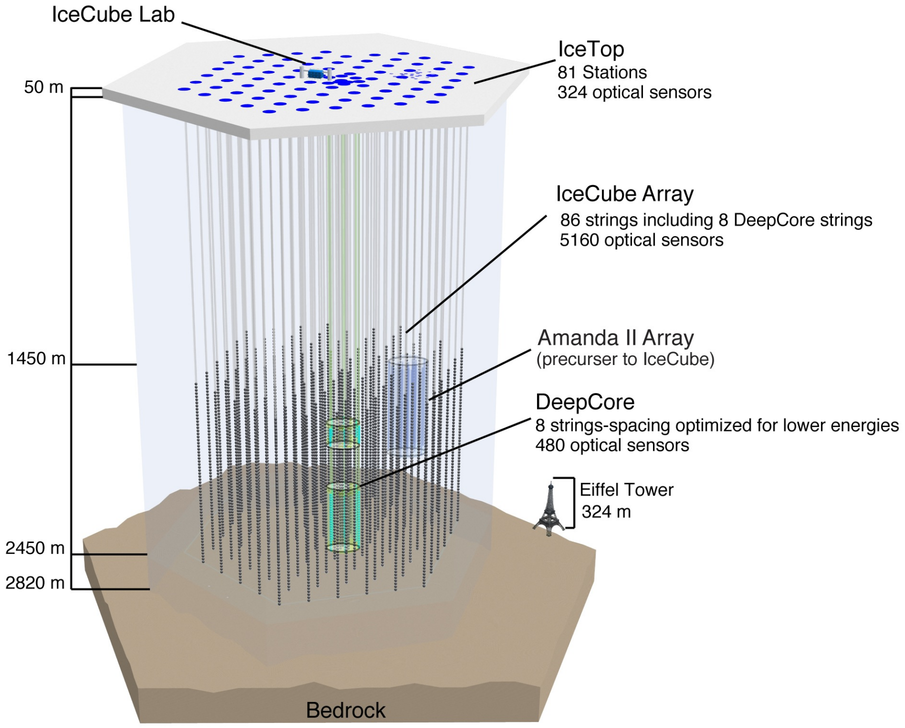

Figure 3.1: The overall layout of the IceCube detector: The IceCube array consists of 86 strings with 60 optical sensors each. The low-energy extension DeepCore comprises 8 of these strings with a denser instrumentation around the center of the detector. The air shower extension IceTop is located at the surface of the ice and consists of 81 stations each containing two ice-filled tanks with two optical sensors. The remainders of the AMANDA II array are sealed inside the IceCube detector (Ref. [Ice12c]).

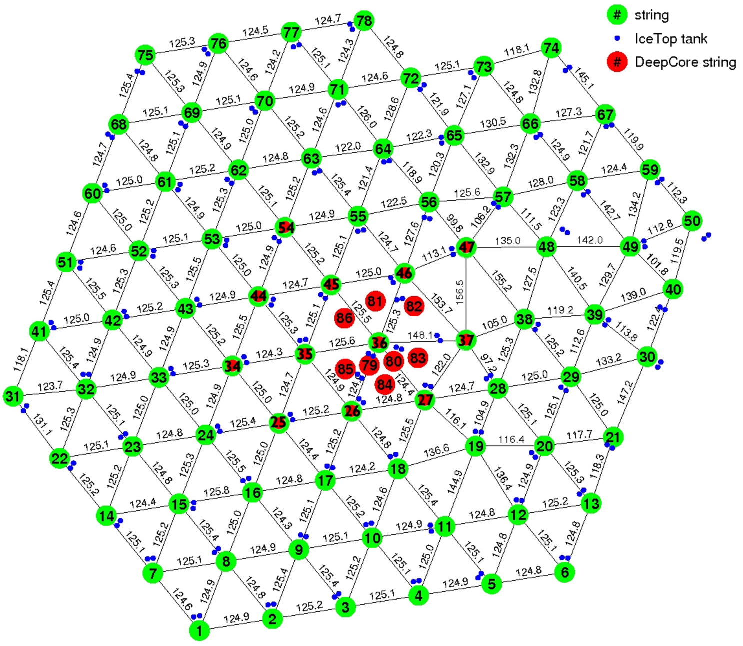

Figure 3.2: The horizontal layout of the IceCube detector: In total 86 strings form a hexagon with 78 strings for IceCube (green) and 8 strings for DeepCore (red) with an average distance between two strings of 125 m and 72 m, respectively (Ref. [Ice12c]).

DeepCore is a low-energy extension of IceCube located at the center of the detector and divided into two parts above and below a dense dust layer. It consists of the remaining 8 strings which are deployed closer together. Each of the center strings has the same length but the instrumented section is shorter and with 60 DOMs per string much denser. The average horizontal distance between two DeepCore strings is 72 m and the vertical distance between two optical sensors is 7 m. The denser instrumentation of the optical sensors in DeepCore and a slightly higher quantum efficiency decrease the energy threshold down to about 10 GeV.

IceTop is an air-shower extension of IceCube located at the surface. It consists of 81 stations each approximately located above one IceCube string. A station consists of two ice-filled tanks with two optical sensors each. In total this sums up to another 324 optical sensors. The goal of IceTop is to detect air showers which allows for a cosmic ray composition study and a veto for muons from air showers entering the detector from above. The IceTop datasets were not available for this study but might be used as an improvement for future studies.

3.1.1 Digital Optical Modules

The optical sensors which detect the Cherenkov light produced by secondary particles are the main component of IceCube. Each sensor is a complete data acquisition system and is, hence, called *digital optical module* (DOM) [Ice01]. The schematic view of a DOM is depicted in Fig. 3.3. It contains a photomultiplier tube (PMT) including a high-voltage source (HV), digitization electronics, control and trigger systems and several light-emitting diodes (LED) for calibration. All parts are contained in a spherical glass pressure vessel. The digitized data from a DOM is readout by the IceCube laboratory at the surface of the ice.

The glass vessel is 1.25 cm thick and has a diameter of 33 cm. It is filled with nitrogen at a pressure of 0.5 atm and consists of borosilicate. It is resistant to the high pressure and thermal stress of the deep antarctic ice. The glass has a low potassium content which reduces the background radioactivity from the ^{40}K β-decay.

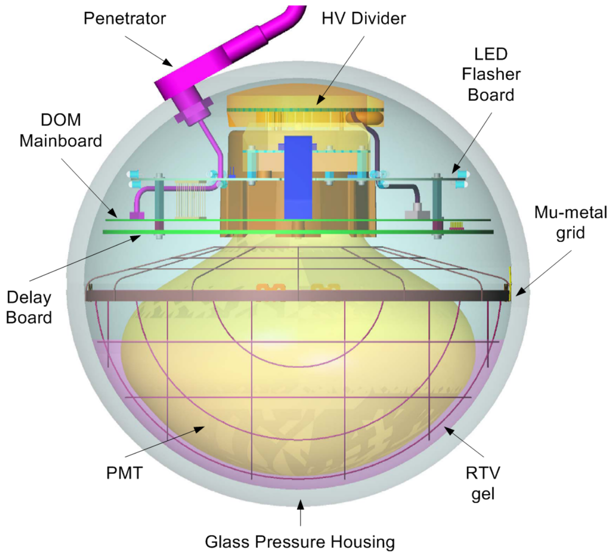

Figure 3.3: Schematic view of a digital optical module (DOM): It contains a photomultiplier tube (PMT) with a high-voltage source (HV), digitization electronics for control and trigger systems and light-emitting diodes (LEDs) for calibration purposes. The mu-metal grid shields the PMT from the Earth's magnetic field and the room temperature vulcanizing gel (RTV) optically couples the PMT to the glass pressure vessel (Ref. [Ice12c]).

For the photon detection a 25 cm diameter R7081-02 photomultiplier tube made by Hamamatsu Photonics is used. It contains 10 dynodes and a 2 kV high voltage source. The PMT has a spectral response from 300 nm to 650 nm, a quantum efficiency of 25% at 390 nm[1] and a transit time spread[2] of 3.2 ns. The dark noise rate is about 400 Hz, mostly caused by the ^{40}K decay in the glass vessel. The PMT is shielded from the Earth's magnetic field by a mu-metal grid and optically coupled to the glass vessel by a room temperature vulcanizing gel (RTV).

Each DOM carries six pairs of 405 nm flasher LEDs which are laid out in a circular pattern to cover different angles. They are used for calibration purposes of the DOMs and to measure the ice properties by the absorption and scattering of the flasher light between two or more neighboring DOMs (c.f. Sec. 3.2).

The readout electronics contain a EPXA4 field-programmable gate array (FPGA) which includes an ARM9-type CPU on its die [Ice09]. The FPGA is configured for calibration, system testing and monitoring, configuration and data transport. It performs the trigger logic, records pulses, compresses data, saves it into the main memory of the DOM and makes it available for the readout by the IceCube laboratory at the surface of the ice.

3.1.2 Signal Digitization and Noise Suppression

In IceCube it is neither possible nor desirable to read out every single DOM continuously. Each string must be able to transmit data from 60 DOMs to the so-called *DOM hub* and the IceCube online data center must be able to manage the data acquisition (DAQ) of 86 DOM hubs. Aside from limited storage capacity at the South Pole, the bandwidth of the strings and the processing power of the data center are strictly limited. Therefore, it is crucial to reduce the noise read out as much as possible by implementing an intelligent trigger logic. The digitizers of the DOM reduce the needed CPU power for the DAQ significantly. An adjacent hit cleaning allows further noise reduction for the analysis.

Digitizer: The signal from the PMT is split into a delay line and a discriminator with a nominal threshold of 0.25 photo electrons (PE). If the discriminator triggers, the delayed signal is sampled by two different digitizers. The first is called *analog transient waveform digitizer* (ATWD) and the second *flash analog-to-digital converter* (fADC).

There are four different ATWD channels. One is used for internal calibration and to measure the LED voltage during flasher measurements. The other three differ by their amplification factors (×0.25, ×2 and ×16) for a maximum dynamic range. Each ATWD has a sampling rate of 300 MHz at a 10 bit resolution. This gives 128 samples each lasting 3.3 ns for a total readout time of 422.4 ns. The whole digitization process of one ATWD may take as long as 30 µs. In order to effectively decrease the DOM's dead time to zero, two ATWDs are operated in parallel. The fADC has a much coarser sampling rate of 40 MHz at a 10 bit resolution. This gives 256 samples each lasting 25 ns for a total readout time of 6.4 µs. It is, therefore, particularly applicable for late PMT pulses in the tail of the waveform after the ATWDs stopped recording. Each digitized waveform is defined by a set of parameters $\{n_i, t_i, \Delta t_i\}$ with n_i being the amplitude in counts, t_i the time and Δt_i the length of each bin $i \in [0, 127]$ for ATWD and $i \in [0, 255]$ for fADC waveforms. If the readout is triggered, these waveforms are sent to the DAQ where they are calibrated, combined and characterized to convert ATWD samples and counts to the measured time and charge, respectively (see Sec. 4.3.1).

---

[1] The PMTs used for DeepCore have a quantum efficiency of 33% at a wavelength of 390 nm.

[2] The transit time spread is the time from the photon absorption at the photocathode to the corresponding pulse at the readout anode of the PMT.

Trigger: Whether a PMT pulse at one DOM should be digitized and whether the complete detector should be read out[3] is determined by several triggers which are implemented in the IceCube laboratory at the surface. The most fundamental trigger condition has already been introduced, i.e. a so-called *DOM launch* occurs if a PMT signal exceeds the discriminator threshold of 0.25 PE. The subsequent trigger comprising several DOMs is called *hard local coincidence* (HLC). It is fulfilled, if there is at least one more launch of the nearest or next-to-nearest neighbor DOMs on the same string within a time window of 1 µs. If the HLC trigger condition is fulfilled all pulses are digitized and save into the flash memory of the DOMs. This reduces the traffic of single DOM launches caused by background radioactivity.

The so-called *simple multiplicity trigger* (SMT8) is the most important global trigger for the study presented in this thesis. It is fulfilled, if eight or more HLC triggers throughout the complete detector occur within a time window of 5 µs. After having been triggered, the readout of the detector is extended by ±10 µs before the first and after the last DOM launch. At the surface all DOM launches in overlapping time windows are combined to form an event. The stream of events is then processed for the waveform calibration and first simple reconstructions (see Sec. 4.3). Afterwards, the data is saved onto tapes which are brought to the North at least once every season by plane. Approximately 70% of all events are sent directly via satellite to the IceCube data center in Madison, Wisconsin.

Another readout concept called *soft local coincidence* (SLC) was developed to gain more information about an event. It means that the PMT waveform is digitized and saved whenever the PMT signal exceeds the threshold. Since there actually is no coincidence with neighboring DOMs at all, the software only emulates the trigger. Only the so-called *charge stamp* is read out to reduce the bandwidth demand. It contains three of the 25 first FADC samples, i.e. the bin with the highest amplitude and its two neighbors. With the SLC readout the rate of DOM launches due to noise is increased. Therefore, a hit cleaning needed to be developed.

Hit cleaning: Noise is created by single hits caused by the background radioactivity of the pressure vessel glass. The easiest way to reduce this noise is given by the HLC trigger, since the probability of two ^{40}K decays in neighboring DOMs within a time window of 1 µs is much smaller than for two in a single DOM. However, this noise rejection technique also removes about 30% of physical hits (Cherenkov photons originating from a low-energy particle) [Sch10].

A new hit cleaning needed to be developed to have a better handle on distinguishing real and noise SLC hits. The method is called *seeded RT-cleaning* and depicted in Fig. 3.4. It consists of two parts. First, a clean set of HLC hits is obtained and compared to the full set of HLC and SLC hits. Similar to the HLC trigger a hit is only kept if there is another hit nearby but instead of demanding the hit to be on the nearest or next-to-nearest neighbor DOM on the same string, one defines a radius R and a time window T in which the hit has to be contained. After applying this so-called *RT-cut* one has achieved a new set of DOM launches which contains the original clean HLC hits extended by the SLC hits that survived this cut. The second step is to use the new set of DOM hits as a seed for another iteration of the RT-cut compared to the full set of DOM launches. This procedure is repeated until there are no further SLC hits left which survive the cut. The result is a cleaned set of HLC and SLC hit.

Compared to a simple RT-cut the seeded RT-cleaning removes outlying hit clusters which are caused by noise and not causally connected with the initial HLC hits. The empirical default settings are $R = 150$ m and $T = 1$ µs. Compared to the average distance of 125 m between two strings, the HLC trigger condition thus effectively has been extended to the coincidence of two neighboring strings.

---

[3] The DAQ does not read out single DOMs or strings, but rather the complete detector.

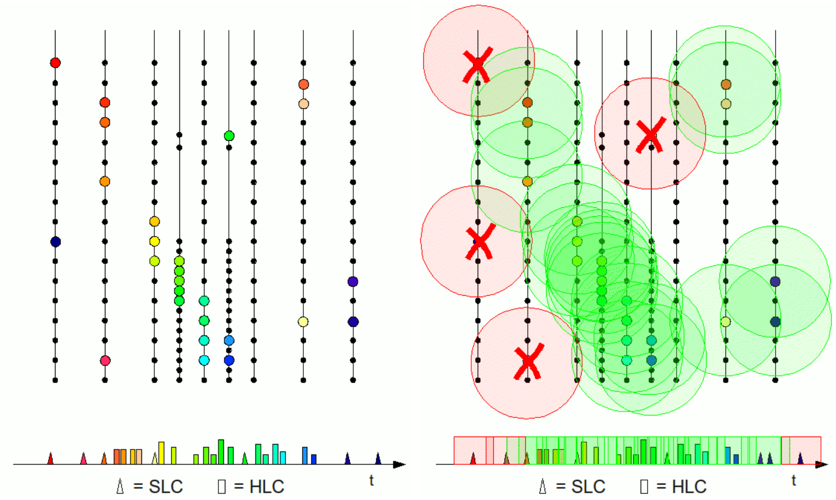

Figure 3.4: The RT-cut as part of the seeded RT-cleaning: SLC hits are discarded if there is no further hit contained within a radius R (shown above) or within a time window T (shown below). The seeded RT-cleaning repeats this process iteratively with every newly acquired SLC hit that survives the previously applied RT-cut (Ref. [Sch10]).

3.2 Ice Properties

The depth in which IceCube was installed was chosen due to measurements of the transparency of the glacial ice. The deep antarctic ice is ultra-transparent and allows light to propagate up to one hundred meters before it is absorbed. Photons scatter at impurities of the ice which are mostly air bubbles or dust particles depending on the depth below the surface. The very deep ice is exposed to a great pressure which cause the air bubbles to disappear. It is thus only the very deep ice which is ultra transparent and well-suited for the detection of Cherenkov light.

The Cherenkov light is created by secondary particles from the neutrino interaction with the nuclei of the ice (c.f. Sec. 2.3). The measurement of a cascade somewhere in the detector is dependent on an accurate model of the ice properties that accounts for the scattering and absorption of the Cherenkov light. For IceCube different ice models and the corresponding detector responses are studied. The properties of the antarctic ice can be modeled by several parameters which all are dependent on the wavelength λ of the photon and on its position x, y, z in the ice. Besides the refraction index, one needs to know the absorption coefficient $a = 1/l_\mathrm{a}$ and the scattering coefficient $b = 1/l_\mathrm{s}$. They are defined as the reciprocal absorption and scattering lengths l_a and l_s, respectively.

The absorption length is the distance after the photon survival probability dropped to $1/\mathrm{e}$. Similarly, the scattering length is the average distance between two scattering processes. Since the scattering in ice is dependent on the size and shape of the air bubbles or dust particles, it is not isotropic. The mean scattering angle $\langle\cos\theta\rangle$ can be calculated using Mie theory [Ice06]. Both the scattering length and the scattering angle cannot be measured independently. Instead, the scattering properties of the ice are measured via the effective scattering length

$$l_\mathrm{e} = \frac{l_\mathrm{s}}{1 - \langle\cos\theta\rangle}, \tag{3.1}$$

after which the scattering becomes isotropic. Therefore, if the light is scattered isotropically, then $l_\mathrm{e} = l_\mathrm{s}$, otherwise $l_\mathrm{e} > l_\mathrm{s}$. The mean scattering angle is $\langle\cos\theta\rangle = 0.8$ for the AHA model which is based on measurements with AMANDA (see below) [Wos08].

The effective scattering coefficient and the absorption coefficient are depicted in Fig. 3.5 in dependence of the depth below the surface and the wavelength. They were measured in a depth of 1200 m to 2200 m for wavelengths between 300 nm and 600 nm by artificial light sources in the AMANDA detector. There are no core samples of the ice for direct measurements available, since the holes for the AMANDA and IceCube strings were drilled with hot water [Ice01]. However, there are some direct measurements of the dust concentration taken with the *dust logger* that was deployed into some of the IceCube holes [W$^+$12].

The basic findings are that the effective scattering length increases drastically at a depth closer to the surface. This is predominantly caused by air bubbles. Due to the high pressure they become instable at depths below 1350 m. The oscillating structure with one larger peak at a depth of about 2050 m is caused by dust layers. These are related to climate changes and volcanic eruptions in the past [Ice06]. The absorptivity follows a similar structure as the effective scattering. At larger wavelengths the light is absorbed heavily and below a wavelength of 470 nm the ice is effectively pure. The remaining absorptivity is also caused by the dust layers which can be seen from the structural comparison between the effective scattering and the absorption in Fig. 3.5.

A comparison between different ice models is shown in Fig. 3.6. Again, the absorption coefficient and the effective scattering coefficient are depicted in dependence of the depth. The Millennium model was the very first ice model based on measurements with the flasher LEDs in AMANDA [Ice06]. The AHA model extends the Millennium model by incorporating experimental data from drill cores which were taken from drill sites about 1 000 km away for the deep regions of the ice below 2 000 m [B$^+$10]. The newer model SPICE1 is a fit to experimental data from the IceCube flasher LEDs. It also incorporates dust logger and drill core data [Chi11]. The IceCube flasher measurements are particularly important for the very deep ice, since this region is below the accessibility of AMANDA and thus not well described by earlier models. The development of improved ice models is an ongoing process leading to the currently newest SPICEMie model which also incorporates Mie scattering into the fit of the flasher data.

The ice properties are described by a table of parameters: the depth below the surface of the ice, the effective scattering coefficient and the absorption coefficient at a wavelength of 400 nm and the temperature difference between two adjacent ice layers. For the calculation of the light distribution between a source and a DOM the data is binned in six dimensions: three space dimensions, the time relative to the photon emission point, the photon emission angle at the source and the incident photon angle when it is measured. For each bin the complete set of parameters necessary to describe the ice properties is saved into a *photorec table*. During the simulation of the photon propagation a software called *Photonics* looks up the listed photon density distributions [LMo07]. This can be very slow for large tables and the interfaces of two ice bins cause the reconstructions to suffer from binning effects. The development of *spline tables* is a new approach which solves both problems by interpolating the photorec tables and fitting a smooth polynomial. The spline tables contain the four before-mentioned ice parameters plus six fit parameters from the table spacings [Chi11].

For the study presented in this thesis both the AHA and the SPICE1 ice models are used in a complementary way. The photon distributions from the AHA model are read from photorec tables with a binning of 40 m in z direction and 20 bins in angular direction. The photon propagation from the SPICE1 model are calculated with spline tables produced from photorec tables with a binning of 20 m in z direction and 10 bins in angular direction.

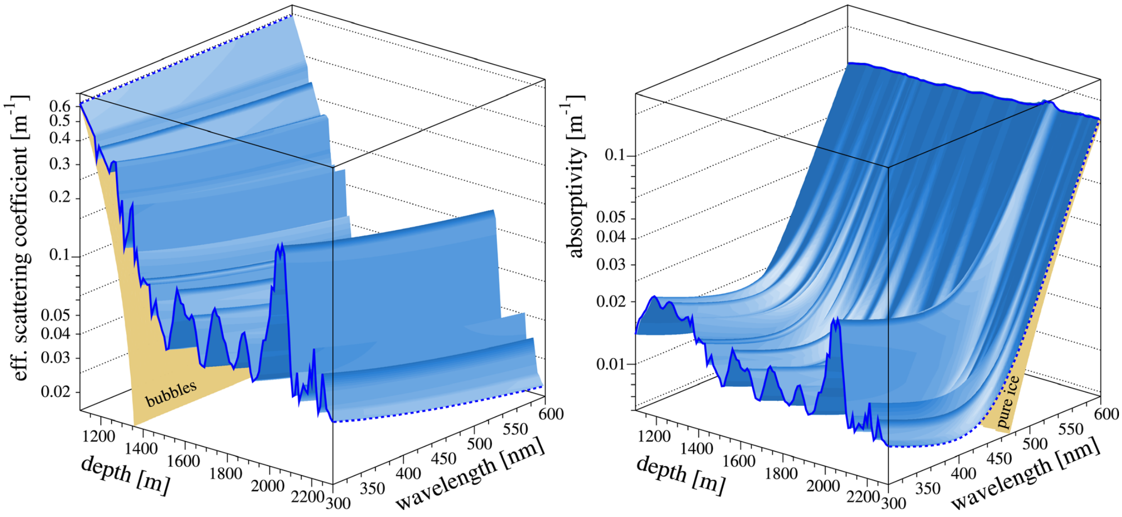

Figure 3.5: The effective scattering coefficient (left) and absorption coefficient (right) measured with AMANDA: They are shown in dependence of the depth below the surface and the wavelength of the light. Both the scattering and absorption are strongly dependent on the depth of the ice and predominantly caused by dust layers of different densities. For the relevant region and sensitivity of IceCube the dependence on the wavelength is rather small (Ref. [Ice06]).

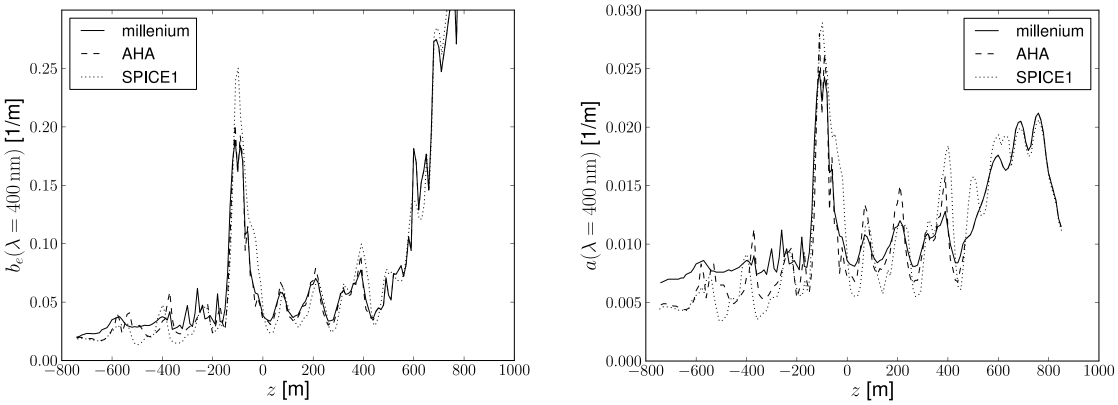

Figure 3.6: The effective scattering coefficient b_e (left) and absorption coefficient a (right) for different ice models: They are measured at a wavelength of 400 nm in dependence of the depth z with respect to the IceCube coordinate system. The origin corresponds to an approximate depth of 1950 m below the surface. Hence, the dense dust layer as seen in Fig. 3.5 is located at $z \simeq -100$ m (Ref. [Pan11]).

4. Cascade and Track Analyses

The purpose of the IceCube detector is to measure neutrinos of all flavors. The flavor can be identified by different event topologies created by the Cherenkov light pattern in the detector. In general, one distinguishes between tracks and cascades. Tracks are generated by muons propagating through the detector which are either produced by cosmic ray air showers in the atmosphere or by the charged current interaction of a muon neutrino. Muons leave kilometer-long tracks in the detector and are detected by the energy losses along their path. Cascades are generated by the charged current interactions of the electron and tau neutrinos and by all neutral current interactions. This event signature is approximately spherical and point-like compared to the dimensions of the detector. The challenges of the cascade analysis are to separate very few neutrinos from a large background of atmospheric muons and to reconstruct the energy, direction and flavor as precisely as possible.

This chapter gives an overview of the preconditions of the cascade and track analysis which are used for the study presented in this thesis. The first two sections introduce the different event signatures in more detail and describe the simulation properties used for this study. The third section treats the necessary cascade and track reconstruction algorithms as well as emerging cut variables. The last section explains how this knowledge is combined in different cascade filters for a first event selection.

4.1 Event Signatures

There are three different event signatures In IceCube: *tracks*, *cascades* and *double bangs*. Although it is not possible to strictly assign one signature to one neutrino flavor, tracks can be associated with the interaction of muon neutrinos, cascades with electron neutrinos and the double bang with tau neutrinos. As will be discussed, the contribution of each flavor to one signature is complex. The signatures are distinguished by the topology of the detected Cherenkov light as shown in Fig. 4.1 where the charged current interaction $\nu_l + N \to l^- + X$ of a neutrino ν_l with an ice nucleus N produces a lepton $l = e, \mu, \tau$ and a shower X.

Tracks are kilometer-long straight lines associated with high-energy muons. Due to their large momentum they are highly relativistic and thus propagate many kilometers before they decay. Along its path a muon loses energy via ionization and via stochastic processes such as bremsstrahlung, pair production and photo-nuclear interactions. The ionization loss is continuous and constant for high energy muons. Although the radiation length for muons is approximately 15 km (c.f. Sec. 2.3.2), the muon predominantly loses energy via these stochastic interactions. This is is due to the proportionality between the specific energy loss and the muon energy. Therefore, a highly energetic muon loses energy by secondary cascades along its path and the emitted Cherenkov light is detected by the surrounding DOMs. This enables a track-like reconstruction of the muon.

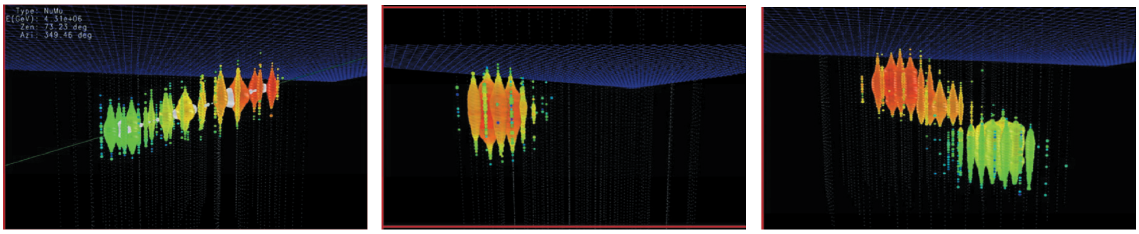

Figure 4.1: IceCube event signatures: Each dot represents a DOM. The colored dots are DOMs which detected Cherenkov photons. The size indicates the detected charge and the color represents the time with red being early and blue late hits. In the left figure a track event from the muon neutrino interaction $\nu_\mu + \mathrm{N} \rightarrow \mu^- + \mathrm{X}$ is shown. The white spheres on the straight line show the stochastic energy losses of the muon. In the middle figure a cascade event from the electron neutrino reaction $\nu_e + \mathrm{N} \rightarrow e^- + \mathrm{X}$ is shown. In the right figure a double bang event from the tau neutrino reaction $\nu_\tau + \mathrm{N} \rightarrow \tau^- + \mathrm{X}$ with the subsequent tau decay $\tau^- \rightarrow \nu_\tau + \mathrm{X}$ is shown. All figures come from simulated events (Ref. [HK10]).

The total energy loss of a muon can be parameterized as

$$\frac{dE}{dX} = -a - bE, \tag{4.1}$$

where a combines the energy loss due to ionization and Cherenkov radiation and b contains the energy loss due to bremsstrahlung, pair production and photo-nuclear interactions. This parametrization is used to estimate the measured energy of a muon traversing the detector. For a muon which starts and stops inside the detector the energy can be estimated by the track length. This is only possible for low-energy muons with a decay length less than 1 km.

Muons can have two different origins, either they are atmospheric or neutrino-induced. Atmospheric muons are the major background for the cascade analysis and outnumber neutrino-induced events by 500 000 : 1 [HK10]. They come from cosmic ray air showers in the atmosphere and are thus only down-going in the detector. This corresponds to a zenith angle of the track which is smaller than 90°. Neutrino-induced muons originate from the charged current interaction $\nu_\mu + \mathrm{N} \rightarrow \mu^- + \mathrm{X}$. Muon neutrinos can be atmospheric as well or they can be of cosmic origin. They are distributed mostly isotropically, since they can propagate through the Earth. Therefore, the zenith angle spectrum is approximately flat except for the peak at the horizon (see Fig. 4.2). The reason is that mesons produced in cosmic air showers at the horizon have a much longer propagation length through the thin atmosphere and thus a higher probability to decay before interacting, increasing the atmospheric neutrino flux.

The neutrino interaction vertex can either be outside of the detector or inside. If it is outside, the detector is only able to measure a track from the muon. The separation from the atmospheric muon background is then possible by taking only up-going muons. These must have been induced by muon neutrinos somewhere inside the Earth. If the vertex is inside the detector, the hadronic cascade X and (depending on the energy) a track of the created muon is measured. This gives a much more precise measurement of the neutrino energy and the reconstruction is not restricted to up-going tracks.

Since muons leave kilometer-long tracks in the detector, it is possible to reconstruct the direction fairly well by the long lever arm. A good muon reconstruction can have an angular resolution down to $\Delta\Omega \lesssim 1°$. An up-going muon is neutrino-induced and its direction is correlated to the neutrino by the Lorentz-factor. Thus, the higher the muon energy, the more exact is the measurement of the original neutrino direction. A good directional resolution for neutrino-induced muons is essential for searching for point sources like supernovae in the optical follow-up program [Fra11].

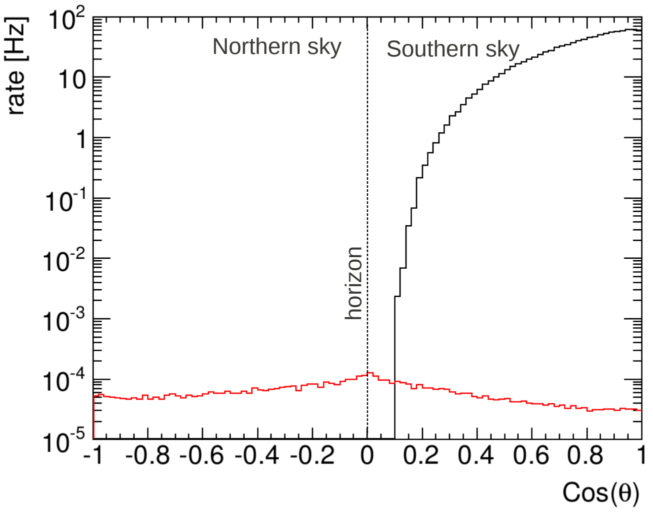

Figure 4.2: The IceCube trigger rate as function of the true zenith angle: Atmospheric muons (black) are restricted to the Southern sky, since they are produced by cosmic ray air showers in the atmosphere and cannot penetrate the Earth. Atmospheric neutrinos (red) are distributed isotropically except for the peak at the horizon as explained in the text. In the IceCube coordinate system the zenith is directed to the Southern sky (Ref. [Fra11]).

Cascades are approximately spherical light patterns and produced by sources that are point-like compared to the dimensions of the detector. These sources are particle showers associated with different interaction types in the detector. One primary cascade is contained in all neutral and charged current neutrino interactions. The cascade signature of a contained muon neutrino also contains a track from the muon and a highly energetic tau neutrino produces another cascade from the tau decay (see double bang below).

The purest cascade signatures are produced by the neutral current interactions $\nu_l + N \rightarrow \nu_l + X$ of all flavors $l = e, \mu, \tau$ and by the charged current interaction $\nu_e + N \rightarrow e^- + X$ of the electron neutrino. The neutral current interactions produce a hadronic cascade which looks the same for all flavors. In the charged current interaction the electron neutrino produces an electron which has a very short radiation length of about 36 cm (c.f. Sec. 2.3.2). The electron produces an electromagnetic cascade which is contained within the hadronic cascade X coming from the ice nucleus. These contributions cannot be separated. The size of the electromagnetic cascade scales logarithmically with the electron energy. For example, an electron with an energy of 1 TeV causes a cascade with a diameter of about 10 m.[1] Compared to the dimensions of the detector in the order of 1 km the resulting cascade is approximately point-like. However, the light pattern is not point-like because the produced light propagates through the detector. For contained cascade events the energy resolution is very good, since the complete energy is deposited inside the detector. The neutrino energy can be reconstructed more precisely for charged current interactions because it is completely transferred to the cascade and less precisely for neutral current interactions due to the escaping neutrino.

Although cascades look approximately isotropic, the direction of the neutrino can be reconstructed from the incident angle of the Cherenkov light. It is emitted at an angle of $\theta_{\mathrm{Ch}} = 41^\circ$ with respect to the secondary particles of the cascade (c.f. Sec. 2.3.3). The angular resolution is roughly $\Delta\Omega \simeq 30^\circ$ and thus much worse than for tracks.

---

[1] This is calculated using Eq. (2.39) and the subsequent relations in Sec. 2.3.2. The diameter of the cascade is determined by $d = \ln(E_0/E_c)/\ln 2 \cdot X_0$ with the exemplary primary energy $E_0 = 10$ TeV and the radiation length $X_0 \simeq 36$ cm as well as the critical energy $E_c \simeq 79$ MeV for ice.

Double bangs are two subsequent cascades only associated with tau neutrino events. The first cascade is purely hadronic and is caused by the break-up of the ice nucleus in the neutrino interaction $\nu_\tau + \mathrm{N} \rightarrow \tau^- + \mathrm{X}$. The emerging tau propagates in the detector until it decays. The decay $\tau^- \rightarrow \nu_\tau + \mathrm{X}$ of the heavy tau produces a second cascade, thus naming this signature double bang. The decay length of the tau is dependent on its energy. For example, a tau with an energy of 1 PeV has a decay length of about 50 m.[2] The decay length would be short enough that the tau lepton does not leave a track, but long enough to observe two separate cascades. However, these high-energy events are very rare and have not been observed yet. More likely, tau neutrinos will be observed at lower energies such as 10 TeV. In this case the decay length of the tau decreases to 50 cm making it impossible to separate the two subsequent cascades from each other. Most tau neutrino events, therefore, look like normal cascades.

In conclusion, track signatures have good directional resolution due to the long lever arm. This is very important for any point source analysis. However, most events do not start and stop in the detector which makes an energy estimation very rough. Cascade signatures on the other hand have a worse directional resolution but a more precise energy measurement, since the total energy of the cascade is contained within the detector. The double bang signature is very rare and has not been observed yet. Most of the tau neutrino events look like single cascades. Roughly two third of all neutrino events modeled from a cosmic neutrino flux are cascade-like which stresses the importance of the cascade analysis.

4.2 Monte Carlo Simulations

The IceCube analysis is performed in a blind manner in order to avoid biases. It means that the analysis is optimized without using the experimental data. Instead, only Monte Carlo (MC) simulations are used for cut optimizations and other studies. For a consistency check a subset of experimental data, the so-called *burnsample*, is available for the individual analysis. It contains 10% of the experimental data for one year of livetime. After the cut optimization and its approval by chosen reviewers from the collaboration, the analysis is performed on the complete dataset in the *unblinding process*.

The simulated events used for this thesis are generated by the *Cosmic Ray Muon Generator* which is a modified version of the *Cosmic Ray Simulations for Kascade* (CORSIKA) for atmospheric muons [HP09] and by the *Neutrino Generator* (NUGEN) which is based on *All Neutrino Interaction Simulation* (ANIS) for all neutrinos [GK05].

Each simulated event starts with the generation of a primary particle. In CORSIKA, this is a cosmic ray particle interacting with a nucleus in the atmosphere and producing a particle shower. From the shower only the muons are propagated through the atmosphere and the ice into the detector by the *Muon Monte Carlo Module* (MMC) [CR04]. In NUGEN, the primary particle is a neutrino which is propagated through the Earth into the detector. All interactions such as the stochastic energy losses of a traversing muon or the cascade from a neutrino interaction are simulated. Then the yield and the propagation of the Cherenkov light from the source to the DOMs are calculated using Photonics (c.f. Sec. 3.2) and the response of the detector electronics is simulated [LMo07]. The simulation forces all particles to interact within a cylinder of 1000 m radius and 2000 m length, centered at the detector origin and oriented in parallel to the direction of the primary particle [Pan11]. This way it is also taken into account what the light pattern looks like from a source outside of the detector.

---

[2] The decay length is defined as $l = \beta\gamma c\tau$ where γ is the Lorentz factor and τ the lifetime. One obtains $l \simeq 50$ m for the tau with $\beta \simeq 1$ and $\gamma = E/m$ using $m = 1777$ MeV and $\tau = 2.9 \cdot 10^{-13}$ s [Par08].

The CORSIKA simulation files used for this thesis are generated with the polygonato model from Hörandel [H0̈3], which incorporates all primary nuclei from ^{1}H to ^{56}Fe. Each element has a different flux and power-law index according to the cosmic ray flux as described in Sec. 2.1.1.[3] The simulation files used are unweighted, i.e. there is no over-sampling of higher energy particles. Furthermore, the simulation files contain coincident events which account for the case that while the detector is measuring one muon there is another muon traversing the detector in the same trigger window.

The NUGEN simulation files used for this thesis are generated with an E^{-2} spectrum. There are, in general, also simulation files which are generated with an E^{-1} spectrum to over-sample events at higher energies. Neutrino are forced to interact, since an unweighted simulation with such low cross sections would not be feasible. The simulated events need to be reweighted during the analysis by modeling a neutrino spectrum such as E^{-2} for astrophysical neutrinos and $E^{-3.7}$ for atmospheric neutrinos (c.f. Sec. 2.2). The astrophysical neutrino flux is expected to be isotropic and the atmospheric is dependent on the zenith angle. The reweighting using the simulation weights is described next.

The simulation weights are calculated by additional weight modules that are appended to the event generators. Each event i carries a certain weight w_i which is a measure of the probability that it is triggered by the detector. Several events are joined in one simulation file j. The number of generated simulation files is a measure of the total number of events.

For muon events generated by CORSIKA each weight is calculated as

$$w_i = \frac{\mathrm{Weight}_i \cdot \mathrm{DiplopiaWeight}_i}{\sum_j \mathrm{Timescale}_j}. \tag{4.2}$$

Weight_i contains all the information about the weight of a specific event which can include over-sampling of higher energies. $\mathrm{DiplopiaWeight}_i$ accounts for the coincidence of muon events. For a single muon event this acts as a correction to the simulated livetime in the sense that a single event is part of a coincident event and, hence, must not be counted separately. For a multiple muon event the weight corresponds to the probability that a single event actually occurs in combination with other uncorrelated muon events [DV12]. $\mathrm{Timescale}_j$ may be different for separate files, but is the same for all events in one file. It is a measure of the frequency of how often the simulated muon event occurs. The effective livetime[4] of all simulation files is given by $T = \sum_j \mathrm{Timescale}_j$. Therefore, the total number of triggered events is $N_{\mathrm{trigger}} = T \cdot \sum_i \mathrm{w}_i$. In unweighted simulation files the Weight_i is equal to one.

For neutrino events generated by NUGEN each weight is calculated as

$$w_i = \frac{\Phi_i \cdot \mathrm{OneWeight}_i}{\sum_j \mathrm{NEvents}_j}. \tag{4.3}$$

$\mathrm{OneWeight}_i$ contains all the information about the weight of a specific event to match any desired flux Φ_i. It is calculated by the event generator and contains all relevant factors such as generation volume, spectral index and interaction probabilities [Fin07]. Its units are GeV cm^2 sr. $\mathrm{NEvents}_j$ is the number of generated events in one file j. The neutrino flux needs to be modeled for astrophysical or atmospheric neutrinos. The atmospheric neutrino flux is calculated by the *NeutrinoFlux* project [Ter10] using the Honda (2006) model [H$^+$07] for the conventional and the Sarcevic model [ERS08] for the prompt flux. It depends on the energy, the zenith angle

---

[3] The newer five component model only incorporates the dominant primary nuclei ^{1}H, ^{4}He, ^{14}N, ^{27}Al and ^{56}Fe in order to simplify the simulation production and to save processing time.

[4] The effective livetime is defined as the detector livetime at which the statistical errors of the Monte Carlo simulations and the experimental data become equal.

and the type of the neutrino. The cosmic neutrino flux is modeled much simpler, since it is unknown. It is independent from the zenith angle and the flavor of the neutrino for a diffuse flux (c.f. Sec. 2.2.1 and 2.2.3). The energy spectrum is modeled as E^{-2} and the normalization of the flux is set by the current upper limit [Mid12]. The flux value for the weight of an astrophysical neutrino in Eq. (4.3) is calculated by $\Phi_i = 4 \cdot 10^{-8}\,\mathrm{GeV\,cm^{-2}\,s^{-1}\,sr^{-1}}\,E_i^{-2}$ with the neutrino energy E_i of the event i.

The trigger rate for weighted simulation files is simply the sum over all weights

$$R = \sum\nolimits_i w_i. \tag{4.4}$$

It is measured in Hz, since it is integrated over all energies and angles. In the unweighted case the trigger rate is given by $R = N_{\text{trigger}}/T$ as can be seen by comparing Eq. (4.2) and (4.4).

The effective livetime for weighted simulation files is calculated by

$$T_{\text{eff}} = \frac{\sum_i w_i}{\sum_i w_i^2}. \tag{4.5}$$

It is defined as the livetime at which the statistical error for experimental data and Monte Carlo data become equal. In the unweighted case the effective livetime is given by $T_{\text{eff}} = N_{\text{trigger}}/R$ as can be seen by comparing Eq. (4.2) and (4.5).

The statistical errors for weighted simulation files are calculated by [BZ10]

$$\sigma = \sqrt{\sum\nolimits_i w_i^2}. \tag{4.6}$$

The error is calculated for each bin of a specific distribution where each error only includes the weights for that bin. In the unweighted case the error comes from the Poisson distribution. Comparing Eq. (4.2) and (4.6) shows that this gives $\sigma = \sqrt{N_{\text{trigger}}}/T$, as expected.

4.3 Reconstruction Algorithms

The IceCube analysis is based on the software *IceRec* [Sch05] which contains all data classes, tools and services needed for reconstructions and filter implementation. IceRec is written in C++ and provides interfaces to Python. It is structured in a modular way similar to Python. All reconstructions, tools and filters are collected in *I3Modules*. Another module called *IceTray* collects all desired modules in a chain and calls each module one after another. This allows easy to use scripts where the result of one reconstruction can be immediately used as a seed for the next. The module chain applies any reconstruction event by event and is also able to filter events on customized selection criteria. The study presented in this thesis is implemented using IceRec 04-01-00 and Python 2.7.2.

The following sections describe the reconstruction algorithms used for this thesis. The first step is the feature extraction which reconstructs photo electrons from the recorded waveforms of the PMT. After obtaining the photon hit information in form of a *pulse map*, simple first guess algorithms are used for a low-level event selection. They are also used as seeds for the more sophisticated maximum likelihood reconstructions. These algorithms are divided by their purpose to reconstruct either tracks or cascades as described in the subsequent sections. It will be explained how these reconstructions work and which cut parameters emerge.

4.3.1 Feature Extraction

The first step of any reconstruction is the evaluation of the recorded waveforms in three ATWD channels with different gains and one fADC channel with a coarser time binning (c.f. Sec. 3.1.2). The reconstruction of single photo electrons is depicted in Fig. 4.3. The goal is to extract the times, charges and widths of the pulses and to obtain the number and time distribution of the photo electrons by a deconvolution of the calibrated waveforms.

In the first step the ATWD channels are combined by taking the value with the highest unsaturated gain for each bin. The still raw PMT waveforms are then transformed from bins and counts into times and voltages, respectively. The correction of electronic effects such as the transit time (c.f. Sec. 3.1.1) are taken into account by the *DOMCalibrator* [Rou07]. In the second step a Bayesian unfolding with a standard pulse form is applied on the calibrated waveform to extract pulses from single photo electrons [Chi12]. The sum over all single pulses gives the same charge as the calibrated waveform. This is performed by the *FeatureExtractor* and gives a set of pulses extracted from the ATWD channels [Rou07]. If the fADC channel recorded later hits, the feature extraction is combined for the ATWD and fADC pulses.

The *NewFeatureExtractor* (NFE) was developed to account for the complexity of waveforms and uses different algorithms depending on its shape [Wal10]. A pulse matching the standard pulse form is tagged as simple. All other waveforms which exceed a certain threshold, are too wide or too close together are tagged as complex, i.e. these waveforms contain overlapping hits. The advantage of the NFE is that the processing time which is saved for simple waveforms can be used for more sophisticated algorithms on complex waveforms.

The final result is a pulse map that contains all extracted pulses from the ATWD and fADC channels for each hit DOM of one event. A pulse is now defined by its charge, width and starting time. Important quantities that are obtained from the pulse map are the total charge Q_{tot} and the number of channels N_{Ch}. The total charge is the sum over all extracted pulses from every DOM and the number of channels is the number of DOM launches (c.f. Sec. 3.1.2). Both are measures of the total deposited energy in the detector (see Sec. 4.3.3). The pulse map obtained from the feature extraction is cleaned using the seeded RT-cleaning (c.f. Sec. 3.1.2) and then used for all further reconstructions which will be discussed in the following sections.

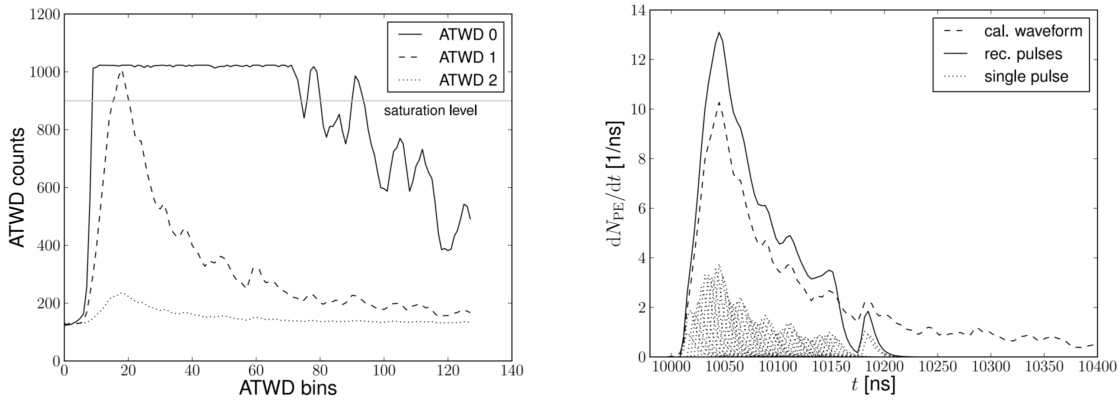

Figure 4.3: Feature extraction from the ATWD waveforms: The left figure shows the three different ATWD channels that record the PMT hits. Each channel has a different gain to cover a broad dynamic range. The right figure shows the different steps of the feature extraction. In the first step all channels are combined, known effects from the electronics are corrected and the ATWD counts are converted into charges (dashed line). With Bayesian unfolding all single pulses are extracted (dotted line). The sum of all single pulses gives the total reconstructed waveform (solid line) (Ref. [Pan11]).

4.3.2 Maximum Likelihood Reconstructions

The goal of any reconstruction is to find the type of event that explains the measured detector response best. Sophisticated reconstruction algorithms maximize a specifically defined likelihood using two different parameter sets. One describes the data given by the detector response and the other characterizes the reconstructed event. They are connected via the expected light distribution calculated by Photonics.

The parameter set $\mathcal{D}$ given by the detector response includes the number of photo electrons for all hit DOMs over time. The calibrated waveform gives the number of photo electrons n_{oi} per DOM o and time bin i (see Sec. 4.3.1). The full dataset also contains the position $\vec{r}_o$ of the DOM as well as the starting time t_{oi} and width Δt_{oi} for each bin. The total parameter set for the detector response is

$$\mathcal{D} = \{\vec{r}_o, t_{oi}, \Delta t_{oi}, n_{oi}\}. \tag{4.7}$$

The parameter set $\mathcal{C}$ for the reconstructed cascade has seven parameters. The vertex position $\vec{r}$ comprises three parameters x, y and z. The fourth is the time t of the interaction and the direction is given by the azimuth angle φ and the zenith angle θ. The last parameter is the cascade energy E. The total parameter set for the reconstructed event is

$$\mathcal{C} = (\vec{r}_\mathrm{c}, t_\mathrm{c}, \theta_\mathrm{c}, \varphi_\mathrm{c}, E_\mathrm{c}). \tag{4.8}$$

The position (x, y, z) and the direction (θ, φ) are measured with respect to the IceCube coordinate system as depicted in Fig. 4.4. It is a right-handed Cartesian coordinate system which has its origin close to the geometric center of the detector. The zenith angle is measured with respect to the z axis pointing towards the surface of the ice [Wos12]. The energy E belongs to a reference cascade which comprises the total amount of Cherenkov light originating from the reconstructed vertex. In case of the charged current interaction the neutrino deposits its total energy in the detector and the energy of the reference cascade is equal to the neutrino energy. In the neutral current interaction, however, the neutrino only transfers a fraction of its energy to the hadronic cascade. In this case, the reconstructed energy only gives an estimate on the neutrino energy.

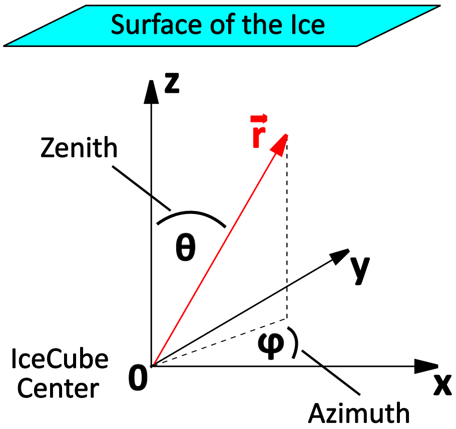

Figure 4.4: The IceCube coordinate system: It is right-handed Cartesian coordinate system with its origin close to the geometric center of the detector. The z axis points towards the surface of the ice. The y axis points Grid North towards Greenwich, UK, and the x points Grid East. The center is located at 46 500 ft E, 52 200 ft N in UTM system, at an elevation of 2900 ft (corresponding to a depth of 1948.07 m below the surface of the ice) [Wos12].

The likelihood function relates the measured data to the parameter set that represents the fit to the data. Let $\mathbf{d} \in \mathbb{R}^{N_d}$ be the dataset with N_d data points and $\mathbf{c} \in \mathbb{R}^{N_c}$ be the set of N_c parameters which are fitted. The likelihood function is defined as the product over each probability to measure the data point d_i [Bar08]

$$L(\mathbf{c}|\mathbf{d}) = \prod_{i=1}^{N_d} p(\mathbf{c}|d_i), \tag{4.9}$$

where the *probability density function* (pdf) $p(\mathbf{c}|\mathbf{d})$ is evaluated at each point d_i for a given set of fit parameters $\mathbf{c}$. In IceCube the parameter sets for the cascade reconstruction are identified with the likelihood variables as $\mathbf{d} = \mathcal{D}$ and $\mathbf{c} = \mathcal{C}$ and the measured Cherenkov light is described with Poisson statistics [Bar08]. The pdf is, therefore, given by

$$p(n|\mu) = \frac{\mu^n}{n!} \mathrm{e}^{-\mu}, \tag{4.10}$$

where n is the measured and μ the expected number of photo electrons. With Eq. (4.9) and (4.10) the likelihood function becomes [Pan11]

$$L(\mathbf{c}|\mathbf{d}) = \prod_{\substack{o\,\in\,\text{hit}\\ \text{DOMs}}} \prod_{\substack{i\,\in\,\text{time}\\ \text{bins}}} \frac{\mu_{oi}^{n_{oi}}}{n_{oi}!} \mathrm{e}^{-\mu_{oi}} \prod_{\substack{o\,\in\,\text{unhit}\\ \text{DOMs}}} \mathrm{e}^{-\mu_o}, \tag{4.11}$$

with the expected number of photo electrons per DOM o summed over all time bins i [Mid08]

$$\mu_o = \sum_{\substack{i\,\in\,\text{time}\\ \text{bins}}} \mu_{oi} \simeq \langle \mu_o^\infty \rangle + \nu_{\text{noise}} \Delta t_{\text{event}}. \tag{4.12}$$

The first term gives the total number of expected photons from the source at the DOM (although there are none measured) and the second term accounts for the noise with the frequency ν_{noise} through the duration Δt_{event} of the event.

The number of expected photo electrons is described by the propagation of the Cherenkov light from the source to the DOM. The residual time is

$$t_{\text{res}} = t_{oi} - t_{\text{geo}} - t_{\text{c}}. \tag{4.13}$$

The first part is the arrival time t_{oi} of a photon at the DOM o in the time bin i. The geometrical time $t_{\text{geo}} = |\vec{r}_o - \vec{r}_{\text{c}}|/c$ is the time which the photon would would need from the cascade to the DOM without being scattered (c is the speed of light in ice). The last part is the starting time t_c of the photon at the cascade.

For bulk ice[5] the light propagation is parameterized by the *Pandel function* given by [Pan96]

$$\frac{\mathrm{d}P}{\mathrm{d}t}(r,t) = \frac{a(at)^{b-1}\mathrm{e}^{at}}{\Gamma(b)}. \tag{4.14}$$

The variables r and t represent the distance and the propagation time, respectively, between the cascade and the DOM. Γ is the gamma distribution. The parameters are given by $a = 1/\tau + c/l_{\text{a}}$ and $b = r/l_{\text{s}}$ where τ can be interpreted as the scattering time, l_{s} the scattering length and l_{a} the absorption length. The speed of light in ice is denoted by c. The values are $\tau = 450$ ns, $l_{\text{s}} = 47$ m and $l_{\text{a}} = 98$ m as taken from a fit to AMANDA-II experimental data [Kow03].

---

[5] The term *bulk ice* refers to an optically homogeneous ice model without any dependence on the depth z. The layered structure of the ice due to the dust layers is taken into account by the photorec tables (c.f. Sec. 3.2).

The expected number of photo electrons per DOM and time bin is then given by [Mid08]

$$\mu_{oi}(\vec{r}_o, t_{oi}, \mathbf{c}) = \left(\langle \mu_o^\infty \rangle \frac{\mathrm{d}P}{\mathrm{d}t}(|\vec{r}_o - \vec{r}_\mathrm{c}|, t_{oi} - t_\mathrm{geo} - t_\mathrm{c}) + \nu_\mathrm{noise} \right) \Delta t_{oi}. \tag{4.15}$$

For each event the likelihood is calculated multiple times for different values of **c**. Depending on the available processing time this can be iterated many times with all parameters set free or some fixed. The above depicted calculation reconstructs the vertex of the cascade. The reconstruction of the energy is implemented in a similar way using the fact that the expected number of photo electrons scales linearly with the cascade energy. The reconstruction of the cascade direction incorporates the angle between the cascade direction and the vector $\vec{r}_\mathrm{o} - \vec{r}_\mathrm{c}$ linking the cascade with each DOM. The fit result for the cascade event is described by the parameter set $\mathcal{C}$ for which the likelihood is maximal.

Due to numerical limitations the negative logarithm of the likelihood is minimized to find the optimal solution. This way the product of lots of very small numbers becomes a sum over numbers with a manageable size. For convenience, the quantity

$$\mathrm{logl} = -\log L \tag{4.16}$$

is defined in the IceCube analysis, i.e. the maximum likelihood corresponds to the minimum logl value. For each event the likelihood minimizer yields the reconstructed cascade and the value of the likelihood. In analogy to a χ^2 fit, one defines the *reduced log-likelihood*

$$\mathrm{rlogl} = -\frac{\log L}{f} \qquad \text{with} \qquad f = N_d - N_c \tag{4.17}$$

as a quality parameter to the fit. The smaller the value the better the agreement between the experimental data and the reconstructed cascade hypothesis.

A problem of the likelihood reconstruction can be that the minimizer finds a local instead of a global minimum. Several iterations with different starting values can be used to avoid this problem. As will be described in the following sections, many reconstruction algorithms are based on the maximum likelihood method. The *Gulliver* framework was established in the IceCube analysis software to combine these different reconstruction modules [Boe12]. It contains four different components that every likelihood reconstruction uses:

- seed preparation,
- minimizer algorithm,
- parametrization of fittable physical variables,
- likelihood function.

The seed preparation builds the first parameter set $\mathcal{C}$ which the minimizer starts with. The minimizer is the algorithm that finds the numerical solution to an optimization problem. The physical variables in the likelihood function are mapped to the parameter space which the minimizer works on. This parameter space is defined by introducing variable bounds on the cascade parameter set or by fixing variables to a specific value (and by that excluding them from the fittable parameter space of the minimizer).

In general, fast first guess algorithms are needed to provide a good seed for the expensive likelihood reconstructions. These non-likelihood based methods are as important, since many simple reconstructions offer powerful cut variables. The main idea for reconstructing cascade events, therefore, is to start with fast and simple first guess algorithms. The emerging cut variables can already be used to reduce the background significantly. With fewer events it is possible to use the results from the first guess algorithms as seeds for the more sophisticated maximum likelihood reconstructions. This will be described in the following sections.

4.3.3 Cascade Reconstruction Algorithms

Center of gravity is a first guess algorithm for the cascade vertex reconstruction [Rut11]. It is adapted from classical mechanics where the measured pulses are regarded as point masses at the positions of the hit DOMs. The timing information is completely neglected, instead only the amplitude of each PMT pulse is used. One can calculate the center of gravity as

$$\vec{r}_{\mathrm{COG}} = \frac{\sum_{i=1}^{N_{\mathrm{d}}} a_i \vec{r}_i}{\sum_{i=1}^{N_{\mathrm{d}}} a_i}, \tag{4.18}$$

where N_{d} is the number of pulses, a_i the amplitude and $\vec{r}_i$ the position of each pulse. The center of gravity is basically the sum over the positions of all hit DOMs each weighted with the total measured charge.

Tensor of Inertia is a first guess algorithm that allows the separation of cascade-like from track-like events [Gru11]. It is based on the same idea as the center of gravity by using the charged weighted DOMs for a virtual mass distribution. The tensor if inertia is calculated as

$$I^{k,l} = \sum_{i=1}^{N_{\mathrm{d}}} a_i (\delta^{kl} |\vec{r}_i|^2 - r_i^k r_i^l), \tag{4.19}$$

where $k, l \in \{1, 2, 3\}$ are the indices of the tensor corresponding to the three axes and δ^{kl} is the Kronecker symbol. The eigenvalues I_1, I_2 and I_3 of the tensor are the sizes of the axes in the center-of-gravity system. If one eigenvalue is much larger than the others, the hit pattern is track-like. If all eigenvalues have about the same value, the hit pattern looks spherical and is thus cascade-like. This relation is quantified by the eigenvalue ratio

$$q = \frac{I_1}{I_1 + I_2 + I_3} \qquad \text{with} \quad I_1 \leq I_2 \leq I_3. \tag{4.20}$$

For tracks I_1 is very small and thus q close to zero. A perfectly spherical event has $q = 1/3$ with $I_1 = I_2 = I_3$. Since cascades are not perfectly spherical most of them are below this value. The axis with the greatest eigenvalue is a first estimate on the cascade direction.

Fill Ratio is another first guess algorithm to estimate how spherical an event looks like [Rut11]. The main idea is to take a reconstructed cascade vertex $\vec{r}_{\mathrm{c}}$ and calculate the distribution of hit DOMs around that vertex as

$$r_{\mathrm{mean}} = \frac{1}{N_{\mathrm{d}}} \sum_{i=1}^{N_{\mathrm{d}}} |\vec{r}_{\mathrm{c}} - \vec{r}_i|. \tag{4.21}$$

The mean distance from the vertex is then multiplied with an empirical factor α coming from optimization studies.[6] The value $r = \alpha r_{\mathrm{mean}}$ defines the radius of a sphere around the reconstructed cascade vertex, which can be much larger for long tracks due to the wider distribution of DOM hits around the vertex. The fill ratio is defined as the number of hit DOMs inside the sphere divided by the number of all DOMs in the sphere

$$f = \frac{N_{\mathrm{hit}}}{N_{\mathrm{all}}}. \tag{4.22}$$

For track-like events f is rather small, since many hits are outside of the sphere. Cascade-like events give a fill ratio close to one.

---

[6] It makes sense to perform a cut optimization using the fill ratio separately for contained and uncontained events, since the requirement on the fill ratio can be looser for hit patterns at the edge of the detector. See Sec 4.4 for more information on cuts on the fill ratio and vertex containment.

CFirst is another first guess algorithm for the reconstruction of the cascade interaction time [Kow03]. The idea is to estimate the starting time t_c of the cascade by using the center of gravity for calculating the geometrical time as in Eq. (4.13). The residual time is calculated as

$$t_\mathrm{res} = t_{oi} - t_\mathrm{c} - \frac{|\vec{r}_\mathrm{cog} - \vec{r}_{oi}|}{c}, \tag{4.23}$$

with the position $\vec{r}_{oi}$ and starting time t_{oi} for each pulse i and DOM o (as before c is the speed of light in ice). The vertex time is calculated by counting the number of direct hits within a radius of 100 m around the center of gravity. A direct hit is defined as a pulse with a residual time of $0 \leq t_\mathrm{res} \leq 200$ ns. If there are more than three direct hits within this sphere, the resulting cascade time t_c is taken from the hit with the smallest residual time t_res. Otherwise the smallest hit time t_{oi} within a sphere of 1 000 m radius is used as the cascade time.

CLast is a complete first guess cascade reconstruction [Toa11]. The algorithm builds a reference cascade by using the center of gravity as vertex, the axis with the highest eigenvalue from the tensor of inertia as direction and the starting time from CFirst. Furthermore, a first estimate on the energy is parameterized by a polynomial using N_Ch as the number of launched DOMs [Mid08]

$$\log(E_\mathrm{c}\,[\mathrm{GeV}]) = 1.7 + 0.7x^2 + 0.03x^3 \quad \text{with} \quad x = \log(N_\mathrm{Ch}). \tag{4.24}$$

The complete seven parameter cascade reconstruction with the vertex, direction, time and energy is used as seed for the more sophisticated likelihood reconstruction *CascadeLlh*.

CascadeLlh is a likelihood-based algorithm which is used for an improved reconstruction of the cascade time, vertex and direction [Gre11]. Its likelihood is defined as described in Sec. 4.3.2. The minimizer used is the *Powell* algorithm and the pdf is *UPandel*. All components are part of the Gulliver framework [Boe12].

ACER is a likelihood-based algorithm which is used to reconstruct the cascade energy [D'A11]. It incorporates the ice model by the use of the photorec tables via Photonics. Differentiating logl with respect to the cascade energy E_c gives an equation that is solved numerically

$$-\sum_{o=1}^{N_\mathrm{Ch}} \frac{n_o}{E_\mathrm{c} + \frac{\nu_\mathrm{noise}\Delta t_\mathrm{event}}{A_o}} + \sum_{o=1}^{N_\mathrm{Ch}} A_o = 0, \tag{4.25}$$

where n_o is the total number of measured photo electrons at the launched DOM o and A_o is the expected light amplitude at the DOM position calculated by Photonics [D'A11]. The duration of the event is given by Δt_event, the noise rate is given by ν_noise and N_Ch is the total number of launched DOMs. For an energy reconstruction the timing is neglected and only the total charge detected at each DOM is used. The most important parameter of the ACER reconstruction is the noise rate. For this thesis it is set to an empirical value of $\nu_\mathrm{noise} = 700$ Hz (c.f. Sec. 3.1.1).

Credo is a likelihood-based algorithm in the Gulliver framework which is used for an improved reconstruction of the complete seven parameter cascade [Mid08]. It uses a Poisson likelihood as defined in Eq. (4.11) and fits the time, vertex, direction and energy of the cascade. It incorporates the ice model by the use of photorec tables via Photonics. The seed is composed of different prior reconstructions. For this thesis the time, vertex and direction seeds come from the CascadeLlh reconstruction. The result from ACER is used as energy seed. The Credo reconstruction is able to fit all seven parameters and can be run with multiple iterations.

Monopod is another likelihood-based algorithm which is derived from the Credo reconstruction [vS12b]. It is a single-source specialization of the general *Millipede* likelihood (see Sec. 4.3.4). It also uses a Poisson likelihood for all pulses and fits all seven parameters. Whereas the time, vertex and direction are minimized numerically using Gulliver, the energy is determined by an analytical approach. Furthermore, unlike the ACER and Credo reconstructions, the Monopod reconstruction does not need an explicit noise rate. Instead, the hardware calibration from each simulation or data run is used. Since the algorithm is able to handle noise on its own, it makes more sense to use uncleaned pulse maps for the reconstruction. In addition, the Monopod reconstruction is used with the spline tables instead of the coarse photon tables (c.f. Sec. 3.2). Consequently, it is much more flexible in cascade reconstructions and might in fact replace the Credo reconstruction in future analyses.

4.3.4 Track Reconstruction Algorithms

LineFit is a simple first guess algorithm for a track reconstruction [Lan11]. The light is assumed to be emitted in a plane perpendicular to the track without taking the Cherenkov geometry into account. The plane moves along the track with the vertex $\vec{r}$ and the velocity $\vec{v}$. The algorithm then calculates the χ^2 between the track hypothesis and the data points defined by the arrival time t_i and the position $\vec{r}_i$ of the measured pulse i

$$\chi^2 = \sum_{i=1}^{N_\mathrm{d}} (\vec{r} + t_i \vec{v} - \vec{r}_i)^2. \tag{4.26}$$

The minimization of χ^2 gives an analytical result for the track with

$$\vec{v} = \frac{\langle \vec{r}_i t_i \rangle - \langle \vec{r}_i \rangle \langle t_i \rangle}{\langle t_i^2 \rangle - \langle t_i \rangle^2} \qquad \text{and} \qquad \vec{r} = \langle \vec{r}_i \rangle - \vec{v} \langle t_i \rangle , \tag{4.27}$$

where $\langle x_i \rangle$ denotes the average of x. In contrast to the calculation of the center of gravity, the positions of the pulses are not weighted with their amplitudes due to a better discrimination between signal and background [MP09]. This discrimination is possible because the LineFit yields a track velocity. Only real muons have a velocity that can be matched to the speed of light. Cascades and noise yield a track velocity that is less or greater than the speed of light. The LineFit is a fast and powerful first guess track reconstruction providing the velocity as a cut variable to reduce the muon background significantly at an early analysis stage.

SPEFit is a likelihood-based reconstruction of tracks implemented in Gulliver [GBH08]. It fits the time, vertex and direction of the track. The track energy is determined by other reconstruction modules such as Millipede via the specific energy loss $\mathrm{d}E/\mathrm{d}X$ of a muon (see below). The light propagation is estimated by the Pandel function. For the SPEFit only the total charge and the time of the first hit per DOM are used.

MPEFit is a likelihood-based reconstruction which is based on the SPEFit [GBH08]. The difference is that, instead of only the first hit, all pulses of a DOM are used. This increases the accuracy of the reconstructed track, but also the processing time of the fit. The MPEFit is used for track reconstructions at more advanced stages.

Millipede is a likelihood-based algorithm for the reconstruction of the specific energy loss along a track [Whi11]. A muon loses energy by continuous ionization and by stochastic interactions (c.f. Sec. 2.3.2). The observed waveform in each DOM is a linear combination from all these contributions. The algorithm uses all the information available from the waveform for the energy reconstruction.

The Millipede algorithm divides a track into segments and determines the energy of a single cascade in each segment as depicted in Fig. 4.5. If the photon arrival times are neglected each DOM $o \in \{1, \dots, m\}$ has a total charge $N_o = \sum_i n_{oi}$, where n_{oi} is the number of photo electrons per time bin i. The superposition of all cascade energies E_k from the segments $k \in \{1, \dots, n\}$ weighted with the photon distribution $B_k(\vec{r}_o)$ gives the total charge per DOM:

$$\begin{pmatrix} B_1(\vec{r}_1) & B_2(\vec{r}_1) & \dots & B_k(\vec{r}_1) & \dots & B_n(\vec{r}_1) \\ B_1(\vec{r}_2) & B_2(\vec{r}_2) & \dots & B_k(\vec{r}_2) & \dots & B_n(\vec{r}_2) \\ \vdots & \vdots & \ddots & \vdots & \ddots & \vdots \\ B_1(\vec{r}_o) & B_2(\vec{r}_o) & \dots & B_k(\vec{r}_o) & \dots & B_n(\vec{r}_o) \\ \vdots & \vdots & \ddots & \vdots & \ddots & \vdots \\ B_1(\vec{r}_m) & B_2(\vec{r}_m) & \dots & B_k(\vec{r}_m) & \dots & B_n(\vec{r}_m) \end{pmatrix} \begin{pmatrix} E_1 \\ E_2 \\ \vdots \\ E_k \\ \vdots \\ E_n \end{pmatrix} = \begin{pmatrix} N_1 \\ N_2 \\ \vdots \\ N_o \\ \vdots \\ N_m \end{pmatrix} . \tag{4.28}$$

This linear equation system can be solved analytically by inverting the matrix. Since this can become very complex, the algorithm minimizes the norm of the difference $|\mathbf{a} - \mathbf{b}|$ between both vectors on the left- and right-hand side of Eq. (4.28) instead. The reconstruction of the energy loss along a given track as described is a pure energy fit which only uses the total amplitudes from all hit DOMs. The arrival times of the photons, however, can be included in the energy reconstruction. By that, unrelated noise pulses are not attributed to the cascade of the track segment if the timing does not fit the cascade hypothesis. Instead of the total number of photo electrons N_o per DOM the individual photons n_{oi} per DOM and time bin i are used.

After solving the linear equation system and obtaining the energy loss per segment, the vertex and direction of the track can be fitted by maximizing the Millipede likelihood

$$L = \prod_{\substack{o \in \text{hit} \\ \text{DOMs}}} \prod_{\substack{i \in \text{time} \\ \text{bins}}} \frac{1}{\Gamma(n_{oi}+1)} \left(\sum_{k=1}^{n} B_{ki}(\vec{r}_o) E_k + \nu_{oi} \right)^{n_{oi}} \mathrm{e}^{-\sum_k B_k(\vec{r}_o) E_k + \nu_{oi}} , \tag{4.29}$$

where $\mu_{oi} = \sum_k B_k(\vec{r}_o) E_k + \nu_{oi}$ is the total number of expected photo electrons per DOM and time bin (c.f. Sec. 4.3.2) and ν_{oi} is the expected number of noise photons [Whi11]. Hence, the Millipede reconstruction can be extended to a complete seven parameter fit. In this thesis the vertex and direction are fixed and only the interaction times and energy losses are reconstructed. The photon arrival times are included by requiring a minimum of five photons per time bin as this is the minimally allowed value for the algorithm to give reliable results.

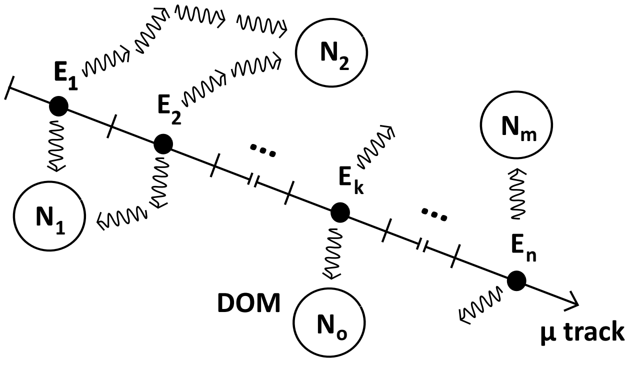

Figure 4.5: Schematic working principle of the Millipede reconstruction: A track is divided into n segments each containing a fitted cascade with energy E_k. The observed charge N_o in a nearby DOM is given by the superposition of all cascade segments each weighted with the corresponding photon distribution. This gives the linear equation system (4.28) for all DOMs.

4.4 First Event Selection

The goal of the cascade analysis is to find neutrino-induced cascades of astrophysical origin. It includes both the charged current interactions of electron neutrinos and the neutral current interactions of all neutrino types. The analysis is optimized for an E^{-2} spectrum as expected for neutrinos from cosmic accelerators (c.f. Sec. 2.2.1). Atmospheric muons and atmospheric neutrinos are considered as background. Due to the low number of expected neutrino events and to not introduce any biases, the cut optimization is performed solely on Monte Carlo simulations. The burnsample containing 10% of the total experimental data is used for a verification of the analysis (c.f. Sec. 4.2).

As described in Sec. 4.1, the number of track events for an unfiltered data sample is much larger than the number of cascade events. The trigger rate of the detector is about 2100 Hz [Seu09] which yields approximately $6 \cdot 10^{10}$ events during the detector operating time of 332 d in the season 2010/11. Only about a couple of hundred signal events are expected at trigger level using the latest limit for the total neutrino flux $\Phi = 4 \cdot 10^{-8}\ \mathrm{GeV\,s^{-1}\,sr^{-1}\,cm^{-2}}E^{-2}$ for all flavors [Mid12]. Therefore, the very first reconstructions need to be applied to a majority of track-like events and they must be fast enough to manage the vast amount of events. The purer a cascade sample becomes the more sophisticated and time-consuming reconstructions can be used. The analysis is, hence, divided into different filters which are optimized with respect to the signal-background discrimination. The main goal of the filters is to reduce the number of background events without losing too many signal events.

The baseline for all analysis channels such as muons, cascades, extremely high energy events (EHE) and others [TB11] is set by the detector triggers such as the SMT8 (c.f. Sec. 3.1.2). For the cascade analysis the event stream is then processed by the *online cascade filter* directly at the South Pole. It only uses simple and fast reconstructions to reduce the background rate. The events passing the online filter make up the first event selection defined as level 1. They are transferred via satellite to the IceCube data center in Madison, Wisconsin. There, some more time-consuming reconstructions but no further cuts are applied which is defined as the level 2 offline filter. The next cascade filter is defined as level 3 which includes more reconstructions and cuts. Both offline levels 2 and 3 are a common baseline for every cascade analysis. If applicable, there are further commonly used cut levels. For the study with IC79 presented in this thesis, however, level 3 is the last commonly used filter level. For each individual analysis based on this first event selection one defines a custom set of higher filter levels. The custom level 4 for this thesis will be discussed in Sec. 6.1.

Online Cascade Filter (Level 1): The event stream taken by the DAQ at the South Pole is processed by the online cascade filter in order to reduce the total rate. Since the neutrino rate is many orders of magnitude below the background rate the total trigger rate is basically equal to the background trigger rate. The online filter uses two simple and fast first guess reconstructions to filter obvious background events based on the shape and source speed of the light distribution in the IC79 detector [Seu09]. The first is the tensor of inertia eigenvalue ratio and the second is the LineFit velocity (c.f. Sec. 4.3.3 and 4.3.4). The distributions are shown in Fig. 4.6. The event rate decreases from 2082 Hz to 31 Hz[7] by using the cuts [Seu09]

$$q > 0.05 \qquad \text{on the tensor of inertia eigenvalue ratio,} \tag{4.30}$$

$$v < 0.11 \qquad \text{on the LineFit velocity.} \tag{4.31}$$

This corresponds to a background suppression of 98.5%. The signal passing rate is 77% for energies above 1 TeV [Seu09].

---

[7] This value is taken from the filter proposal. The passing rate of the installed online filter is 27.75 Hz [vS12a].

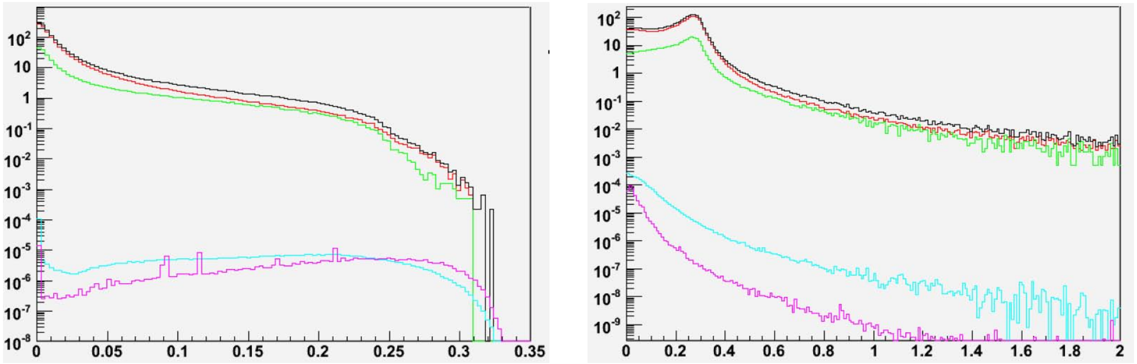

Figure 4.6: The event rate in Hz as a function of the tensor of inertia eigenvalue ratio (left) and the LineFit velocity (right) for the online cascade filter: Shown are single (red), double (green) and the combined (black) CORSIKA events as well as the atmospheric (cyan) and the astrophysical (purple) electron neutrino events. Cascade events have an eigenvalue ratio close to 0.3, whereas most track-like events have a value close to zero. The LineFit velocity peaks at a value of 0.3 corresponding to the speed of light for real muons traversing the detector. Cascades have a rather small value. The authors of the filter proposal used the IC77 dataset. The filter implementation is equal for the IC79 detector (Ref. [Seu09]).

Offline Cascade Filter (Level 2): The event stream which has passed the online filter is processed offline with the level 2 filter at the IceCube data center in the North. The level 2 filter does not apply any cuts. It only adds reconstructions which are, due to a strict limitation of resources, too expensive to process at the South Pole [vS12a]. The level 2 filter adds the likelihood based reconstructions CascadeLlh, SPEFit and ACER for a first reconstruction of the vertex, the direction and the energy, respectively (c.f. Sec. 4.3.3 and 4.3.4).

Offline Cascade Filter (Level 3): The event stream coming from the level 2 filter contains some first likelihood reconstructions which yield cut variables. The offline level 3 filter, therefore, mainly cuts on the level 2 variables and adds some more reconstructions to the remaining events. The cut variables used in the level 3 filter are a likelihood ratio from the reconstructions CascadeLlh and SPEFit (c.f. Sec. 4.3.3 and 4.3.4), an energy-dependent zenith angle cut and a fill ratio cut which is dependent on a vertex containment criterion. Furthermore, the rather expensive likelihood based reconstruction Credo is applied to obtain a full seven parameter cascade fit. The cuts are optimized using the atmospheric muons as background and the atmospheric electron neutrinos as signal, since this resulted in cut efficiency which was equal or greater for the astrophysical E^{-2} electron neutrino flux [vS12a].

The first cut is based on the ratio between the likelihood of the track and the cascade reconstruction. The cascade is reconstructed by CascadeLlh and the track by the SPEFit. The distribution is shown in Fig. 4.7 (left). It shows that the majority of events is located at positive values, i.e. that the track hypothesis is more likely. As discussed in Sec. 4.3.2, the logl value should be small, since the likelihood maximization corresponds to a minimization of the negative logarithm of the likelihood. A positive ratio means that the track hypothesis is more likely, a negative ratio comes from the cascade hypothesis. With the cut on the log-likelihood ratio, only events are kept with [vS12a]

$$\log\left(\frac{L_{\text{track}}}{L_{\text{cascade}}}\right) < 5 \qquad \text{or} \qquad E_{\text{ACER}} > 10\ \text{TeV}, \tag{4.32}$$

where E_{ACER} is the energy reconstructed by ACER. The energy cut is introduced due to the fact that atmospheric muons predominantly occur at lower energies up to 10 TeV.

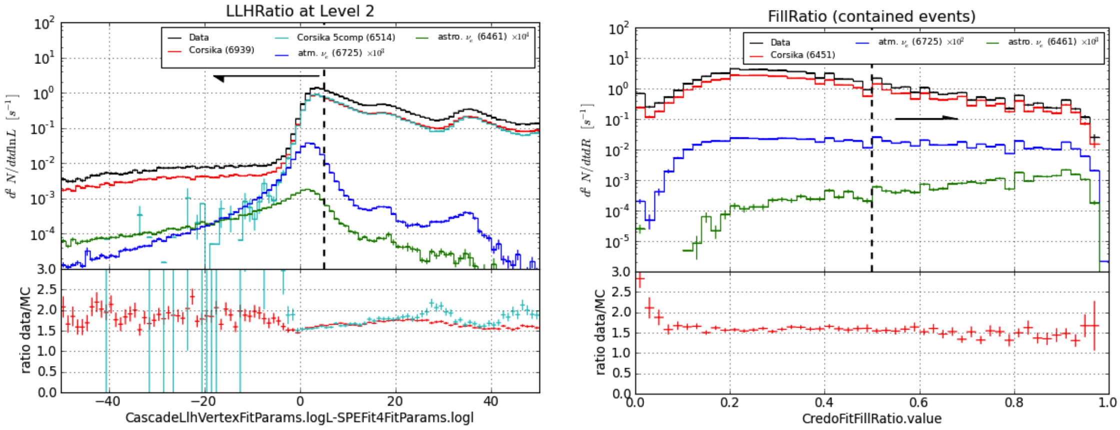

Figure 4.7: The distributions of the log-likelihood ratio (left) and the fill ratio (right) for the cascade level 3 filter: Shown are polygonato (red) and five component (cyan) CORSIKA events, atmospheric (blue) and astrophysical (green) electron neutrino events as well as experimental data (black). The ratio $\log(L_{\text{track}}/L_{\text{cascade}})$ compares the cascade and the track hypothesis to the observed light distribution where the cut is indicated to keep cascade-like events with $\log(L_{\text{track}}/L_{\text{cascade}}) < 5$. The fill ratio distribution is shown for contained events and peaks at high values for signal and at low values for background. The cut is applied as indicated with $f > 0.5$. Note that the electron neutrino fluxes are conveniently scaled by a factor of 100 and 1000 for atmospheric and astrophysical neutrinos, respectively (Ref. [vS12a]).

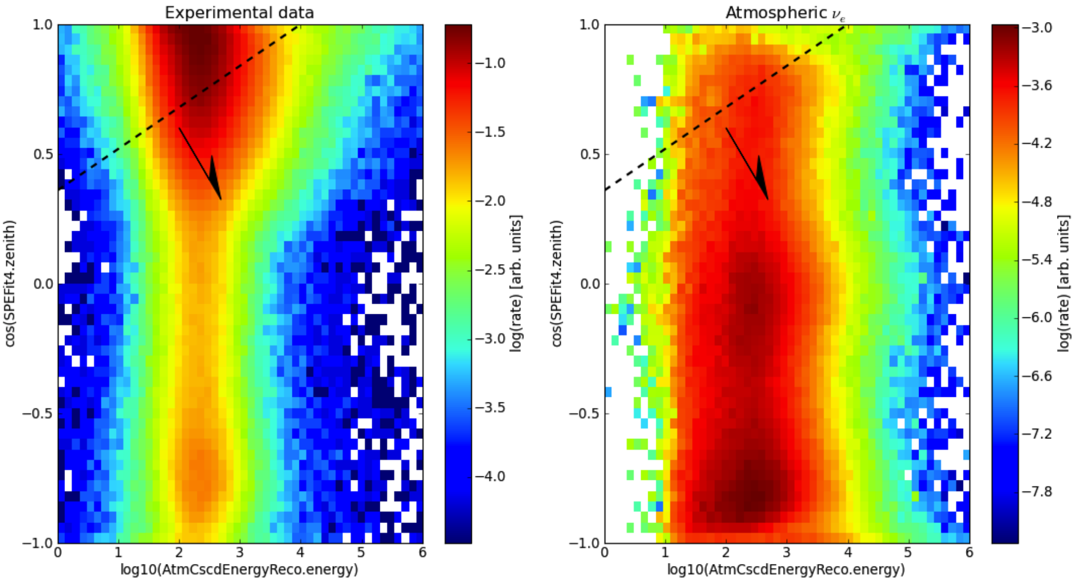

Figure 4.8: The distribution of the cascade energy and zenith angle for the cascade level 3 filter: Shown are the dependence of the zenith angle reconstructed by the SPEFit versus the energy reconstructed by ACER for experimental data (left) and atmospheric electron neutrino events (right). Since the cut was optimized using atmospheric instead of astrophysical neutrinos, this corresponds to a comparison between signal and background for the energy-dependent zenith cut. The cut on the zenith angle scales linearly with the logarithm of the energy as indicated and is parameterized by $\cos\theta_{\text{SPE}} < 0.36 + 0.16\log(E_{\text{ACER}}/\text{GeV})$. It reduces a majority of down-going tracks without discarding high-energy events (Ref. [vS12a]).

The second selection criterion is an energy-dependent cut on the zenith angle. The energy is reconstructed with ACER and the zenith angle is taken from the SPEFit. The distributions are shown in Fig. 4.8. One can see that the experimental data is dominated from down-going muons (the zenith angle is smaller than 90°). With this cut only events are kept with [vS12a]

$$\cos\theta_{\mathsf{SPE}} < 0.36 + 0.16\log(E_{\mathsf{ACER}}/\mathrm{GeV}) \qquad \text{or} \qquad E_{\mathsf{ACER}} > 10\ \mathrm{TeV}, \tag{4.33}$$

where θ_{SPE} is the zenith angle reconstructed by the SPEFit. Both the log-likelihood ratio and the zenith angle cuts are not applied for events with an energy $E_{\mathsf{ACER}} > 10$ TeV [vS12a].

The next step of the level 3 filter is to apply a full seven parameter cascade reconstruction using the Credo reconstruction with one iteration [vS12a]. The resulting vertex is then used to determine if the reference cascade is contained inside the detector. The vertex in this step is considered to be contained if the x and y coordinates are inside the polygon as shown in Fig. 3.2. The containment criterion can be tightened when demanding that the z coordinate is within $[-500\ \mathrm{m}, 500\ \mathrm{m}]$. An actual cut on the (full) containment is not applied until level 4 (see Sec. 6.1). At this stage the vertex containment is only determined.

The last cut is on the fill ratio. The calculation of the fill ratio is seeded with the vertex from the Credo reconstruction and the optimization is performed in dependence on the vertex containment. The distribution is shown in Fig. 4.7 (right) for contained events. It shows that the majority of events is track-like resulting in a small fill ratio value and that neutrino-induced cascades have greater values. With the fill ratio cut only events are kept with [vS12a]

$$f > \begin{cases} 0.5 & \alpha = 0.3 \quad \text{and} \quad \text{vertex contained,} \\ 0.35 & \alpha = 0.5 \quad \text{and} \quad \text{vertex uncontained,} \end{cases} \tag{4.34}$$

where α is the scaling constant for the radius of the sphere defined by the mean distance between the vertex and the hit DOMs (c.f. Sec. 4.3.3).

The cut efficiencies can be extracted from the filter passing rates listed in Tab. 4.1. The total event rate of 27.75 Hz from the online filter is reduced to 0.76 Hz by the level 3 filter. This corresponds to a background suppression of about 97%. The atmospheric electron neutrino rate is suppressed by roughly 40%, whereas the efficiency is almost 90% for astrophysical electron neutrinos (which are also modeled by the flux $\Phi = 4\cdot10^{-8}\ \mathrm{GeV\,s^{-1}\,sr^{-1}\,cm^{-2}}E^{-2}$). A possible containment cut as defined for level 3 could reduce the background rate by another factor of 2 while maintaining nearly 100% for contained cascade events above an energy of $E_{\mathsf{ACER}} > 10$ TeV [vS12a]. For each passing rate there is a gap between the experimental data and the predicted background. In the analysis this is described empirically with the *fudge factor* which only is a scaling but not a shape difference in the distributions as can be seen in Fig. 4.7. This discrepancy is already observed for the online filter [Seu09]. The trigger rate is approximately 1.6 times higher for experimental data than for simulated data at level 3 [vS12a].

dataset	Level 2 (online)	Level 3 (total)	Level 3 (contained)
Burnsample	27.75 Hz	0.76 Hz	0.34 Hz
CORSIKA	16.73 Hz	0.47 Hz	0.24 Hz
atm. ν_e	245 μHz	90.8 μHz	80.9 μHz
astro. ν_e	2.7 μHz	2.4 μHz	1.3 μHz

Table 4.1: Passing rates for the cascade level 3 filter: The event rate of level 2 filter is equal to the online filter, since there are no further cuts applied (Ref. [vS12a]).

The event stream which passed the cascade level 3 filter is used for the study presented in this thesis. The data samples used and the implementation of the new reconstruction tool will be discussed in the next chapter.

5. The Igelfit as a new Hybrid Reconstruction Tool

The goal of this study is to implement a new reconstruction tool which supports the search for neutrino-induced cascades. The first step is to classify background events by how cascade-like their light distribution looks in the detector. This can be achieved with the Millipede algorithm which reconstructs the energy losses along a given track. The classification is described by a new quantity called *cascade factor* which relates the maximum to the total deposited energy. In the second step the cascade and track reconstructions are combined to build a new hybrid tool called *Igelfit*. The idea is to reconstruct the cascade vertex as precisely as possible and to take it as a fixed anchor point for a set of tracks with different directions. For each track the corresponding energy loss hypotheses are reconstructed with Millipede. The fit result of this hybrid reconstruction is the track which maximizes the Millipede likelihood. The Igelfit is essentially a combined full seven parameter fit and delivers the cascade factor, the zenith angle, the energy and a likelihood ratio as potential cut parameters.

In the first section the data samples used for this study are introduced. In the second section the classification of background events via the cascade factor is described and the true and reconstructed energy losses are compared. The implementation of the Igelfit and the emerging cut parameters are described in the third section. Finally, the vertex, directional and energy resolutions of the Igelfit are discussed in the last section. The applications of the Igelfit along with the definition of the customized cascade level 4 are discussed in Chapter 6.

5.1 Data Samples

The study presented in this thesis uses data samples which are optimized for an astrophysical neutrino flux with an E^{-2} spectrum. Two different ice models are used in a complementary way for different reconstruction algorithms, since there are already studies on how each reconstruction behaves with the corresponding ice model [Mid12, vS12b]. There are no significant conflicts observed for different ice models. Millipede and Monopod reconstructions are applied with the SPICE1 ice model using spline tables and all other reconstructions, in particular the Credo reconstruction, are applied with the AHA ice model using photorec tables (c.f. Sec. 3.2). The study is based on simulations and experimental data from 2010 and 2011 with the IC79 detector geometry (c.f. Sec. 3.1). It is implemented with IceRec 04-01-00 and Python 2.7.2.

The muon simulation files are generated by CORSIKA using the polygonato model with an unweighted Hörandel spectrum. The SPICEMie ice model is used for the simulated photon propagation. The zenith angle range of the primary particles is $0^\circ < \theta_{\text{prim}} < 90^\circ$ and the energy range is $600\text{ GeV} < E_{\text{prim}} < 100\text{ EeV}$. Two datasets with the same settings and in total 200 000 generated files are used. This corresponds to an effective livetime of 21.8 d.

The neutrino simulation files for all flavors are generated by NUGEN using a weighted E^{-2} spectrum and the SPICEMie ice model. The range of the zenith angle is $0° < \theta_\nu < 180°$ for all neutrino flavors. The energy range for the electron and tau neutrinos is $1\ \text{TeV} < E_\nu < 1\ \text{EeV}$ and for the muon neutrinos $10\ \text{GeV} < E_\nu < 1\ \text{EeV}$. The lower energy limit for muon neutrinos compared to the other flavors is chosen to account for the background of atmospheric muons below 1 TeV. Each dataset contains in the order of 10 000 generated files resulting in an effective livetime of much more than one year.

The experimental data was taken in the season 2010/11. Every tenth run is selected for the burnsample starting from 115990 to 118170. In total, the burnsample consists of 119 runs each lasting about 8 h in the median.[1] This gives a detector livetime of 33.5 d for the burnsample. An overview of the data samples used in this study is given in Tab. 5.1.

Generator	**Type**	**Spectrum**	**Datasets/Runs**	**No. Gen. Files**	**No. Events**	**(Eff.) Livetime**
CORSIKA	μ	unw. poly.	6939, 6451	200 000	887 530	21.8 d
NUGEN	ν_e	E^{-2}	6725	10 000	1 384 943	> 365 d
NUGEN	ν_μ	E^{-2}	6726, 6467	24 480	631 684	> 365 d
NUGEN	ν_τ	E^{-2}	6593	9 688	505 315	> 365 d
Burnsample	-	-	115990 - 118170	-	2 176 556	33.5 d

Table 5.1: Data samples used for the study presented in this thesis.

5.2 Event Classification

The reconstruction algorithms and cut parameters described in Sec. 4.3.3 and 4.3.4 are used to distinguish background and signal events by utilizing the shape and time of the light distribution in the detector. The Millipede reconstruction has already been introduced as a reconstruction algorithm which divides a track into segments and tries to fit a single cascade in each segment by maximizing the likelihood. The idea is to reconstruct the stochastic energy losses of a muon along its track. Whether an event looks track-like or cascade-like can then be determined by the distribution of the reconstructed energy losses.

The different event classes are sketched in Fig. 5.1. A track-like muon can be identified by its more or less evenly distributed energy losses over the major part of the track. All secondary cascades deposit roughly the same amount of energy in the detector. These events, although track-like, still pass the online cascade filter and are the major background on level 2. If a muon deposits the major part of its total energy loss by a single catastrophic interaction and much less along the remaining part of the track, the event will look rather cascade-like than track-like. These are the remaining background events passing the level 3 filter. A signal cascade induced by an electron neutrino causes just one single energy deposition on a (hypothetical) track along the incident neutrino direction. Depending on the deposited energy and the size of the track segments the energy loss spreads over one or more adjacent segments.[2] The major challenge of the cascade analysis is to identify those background events which look very alike.

In the first part of this section the energy loss distributions are discussed with respect to the different event classes. The true energy depositions are compared to the reconstructed. In the second part the cascade factor is introduced to quantify this classification. The distributions of the cascade factor are shown for different cut levels.

---

[1] Some runs are shorter due to problems with the calibration or the DAQ. The shortest run only lasted 10 min.

[2] As discussed in Sec. 2.3.2 the size of the cascade scales logarithmically with the neutrino energy.

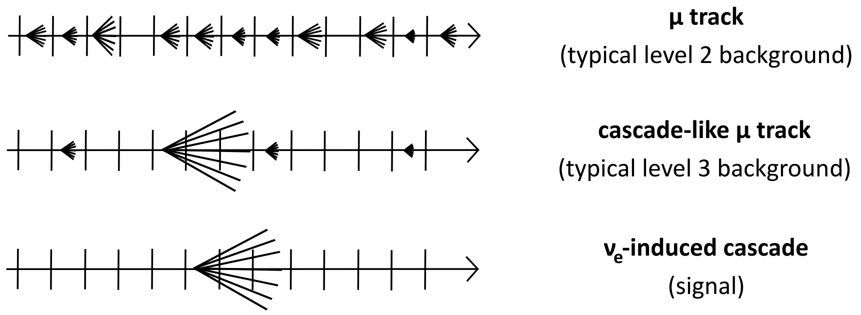

Figure 5.1: Schematic view of the event classification using the stochastic energy loss distribution for track-like muons at level 2, cascade-like muons at level 3 and neutrino-induced cascades.

5.2.1 Energy Loss Distributions

The first step of the study is to have a look at the energy loss distributions for different event types and to compare the true energy depositions with the Millipede reconstruction. Since a description of the true energy losses along a segmented track was not available, an algorithm is implemented specifically for this purpose. It is written as *I3Module* to be used as part of a module chain in IceRec in a way that the result is comparable to the Millipede reconstruction. The module called *MCMillipede* divides the true muon track into segments and sums the simulated energy losses taken from the Monte Carlo tree for each segment. Since many muon events are actually not single muons but extended muon bundles, energy losses from other tracks are projected orthogonally onto the track with the most energetic cascade. See App. A for a thorough description of the implementation.

The track is given by the production vertex and direction of the muon and its length is defined by the intersections with a cube located at the IceCube coordinate center. The cube is described by a boundary parameter a, i.e. the reconstruction space is restricted to $-a \leq x, y, z \leq a$. It is chosen to be 600 m, since the detector has a dimension of about 500 m in each direction and light produced outside the detector can propagate up to 100 m from its source into the detector. The size of the track segments is chosen to be $\Delta l = 10$ m because it is in the order of the possible vertex resolution. The length of a track is different for each event, depending on the direction. The maximum track length is $l_{\text{max}} = 1732$ m (from one corner of the cube to the opposite) and the maximum corresponding number of track segments is $n = 174$.

The MCMillipede module calculates the true energy losses and the Millipede algorithm reconstructs them. The true vertex and direction are provided as seed for the Millipede reconstruction. Only the energy losses but not the vertex and direction are reconstructed. The Millipede algorithm is configured to account for the arrival times of the photons by requiring a minimum of five photons per time bin (c.f. Sec. 4.3.4). Consequently, a track with zenith angle $\theta \in (0°, 90°)$ and azimuth angle $\varphi \in (0°, 360°)$ and the inverted track with $\theta' = \theta + 90°$ and $\varphi' = \varphi + 180°$ have the same absolute direction, but differ as down-going and up-going, respectively. This degeneracy is broken by including the photon arrival times in the reconstruction which is important for the generation of the direction seeds for the Igelfit (see Sec. 5.3.1).

In Fig. 5.2 - 5.4 the true and reconstructed energy losses are shown for exemplary background and signal events at different cut levels (c.f. Sec. 4.4). The greater the width of the distribution the more track-like the events are. If one or more adjacent track segments contain the bigger part of the total energy depositions, the event looks cascade-like. If *only* one or more adjacent track segments contain the total deposited energy, it is either a signal event or a background event which cannot be distinguished using the energy loss distribution.

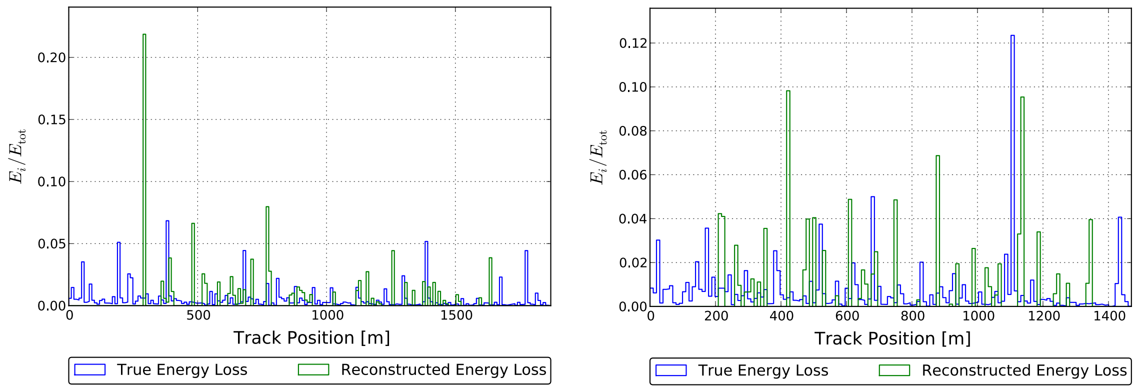

Figure 5.2: Energy loss distribution for two background events at level 2: The energy deposition is evenly distributed along the track. The muons have an energy of 5.3 TeV (left) and 11.9 TeV (right). The events are taken from the CORSIKA dataset 6451.

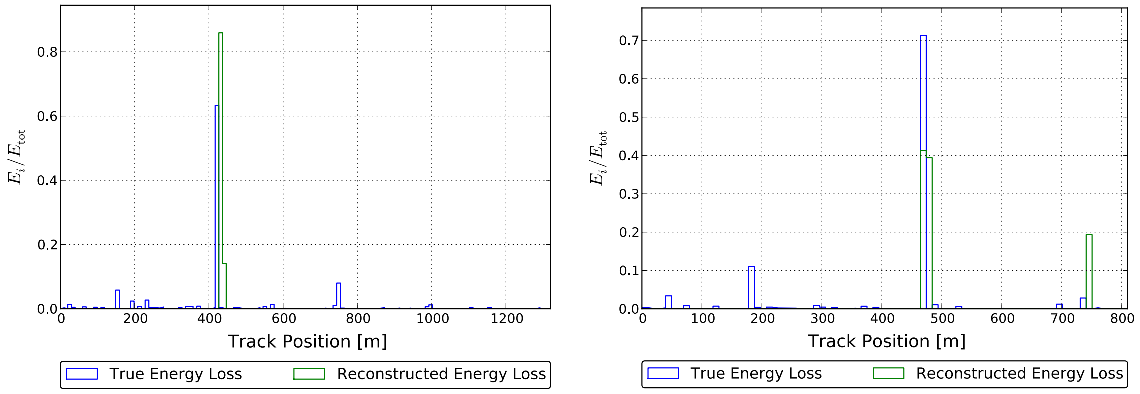

Figure 5.3: Energy loss distribution for two background events at level 3: A catastrophic energy loss makes up most of the total energy deposition. The muons have an energy of 1.3 TeV (left) and 5.9 TeV (right). The events are taken from the CORSIKA dataset 6939.

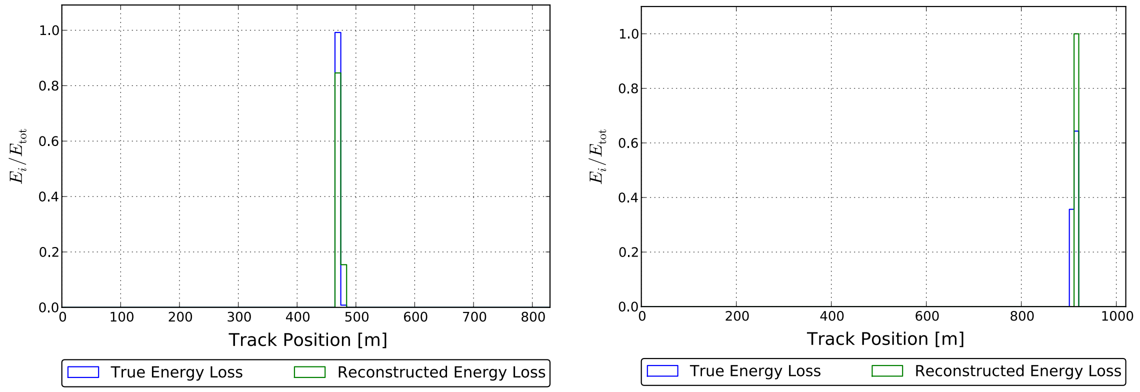

Figure 5.4: Energy loss distribution for two signal events at level 3: The energy deposition only contains the primary cascade from the neutrino interaction. The electron neutrinos have an energy of 121.6 TeV (left) and 2.2 TeV. The events are taken from the NUGEN dataset 6725.

Another observation is that the Millipede reconstruction works well for large energy depositions. It reconstructs the deposited energy at the correct vertex within the accuracy of the track segmentation of 10 m. This can particularly be seen in Fig. 5.4. For small and more frequent energy losses as shown in Fig. 5.2 the reconstruction is limited by the number of produced Cherenkov photons which might be scattered or absorbed before reaching a DOM. The pattern in the reconstructed energy loss distribution, however, agrees with the true distribution.

As a measure of how well the Millipede reconstruction is able to reconstruct the energy losses one can have a look at the total energy deposition $E_{\text{tot}} = \sum_{i=1}^{n} E_i$ summed over all n bins. In Fig. 5.5 the true and reconstructed energy depositions are compared at different cut levels. The difference of the logarithm of the energy describes the energy resolution. The distributions are normalized for convenience, since the rate at level 3 is much smaller than at level 2. The resolution improves with the cut level for atmospheric muons. This underlines the argument previously stated that the Millipede reconstruction works best for only few and large energy depositions as they are reconstructed for cascade-like events. For neutrino-induced cascades there are only subtle differences between the cut levels. The energy reconstruction is slightly asymmetric for both muons and neutrinos. The Millipede algorithm tends to reconstruct less energy than is actually deposited.

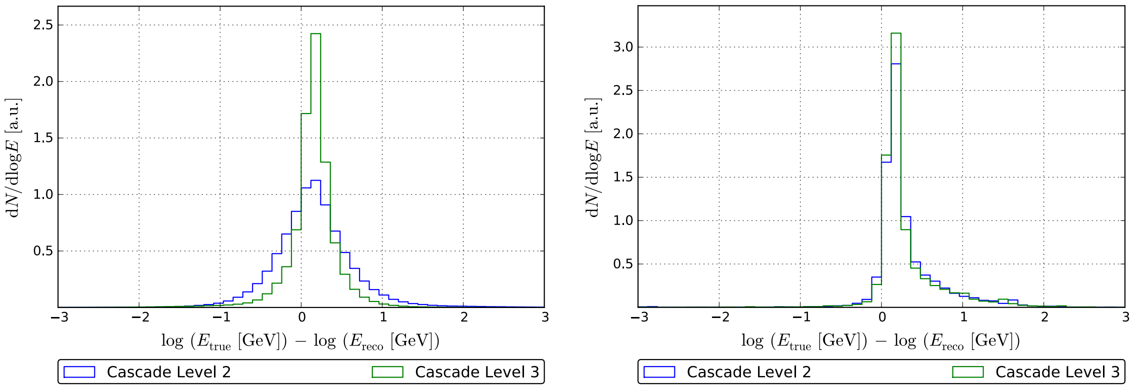

Figure 5.5: Resolution of the total energy deposition for atmospheric muons (left) and astrophysical electron neutrinos (right) at different cut levels.

Further systematic errors can be explained by the calculation of the true energy loss, namely:

- Due to the projection of secondary cascades in muon bundles onto a single track, the true energy deposition at each point along the track is slightly overestimated.
- The cascades are reconstructed as point-like but since the simulated cascades are extended they allow secondary particles to cross the border between two track segments.
- The boundary cube is 100 m larger than the actual detector, i.e. reconstructed energy losses outside the detector will be less precise compared to the true energy depositions.

The next step of the study is to quantify the different event classes by using the energy loss distributions and relating the maximum energy loss with the total deposited energy.

5.2.2 The Cascade Factor

The quantification of the energy loss distributions yields a criterion to distinguish background and signal events. How cascade-like an event looks is determined by the maximum energy loss in a single track segment in relation to the total deposited energy. This is quantified by the cascade factor

$$k = \frac{E_{\mathrm{max}-1} + E_{\mathrm{max}} + E_{\mathrm{max}+1}}{\sum_{i=1}^{n}(E_i + 2\ \mathrm{GeV})}, \tag{5.1}$$

where E_{max} is the maximum energy loss and E_i the energy loss per bin i. The enumerator does not only contain the bin with the maximum energy loss but also takes the adjacent bins into account. The size of a neutrino-induced cascade is in fact point-like compared to the dimensions of the detector but not with respect to the vertex resolution. As described in Sec. 4.1, a highly energetic cascade can have an extension which is greater than 10 m. The adjacent bins are thus added to not risk losing high-energy signal events by a possible cut on the cascade factor. The denominator is the total deposited energy plus a correction of 2 GeV per bin as the continuous ionization loss of a muon. It is approximately $\mathrm{d}E/\mathrm{d}X \simeq 0.2$ GeV/m or 2 GeV per 10 m bin (c.f. Sec. 2.3.2). The correction is added since the Millipede algorithm only reconstructs stochastic energy losses and the contribution from the ionization losses are mostly too small to produce the minimum required number of photons per time bin. The same correction is applied to signal events and thus $k_{\mathrm{true}} \lesssim 1$ for neutrino-induced cascades.

In Fig. 5.6 the cascade factor k_{true} from the true energy loss distribution is shown for background and signal. For atmospheric muons at level 2 it peaks at small values of $k_{\mathrm{true}} \simeq 0.2$ which corresponds to the observation that most events are track-like. By applying different cuts as described in Sec. 4.4, the majority of events at level 3 is cascade-like with a peak at $k_{\mathrm{true}} \simeq 0.8$. The distribution also contains a small peak from remaining track-like events at $k_{\mathrm{true}} \simeq 0.1$. As expected, the distribution for astrophysical electron neutrinos peaks at a value of $k_{\mathrm{true}} \simeq 1$. The shape does not change at different cut levels, since neutrino-induced cascade events always look cascade-like. The widening of the distribution to smaller values is caused by the ionization correction. This is acceptable because the widening which comes naturally from the Millipede reconstruction is larger as shown for the reconstructed cascade factor k_{reco} in Fig. 5.7.

In Fig. 5.8 the resolution of the cascade factor is shown for background and signal. From the distribution for atmospheric muons it can be concluded that the resolution slightly decreases with the cut level. The resolution distribution for astrophysical electron neutrinos is asymmetric, since the widening of the distribution of the reconstructed cascade factor is greater than for the true cascade factor which is $k_{\mathrm{true}} \simeq 1$ as per construction. Hence, the reconstructed cascade factor yields about the same resolution for astrophysical electron neutrinos as for atmospheric muons. Still, it is systematically underestimated which is the biggest challenge when trying to utilize the cascade factor as a cut parameter. This will be discussed in more detail in Sec. 5.4. It can be concluded that the shapes for both cut levels as well as for both background and signal agree with the true distributions.

So far, the cascade factor has only been discussed using the true information from simulation. In the next section the implementation of the Igelfit as a new hybrid reconstruction will be described. It will be explained that the cascade factor emerges from the reconstruction. Instead of the true cascade factor k_{true}, the reconstructed cascade factor k_{reco} from the truth-seeded Millipede reconstruction will be used for comparison because it includes the same systematics as a fit result employing the Millipede reconstruction.

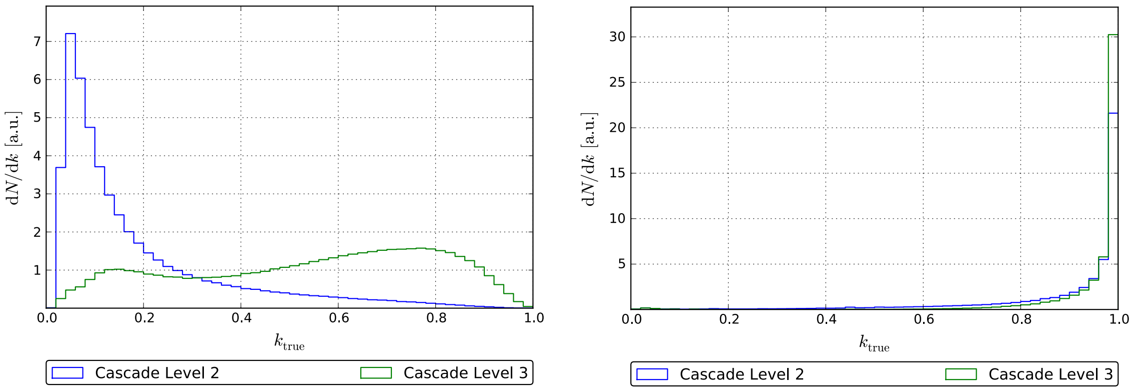

Figure 5.6: True cascade factor for atmospheric muons (left) and astrophysical electron neutrinos (right) at different cut levels.

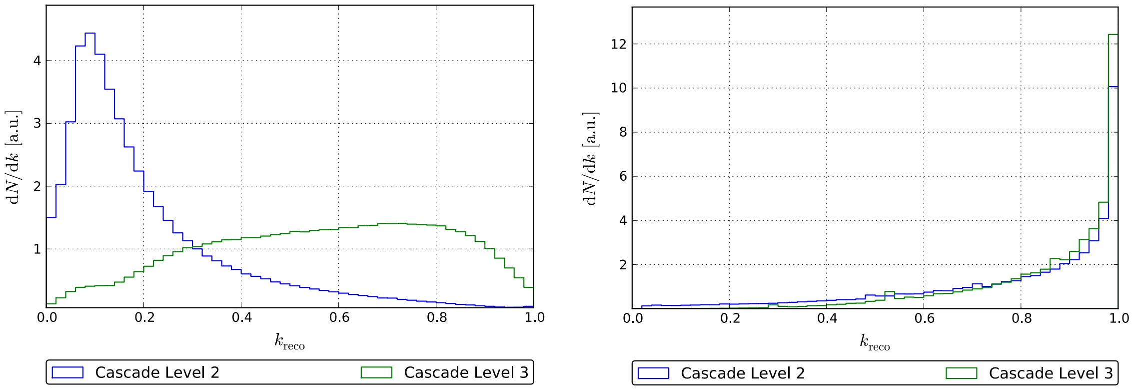

Figure 5.7: Reconstructed cascade factor from the true seed for atmospheric muons (left) and astrophysical electron neutrinos (right) at different cut levels.

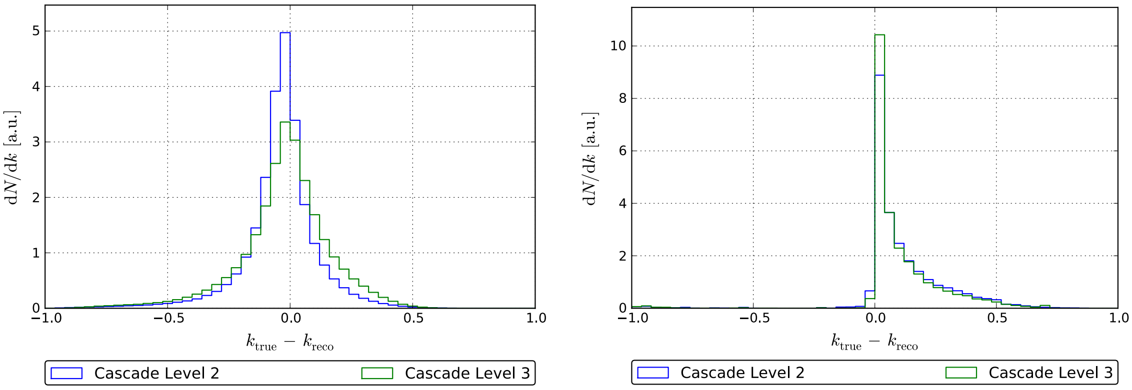

Figure 5.8: Resolution of the cascade factor for atmospheric muons (left) and astrophysical electron neutrinos (right) at different cut levels.

5.3 Implementation of the Igelfit

The idea of the Igelfit is to combine existing maximum likelihood reconstructions for tracks and cascades to build a new hybrid analysis tool. The Credo algorithm is used for the cascade vertex reconstruction which is fixed as anchor point for a multitude of isotropically distributed track directions (see Fig. 5.9). The Millipede reconstruction is seeded with each track direction and the fit result is the track that maximizes the likelihood. The idea is to use the Millipede algorithm to search for small energy depositions that are causally connected to the reconstructed cascade but located further away. If this is the case, the track hypothesis describes the event much better than the cascade hypothesis. Consequently, the Igelfit has the potential to separate cascade-like muons from neutrino-induced cascades even at high cut levels.

The implementation of the Igelfit and the emerging cut parameters will be discussed in the following sections. It will be concluded that this reconstruction is powerful for several reasons:

- The reconstruction of the cascade direction yields the zenith angle $\cos\theta_{\text{igel}}$ as a potential cut parameter. The directional resolution is dependent on the number of track directions.
- The Millipede algorithm reconstructs the energy losses along the track which yields the total energy deposition E_{igel} and the cascade factor k_{igel} as potential cut parameters.
- Since the Monopod reconstruction uses the general Millipede likelihood and because it can be used as vertex seed, the Igelfit result allows for a direct comparison between the cascade and track hypothesis via the likelihood ratio $\text{logl}_{\text{millipede}} - \text{logl}_{\text{monopod}}$.
- The Igelfit works well for both atmospheric muons and neutrino-induced cascades.

There are also some disadvantages which are mostly due to technical limitations. The Millipede reconstruction is computationally very expensive in both memory and processing time. Since each track contains many cascade reconstructions (depending on the track length and bin size), the fit diverges more often than other reconstruction algorithms. Both problems are particularly relevant for the Igelfit which consists of multiple applications of the Millipede reconstruction. The consequences for the cascade analysis are not fatal, since the Igelfit should be used at higher cut levels at which the processing time and the number of failed fits decreases significantly.

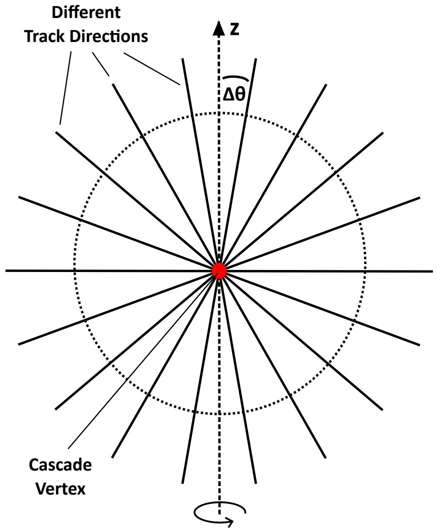

Figure 5.9: Schematic view of the Igelfit: The cascade vertex is a fixed anchor point for a multitude of different track directions. The fit result is the track hypothesis that maximizes the Millipede likelihood. The resolution $\Delta\theta$ increases with the number of tracks.

5.3.1 Vertex and Direction Seeds

The Igelfit is a hybrid tool and thus consists of two parts. The reconstruction is seeded by a vertex and a set of different track directions which will be discussed in the following.

The vertex seed for the Igelfit can be the vertex of any cascade reconstruction. Since the Credo and Monopod algorithms are the most sophisticated cascade reconstructions they are most suitable. An improved resolution is achieved by shifting the given vertex multiple times running with the full set of track directions each time. The most simple case is to shift the vertex in each direction of the coordinate axes centered around the vertex (see Fig. 5.10):

$$\vec{v}_{1,2} = \begin{pmatrix} v_x \pm \Delta r \\ v_y \\ v_z \end{pmatrix} \quad \text{and} \quad \vec{v}_{3,4} = \begin{pmatrix} v_x \\ v_y \pm \Delta r \\ v_z \end{pmatrix} \quad \text{and} \quad \vec{v}_{5,6} = \begin{pmatrix} v_x \\ v_y \\ v_z \pm \Delta r \end{pmatrix}, \tag{5.2}$$

where $\vec{v} = (v_x, v_y, v_z)$ is the original vertex seed and Δr is the shift distance. Including the original cascade vertex the total number of vertex seeds is seven. The Credo reconstruction with eight iterations is used as vertex seed for this study. The results at level 3 are obtained without and at level 4 including a vertex shift of $\Delta r = 10$ m (see Sec. 6.1). The value of the shift is chosen corresponding to the approximate size of the vertex resolution.

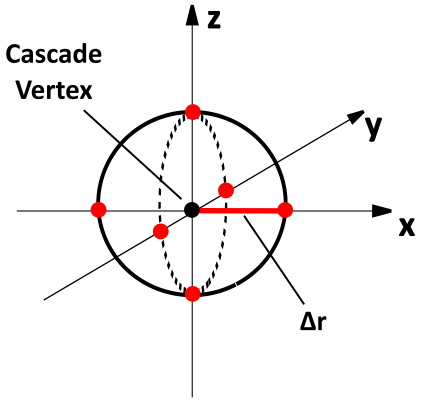

Figure 5.10: Schematic view of the shifted vertex seed: The vertex from a cascade reconstruction is shifted by a distance of Δr in six different directions along the standard axes.

The direction seeds are generated by isotropically distributing a predefined number of points on a sphere. The method used is taken from Ref. [Bou96] and works in three steps:

1. Randomly distribute the required number of points on the unit sphere.
2. Find the two closest points on the sphere and move them slightly apart by a factor r.
3. Repeat the second step with n iterations.

This method is chosen because it is very simple and straightforward. Although it is very inefficient, it is still suited for this purpose because the direction seeds are generated once, saved and then simply read in for all reconstructions. Three different sets of direction seeds are generated with 128, 256 and 512 different track directions using $r = 1\%$ and $n = 1\,000, 10\,000, 100\,000$ iterations, respectively. The results are shown in Fig. 5.11. The main idea behind this method is to set a fixed number of points per surface area $\mathrm{d}A = \mathrm{d}\varphi \mathrm{d}\cos\theta$ which scales with the cosine of the zenith angle. Therefore, the number of different track directions at the horizon is greater than at the poles as can be seen in Fig. 5.11. For this study the Igelfit is used with 128 track directions at level 3 and 512 at level 4 (see Sec. 6.1).

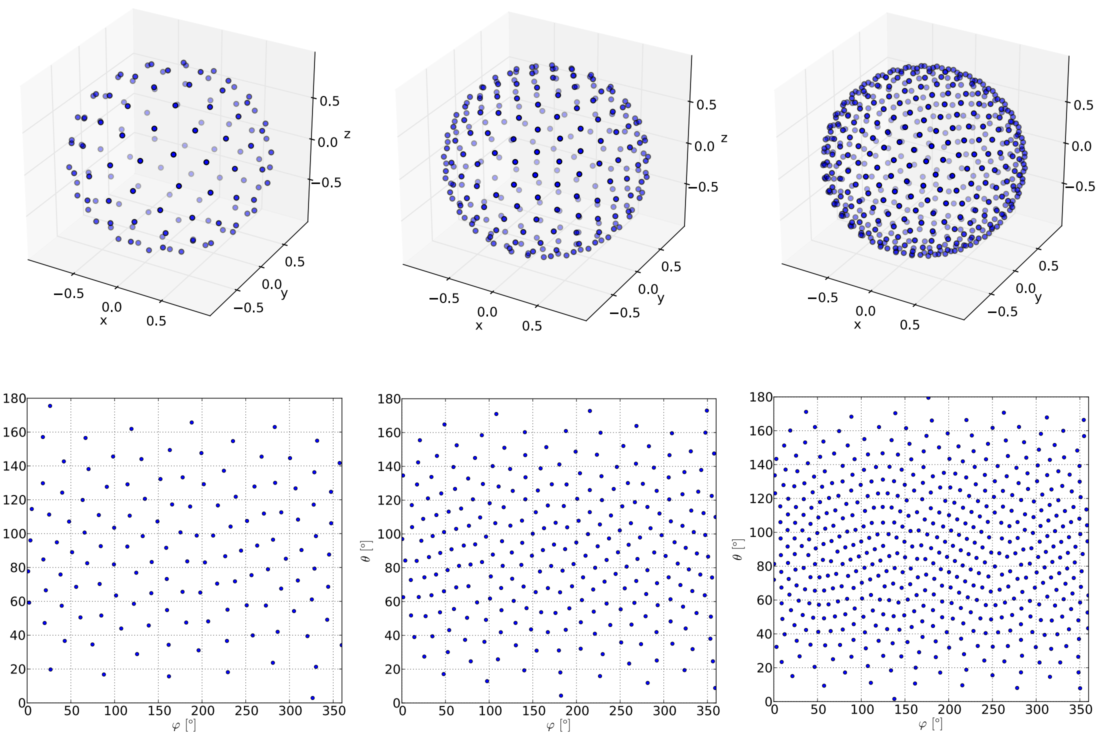

Figure 5.11: Different sets of direction seeds: The Igelfit can be used with 128 (left), 256 (middle) or 512 (right) track directions. Shown are the corresponding points on the unit sphere in cartesian coordinates (above) and the projections of the zenith and azimuth angles (below).

5.3.2 Cut Parameters of the Igelfit

The Igelfit yields at least four potential cut parameters. In this study the cascade factor k_{igel}, the zenith angle $\cos\theta_{\mathrm{igel}}$, the total energy deposition E_{igel} and the likelihood ratio $\mathrm{logl}_{\mathrm{millipede}} - \mathrm{logl}_{\mathrm{monopod}}$ of the track and cascade reconstructions by Millipede and Monopod, respectively, are studied. The Monopod reconstruction is performed separately but can be incorporated as vertex seed for the Igelfit in future analyses.

The distributions of the potential cut parameters are shown in Fig. 5.12 and 5.13 for atmospheric muons and for electron, muon and tau neutrinos modeled with an astrophysical E^{-2} flux as well as for experimental data. The distributions are normalized to conveniently compare the shapes for all datasets. Since the event rate of atmospheric muons is much greater than for neutrinos, the experimental data follows the muon distribution. The potential of these parameters in separating signal and background is discussed in Sec. 6.1 by using atmospheric muons as background and astrophysical electron neutrinos as signal. Possible distinctions between different neutrino flavors will be discussed in Sec. 6.2.1.

The cascade factor in Eq. (5.1) is obtained from the reconstructed energy losses using the Millipede algorithm. The distributions of the cascade factor are plotted in Fig. 5.12 (left). The different shapes for atmospheric muons and neutrino-induced cascades can be reconstructed fairly well. As expected, the distribution for atmospheric muons is rather flat and peaks around $k_{\mathrm{igel}} \simeq 0.7$. It stands out that the last bin ($k = 1$) of the distribution is populated more often. These are misreconstructed events which will be discussed in Sec. 5.4.2. As expected, the distribution of the cascade factor for neutrino-induced cascades peak at $k_{\mathrm{igel}} \simeq 1.0$. The long tail towards small values is due to the reconstruction effects of the Millipede algorithm (c.f. 5.2.2). The shapes of the distributions for experimental and simulation data agree.

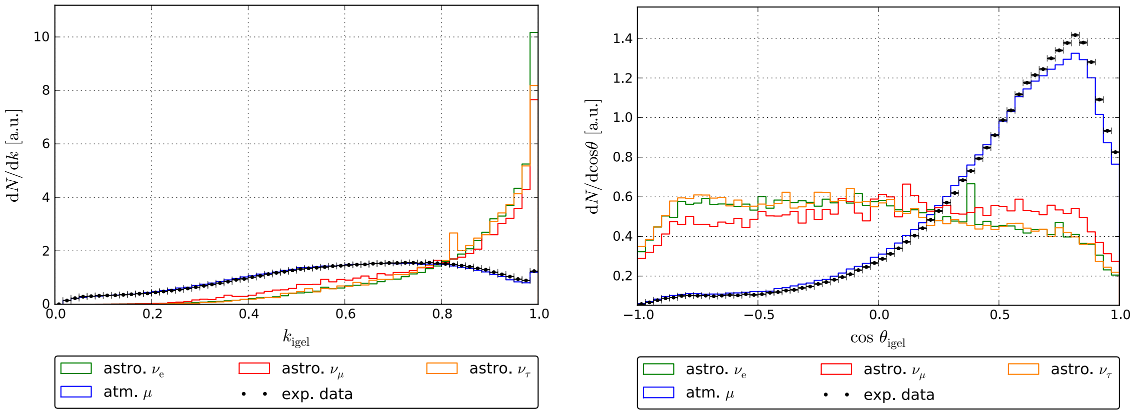

Figure 5.12: The cascade factor (left) and the zenith angle (right) of the Igelfit for atmospheric muons, for electron, muon and tau neutrinos and for experimental data.

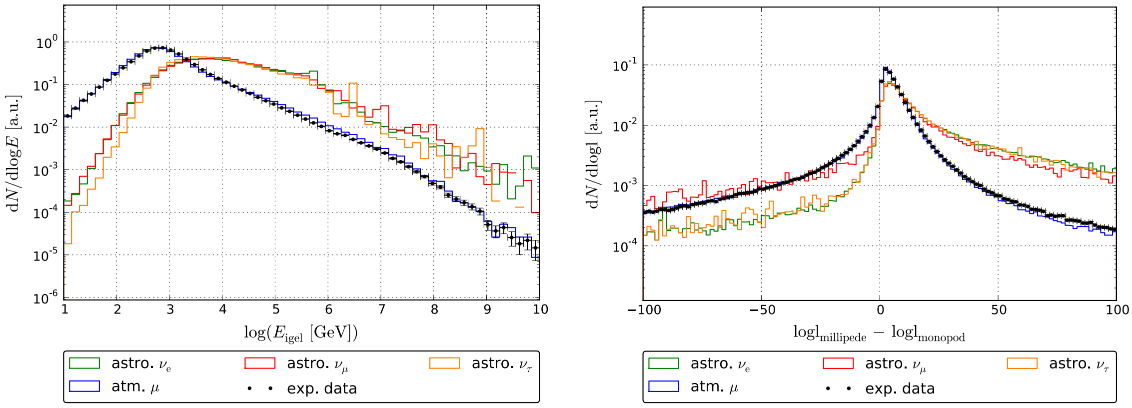

Figure 5.13: The total energy deposition (left) and the likelihood ratio (right) of the Igelfit for atmospheric muons, for electron, muon and tau neutrinos and for experimental data.

The zenith angle is given by the reconstructed track which is fitted through the cascade vertex. The distributions of the zenith angle are plotted in Fig. 5.12 (right). As expected, atmospheric muons are only down-going in the detector and thus peak at small zenith angles. The distribution decreases for $0.8 \leq \cos\theta_{\mathrm{igel}} \leq 1.0$, since the dataset used is processed to level 3 which includes a cut on the zenith angle (c.f. Sec. 4.4). Events below the horizon are misreconstructed. The distribution for neutrinos is flat and approximately equal for all flavors. This is expected for a diffuse astrophysical neutrino flux. The cosine of the zenith angle is smeared with a Gaussian distribution to reduce the binning effect due to the limited number of distinct track directions of the Igelfit. The shapes of the distributions for experimental and simulation data agree. The discrepancies at the peak of the atmospheric muon distribution are still reasonably good, since this is background which will be filtered out at higher cut levels.

The total energy deposition is the sum over all reconstructed energy losses along the track. The distributions of the total energy depositions are shown in Fig. 5.13 (left). As expected, the spectrum follows a power law. Atmospheric muons predominantly have energies at $E_{\mathrm{igel}} \leq$ 10 TeV which is also the crossing point where most neutrino events are reconstructed. An energy cut is, therefore, a very efficient way to reduce the background but inevitably removes all low energetic neutrino events. Eventually, an astrophysical or atmospheric prompt neutrino flux could be detected at the highest energies where the background rate is smaller than the signal rate. Again, the shapes of the distributions for experimental and simulation data agree.

The likelihood ratio is obtained by comparing the Millipede likelihood of the fitted track with the Monopod likelihood of an independent cascade reconstruction.[3] The logl value should be small for a good hypothesis, since it corresponds to a large value of the likelihood per definition in Eq. (4.16). The difference $\text{logl}_{\text{millipede}} - \text{logl}_{\text{monopod}}$ is equivalent to the negative likelihood ratio and should thus be negative for track-like and positive for cascade-like events. The distributions of the likelihood ratio are plotted in Fig. 5.13 (right). Although the separation is not very strong, the tendency follows the argument. It is also interesting to compare electron and muon neutrinos. The distribution of muon neutrinos is just in between the expected behavior for muons and electron neutrinos. This is due to the charged current interactions of the muon neutrino which produces a cascade and a muon. These events can be described equally well as track or cascade hypothesis, hence the shifted likelihood ratio.

The energy dependence is an important aspect of the quality check of potential cut parameters, since it might be necessary to develop an energy-dependent cut similar to the level 3 filter (c.f. Sec. 4.4). In Fig. 5.14 - 5.16 the cascade factor and the zenith angle obtained from the Igelfit are shown in dependence of the energy of the Credo reconstruction for experimental data, atmospheric muons and astrophysical electron neutrinos. The cascade factor is energy dependent for all datasets. Large values of k_{igel} tend to occur at higher energies for atmospheric muons. This observation is reasonable, since the probability and size of a catastrophic energy loss increase with the muon energy. The zenith angle is particularly energy dependent for atmospheric muons. The distribution peaks at the zenith as all atmospheric muons are down-going in the detector. Events with $\cos\theta_{\text{igel}} < 0$ are misreconstructed events. Muons which deposit much energy in the detector predominantly come from the zenith, since the propagation length through the ice is the shortest, and hence, the energy losses outside the detector are small. As expected, the zenith angle distribution for a diffuse astrophysical neutrino flux is not dependent on the energy. The distributions of the experimental and the simulation data agree except for the total event rate which is slightly higher (c.f. Sec. 4.4 and 6.1).

---

[3] It is proposed to use the reconstructed cascade by Monopod as vertex seed In the future use of the Igelfit. The obtained likelihood ratio will then only be derived from reconstructions which are part of the Igelfit.

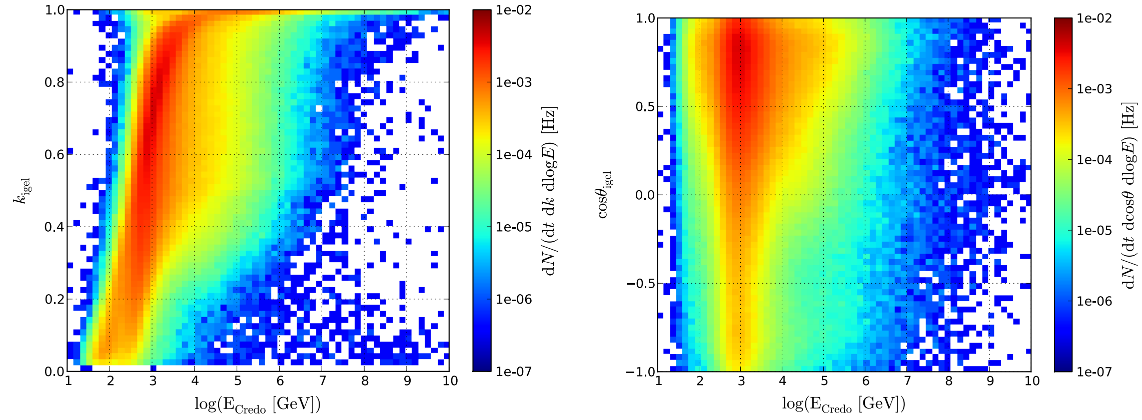

Figure 5.14: Energy dependence of the cascade factor (left) and the zenith angle (right) from the Igelfit for experimental data.

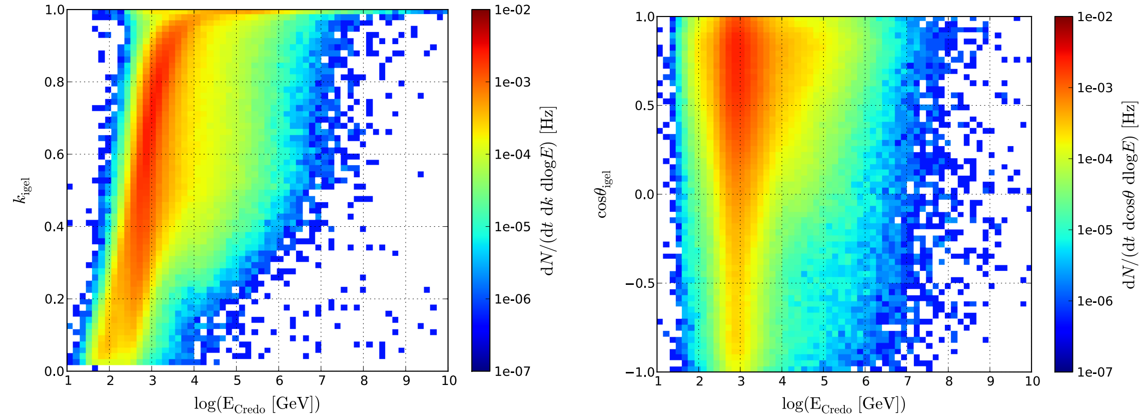

Figure 5.15: Energy dependence of the cascade factor (left) and the zenith angle (right) from the Igelfit for atmospheric muon simulations.

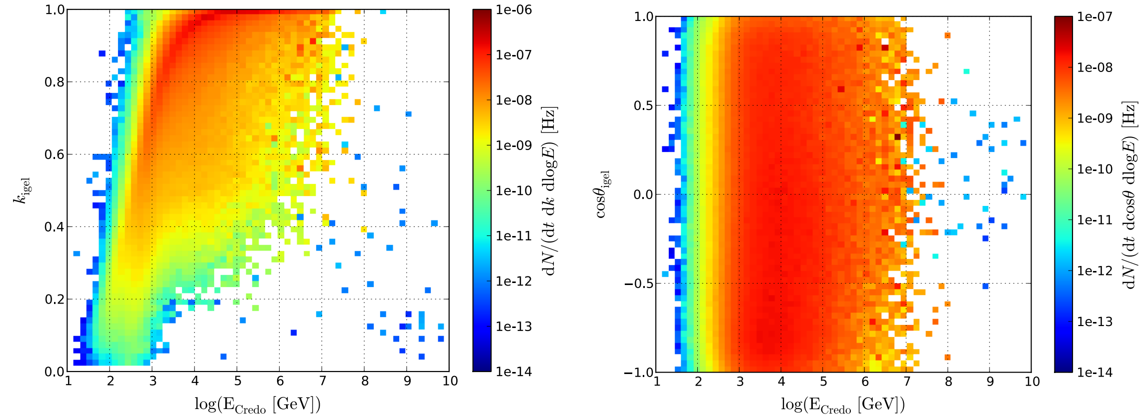

Figure 5.16: Energy dependence of the cascade factor (left) and the zenith angle (right) from the Igelfit for astrophysical electron neutrino simulations.

5.4 Resolution of the Igelfit

In this section resolution of the Igelfit reconstruction is discussed. In the first part the resolutions of the energy and the cascade factor are determined. The vertex resolution is discussed in the second section. Finally, the directional resolution is compared to existing reconstructions.

5.4.1 Energy Resolution

The sum over all reconstructed energy losses yields a total energy deposition. For neutrino-induced cascades this is equal to the reconstructed cascade energy. The resolutions of the cascade factor and the total deposited energy are plotted in Fig. 5.17 and the values listed in Tab. 5.2. The resolution is determined by using a Gaussian fit to the difference of the result obtained from the Igelfit and the Millipede reconstruction using the true vertex and direction seed (c.f. Sec. 5.2.1). This implies that the resolution is only given as quality criterion for the Igelfit reconstruction. It does not include systematic effects with respect to a potentially false estimation of the true deposited energy (e.g. due to the ice model or DOM calibration).

The energy resolution is plotted in Fig. 5.17 (left) for all datasets at level 3. It is best for pure cascades induced by electron and tau neutrinos, slightly worse for muon neutrino events and worst for atmospheric muons. The energy resolution is $\Delta \log E\,[\mathrm{GeV}] \simeq 0.1$ on average for all datasets. It increases at level 4 which supports the argument that the reconstruction works best for events of purer cascade samples. The resolution of the cascade factor is depicted in Fig. 5.17 (right). It is about $\Delta k \simeq 0.07$ on average for all neutrino datasets. The resolution is $\Delta k = 0.19$ for atmospheric muons at level 3 and thus much worse compared to cascade events. However, at level 4 the resolution for atmospheric muons becomes equally good as for neutrino events. Hence, it can be concluded that the more cascade-like the event looks, the better the reconstruction of the cascade factor and the total deposited energy is.

		atm. μ	**astro. ν_e**	**astro. ν_μ**	**astro. ν_τ**
Level 3	Δk	0.19	0.06	0.08	0.06
	$\Delta \log E$ [GeV]	0.12	0.09	0.10	0.09
Level 4	Δk	0.07	0.06	0.06	0.06
	$\Delta \log E$ [GeV]	0.07	0.07	0.08	0.07

Table 5.2: Resolution of the Igelfit energy and cascade factor quoted as the standard deviation from a Gaussian fit.

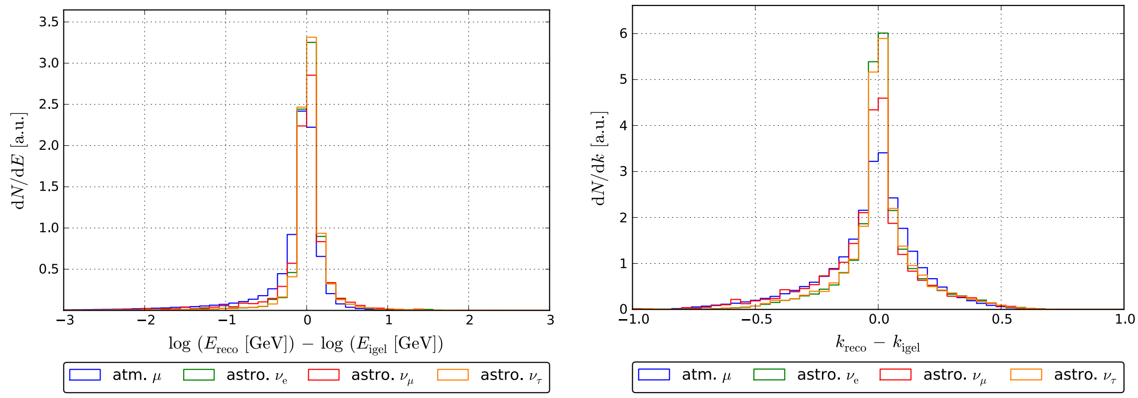

Figure 5.17: Resolution of the Igelfit energy and cascade factor at level 3.

5.4.2 Vertex Resolution

The vertex resolution is defined as the difference between the reconstructed vertex $\vec{r}_{\text{igel}}$ and the true vertex of the most energetic cascade $\vec{r}_{\text{true}}$.[4] For muons this is the stochastic energy loss with the greatest energy deposition and for cascades it is the neutrino interaction vertex.

The vertex resolutions in x and y direction are plotted in Fig. 5.18. Both distributions do not differ significantly because no asymmetry of the reconstruction in the horizontal ice layer is expected. Pure cascade events (electron and tau neutrinos) have the best resolution, since the Credo algorithm reconstructs a single cascade. Muon neutrinos are slightly worse because these events contain a track from the charged current interaction along with a cascade from the hadronic remnant. Atmospheric muons have the worst resolution, since these events are tracks which only look cascade-like. The vertex resolution in z direction and the distance $\Delta r = \sqrt{(x_{\text{igel}} - x_{\text{true}})^2 + (y_{\text{igel}} - y_{\text{true}})^2 + (z_{\text{igel}} - z_{\text{true}})^2}$ are shown in Fig. 5.19. The resolution in z direction is asymmetric for atmospheric muons because they are only down-going and the stochastic energy losses are proportional to the energy of the muon. Therefore, many catastrophic energy losses occur just above the detector where the reconstruction is less accurate. The distribution would be symmetric if only those events would be used where the most energetic cascade occurs inside the detector. It can be concluded from Tab. 5.3 that the vertex resolution is in fact of the order of 10 m as stated several times throughout this thesis. Furthermore, by applying quality cuts to select cascade-like events the vertex resolution increases for atmospheric muons at level 4.

In Fig. 5.20 the distribution of the cascade factor is plotted for atmospheric muons and astrophysical electron neutrinos using different seeds. As before, k_{reco} is the reconstructed cascade factor obtained by Millipede with the true vertex and direction seeds. The other two distributions are obtained by two separate Igelfit reconstructions, one seeded with the true vertex of the most energetic cascade and the other with the vertex from the Credo reconstruction. The population of the highest bin ($k = 1$) is due to a misreconstructed vertex. If it is much further away than 10 m from the true vertex, no track hypothesis from the Igelfit can meet the true track or be even slightly parallel to it. Instead, the track which maximizes the Millipede likelihood penetrates the true track at a large angle. Consequently, the reconstructed track only contains few track segments with reconstructed energy losses. The remaining energy depositions along the true track are far off from the reconstructed track. Hence, the cascade factor is $k_{\text{igel}} \simeq 1$ for misreconstructed events. They can simply be removed by applying quality cuts on the existing cascade variables. The resulting distribution of the cascade factor at level 4 (see Sec. 6.1) does not contain the overpopulation of the highest bin anymore. Furthermore, this effect is practically non-existent for neutrino-induced cascades, since the vertex of the Credo reconstruction works well for these events as can be seen in Fig. 5.20 (right).

		atm. μ	**astro. ν_e**	**astro. ν_μ**	**astro. ν_τ**
Level 3	Δx	12.9 m	6.3 m	7.3 m	6.3 m
	Δy	13.8 m	6.5 m	7.7 m	6.5 m
	Δz	6.6 m	3.9 m	4.0 m	3.4 m
Level 4	Δx	8.3 m	5.7 m	6.5 m	5.7 m
	Δy	8.6 m	5.7 m	6.7 m	5.9 m
	Δz	5.6 m	3.5 m	3.7 m	3.5 m

Table 5.3: Vertex resolution of the Igelfit quoted as the standard deviation in a Gaussian fit.

---

[4] As described in Sec. 5.3.1 the vertex seed of the Igelfit is given by the Credo reconstruction in this study. A discussion of the vertex resolution is thus an evaluation of the Credo reconstruction.

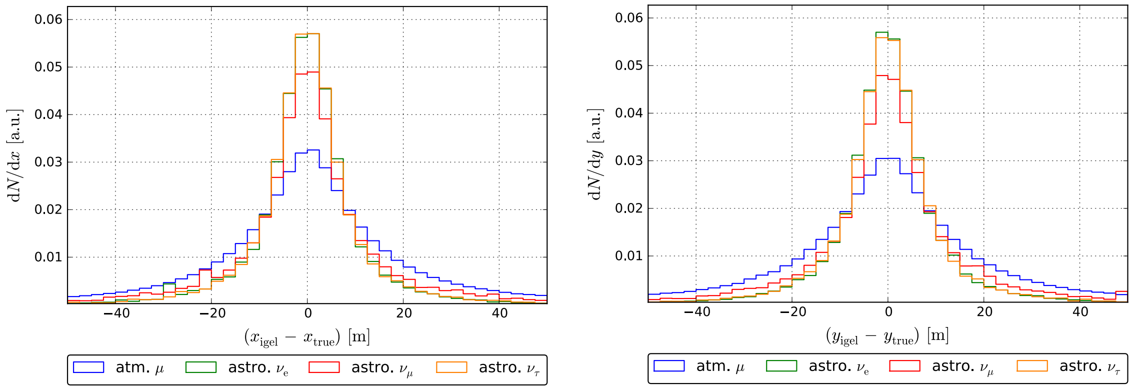

Figure 5.18: Vertex resolution of the Igelfit for x (left) and y (right) direction at level 3.

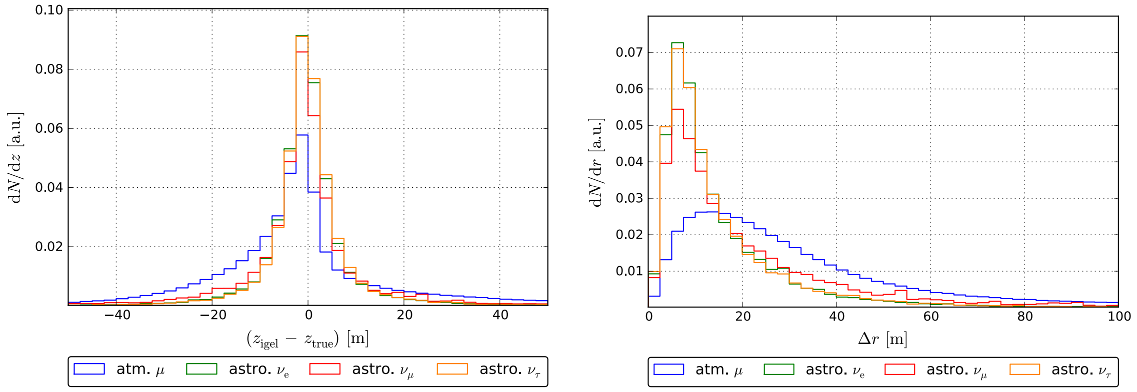

Figure 5.19: Vertex resolution of the Igelfit for z direction (left) and distance Δr (right) at level 3.

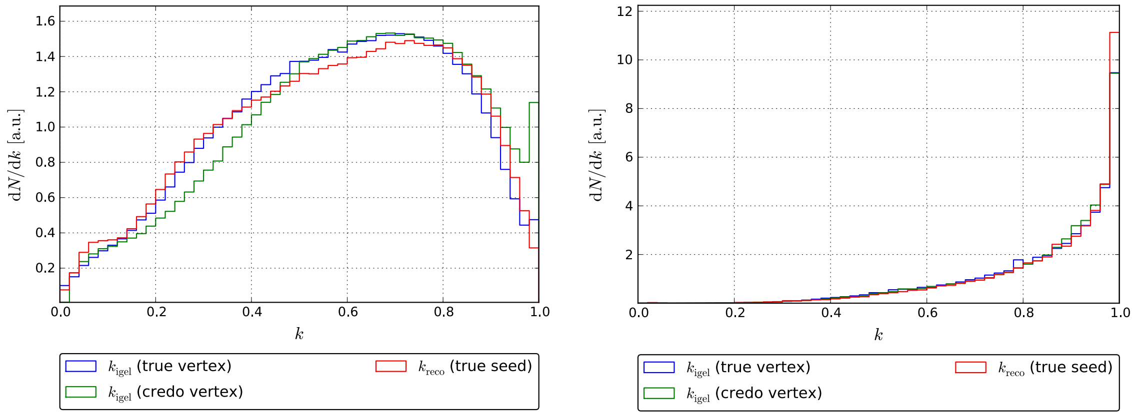

Figure 5.20: The cascade factor of the Igelfit with different vertex seeds for atmospheric muons (left) and astrophysical electron neutrinos (right) at level 3.

5.4.3 Directional Resolution

A precise reconstruction of the direction of a neutrino is essential for many applications. The charged current interaction of muon neutrinos produces a muon which can be selected as up-going track in the detector. Due to the long lever arm the angular resolution is about 1° (c.f. Sec. 4.1). Consequently, muon neutrinos can be used in the search for point sources such as GRBs. The angular resolution for cascades is much worse and only yields a precision of about 30°. Therefore, one aims to measure a diffuse neutrino flux in the cascade analysis. Still, a good directional reconstruction can prove valuable if it is good enough to be employed as cut parameter for cascade-like events which are down-going in the detector.

The preconditions to study the directional resolution are that the MPEFit works well for atmospheric muons and the Credo reconstruction works well for cascades. However, at higher cut levels the majority of events looks cascade-like and the MPEFit becomes ineffective, since it is a track reconstruction. Although the ability of the Credo algorithm to reconstruct muons at higher cut levels increases slightly, it is still intended for cascade reconstructions. That is why the Igelfit as an hybrid tool works well for both tracks and cascades. It can reconstruct muons and neutrinos with an increasing resolution at higher cut levels as will be discussed next.

The directional resolution is defined as the difference between the reconstructed direction and the true direction of the muon or neutrino, respectively. In Fig. 5.21 and 5.22 the resolution of the Igelfit for the zenith angle $\theta_{\text{igel}} - \theta_{\text{true}}$ and for the azimuth angle $\varphi_{\text{igel}} - \varphi_{\text{true}}$ are shown separately for atmospheric muons and for all three neutrino flavors. The azimuth angle is scaled by the cosine of the true zenith angle, since large differences of the azimuth angle near the poles have less impact on the directional resolution than at the horizon. The resolution of the zenith angle is asymmetric for all event types since the Igelfit tends to reconstruct events closer to the horizon than they are. However, a similar tendency is observed for other reconstruction algorithms (see Fig. 5.23). The longer tail towards high values of $\theta_{\text{igel}} - \theta_{\text{true}}$ for the resolution of atmospheric muons is due to the fact that muons are only down-going in the detector. Hence, most muons have a small zenith angle and the reconstruction is asymmetric towards the horizon. The resolution of the azimuth angle is symmetric in all event types, since there are no asymmetries expected for the horizontal direction. The angular resolution of the Igelfit with 128, 256 and 512 iterations is limited to 18°, 13° and 9°, respectively.[5]

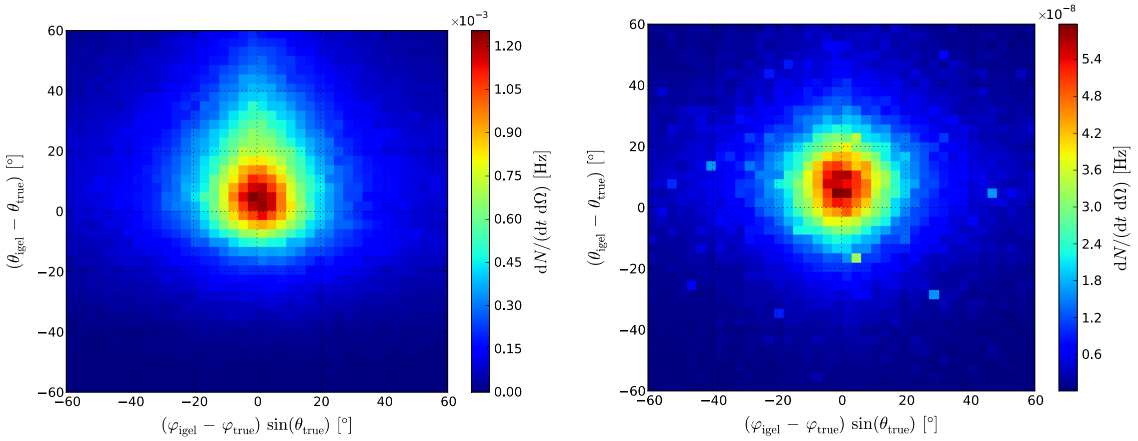

Figure 5.21: Angular resolution of the Igelfit reconstruction for atmospheric muons (left) and electron neutrinos (right) at level 3.

---

[5] The surface area of the sphere is 41 253 square degrees. Dividing the total surface by the number of track directions gives the surface area per track and the square root gives the stated angular resolution.

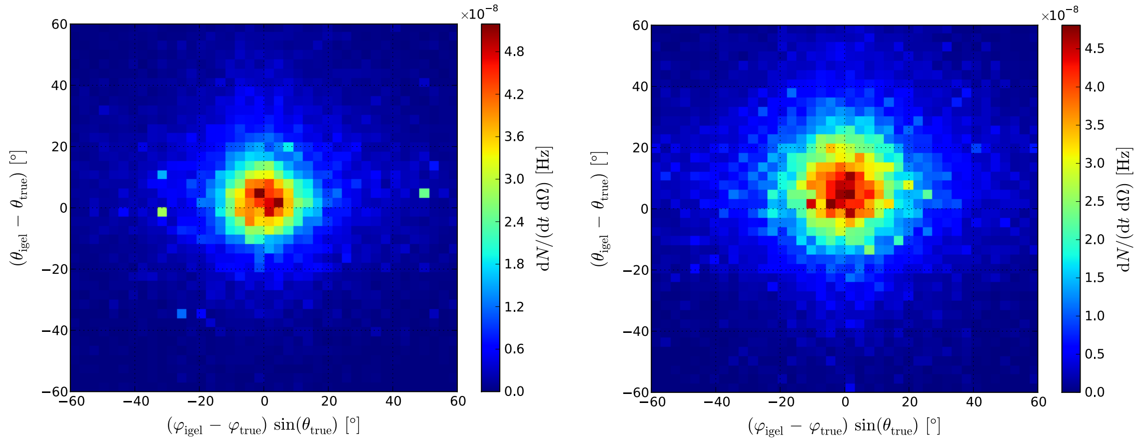

Figure 5.22: Angular resolution of the Igelfit reconstruction for muon neutrinos (left) and tau neutrinos (right) at level 3.

As shown in Fig. 5.21 and 5.22, the Igelfit has about the same angular resolution for electron and tau neutrinos. It is slightly worse for muons due to the asymmetry towards the zenith and better for muon neutrinos. These conclusions are stated Tab. 5.4. At level 3, the resolution of the zenith angle is 22.9° for atmospheric muons, about 19.0° for electron and tau neutrinos and 15.4° for muon neutrinos. The relation is similar for the resolution of the azimuth angle. The resolution is best for muon neutrinos because these are events which contain a track from the muon of the charged current interaction and a cascade from the hadronic remnant and thus are well reconstructed by the Igelfit. At level 4, the angular resolution even increases by a few degrees for all datasets. The angular resolution for electron neutrinos at level 4 is about 16° which is much better than for the Credo reconstruction.

		atm. μ	**astro. ν_e**	**astro. ν_μ**	**astro. ν_τ**
Level 3	$\Delta\theta$	22.9°	19.3°	15.4°	19.0°
	$\Delta\varphi$	20.7°	18.4°	14.6°	18.8°
Level 4	$\Delta\theta$	20.7°	16.2°	14.5°	15.1°
	$\Delta\varphi$	18.0°	16.0°	13.6°	15.3°

Table 5.4: Angular resolution of the Igelfit quoted as the standard deviation from a Gaussian fit.

In comparison, the directional resolution of the Credo reconstruction is plotted for atmospheric muons and electron neutrinos in Fig. 5.23. Electron neutrinos are reconstructed equally well at level 3, however, for muons the Credo reconstruction has a much worse resolution considering both the width of the distribution and the systematic shift. As expected, the MPEFit has a much better resolution for muons as can be concluded from Fig. 5.24. However, there is a significant number of misreconstructed events which are too far off to be visible in the plot. The reconstructed direction of electron neutrinos is completely uncorrelated with the true direction. Only few events are reconstructed correctly, the majority is misreconstructed and not even visible in the plot. Consequently, although the MPEFit works well for muons and the Credo reconstruction for electron neutrinos the reconstructions cannot be used the other way around. In comparison, it follows from Fig. 5.21 that the Igelfit works well for both muons and electron neutrinos. An analysis to select cascade-like events most commonly employs a cut on the zenith angle from a track reconstruction at an early cut stage. In this case, the MPEFit is more effective due to the better angular resolution for tracks at level 3. However, it will be discussed how the cut efficiency of the zenith angle changes at higher cut levels in Sec. 6.1. An improved angular resolution by the Igelfit will prove valuable in this respect.

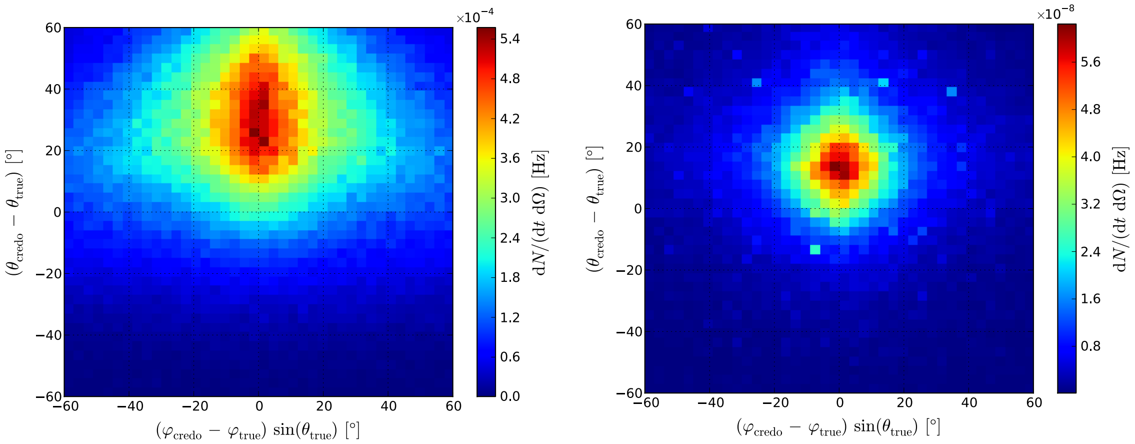

Figure 5.23: Angular resolution of the Credo reconstruction for atmospheric muons (left) and astrophysical electron neutrinos (right) at level 3.

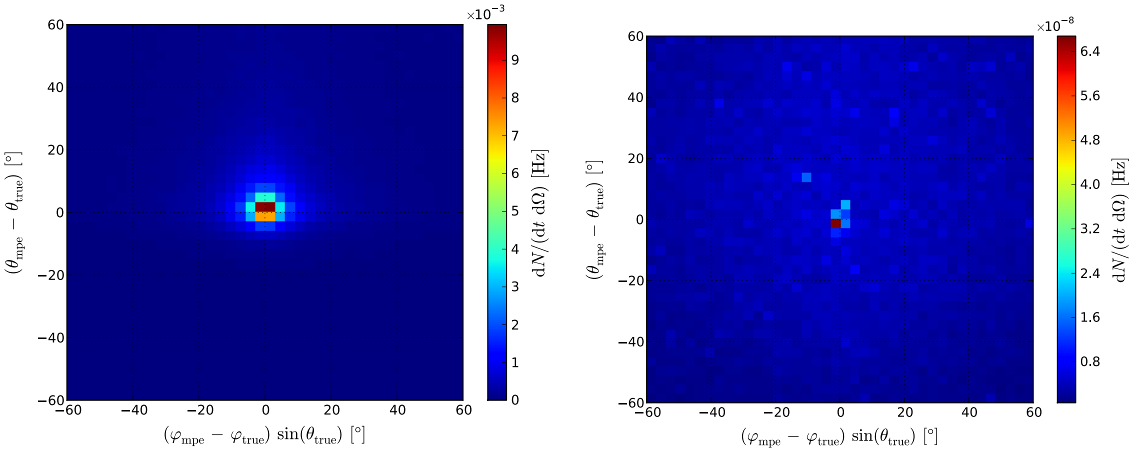

Figure 5.24: Angular resolution of the MPEFit for atmospheric muons (left) and astrophysical electron neutrinos (right) at level 3.

The comparison of the angular resolution for different reconstruction algorithms is more convenient by looking at the projected resolution $\vec{n}_{\mathrm{i}} \cdot \vec{n}_{\mathrm{true}} = \cos(\alpha_{\mathrm{i,\,true}})$ where $\vec{n}_{\mathrm{true}}$ is the true and $\vec{n}_{\mathrm{i}}$ the reconstructed normalized direction vector (i stands for either the Credo reconstruction, the MPEFit or the Igelfit). The resulting distributions are plotted in Figs. 5.25 - 5.26 for levels 3 and 4, respectively. The argument previously stated is supported by a direct comparison. At level 3 the MPEFit works well for muons whereas the Credo reconstruction does not at all. The situation is reversed for electron neutrinos. The quite significant number of misreconstructed events by the MPEFit can be concluded from the small peak around $\cos\alpha_{\mathrm{i,\,true}} \simeq -0.3$. The Igelfit works well for both muons and electron neutrinos. Compared to the MPEFit the resolution is worse for muons and compared to the Credo reconstruction it is equally good for electron neutrinos. At level 4 the directional resolution of the Igelfit is even better, exceeding the resolution of the MPEFit and the Credo reconstruction for both signal and background.

The resolution quoted as the median of the distributions shown in Fig. 5.25 and 5.26 is listed in Tab. 5.5 for different reconstructions. The value of $\Delta\cos\alpha$ is the median of the projection resolution distribution and $\Delta\alpha$ is the corresponding angle for which half of the events are reconstructed better and half worse. This accounts for misreconstructed events close to $\cos(\alpha_{\mathrm{i,\,true}}) \simeq -1$ and yields a convenient comparison of the different reconstruction algorithms.

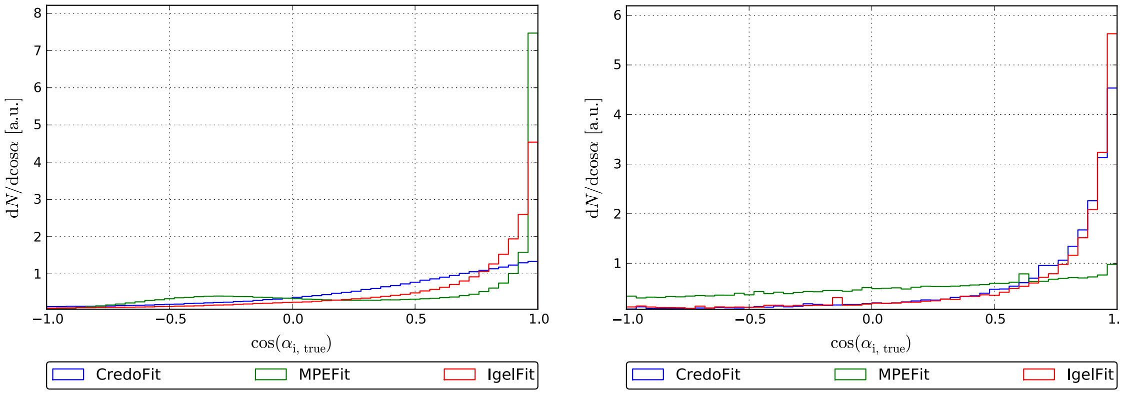

Figure 5.25: Projected directional resolution $\cos(\alpha_{\mathrm{i,\,true}}) = \vec{n}_{\mathrm{i}} \cdot \vec{n}_{\mathrm{true}}$ of different reconstructions for atmospheric muons (left) and astrophysical electron neutrinos (right) at level 3.

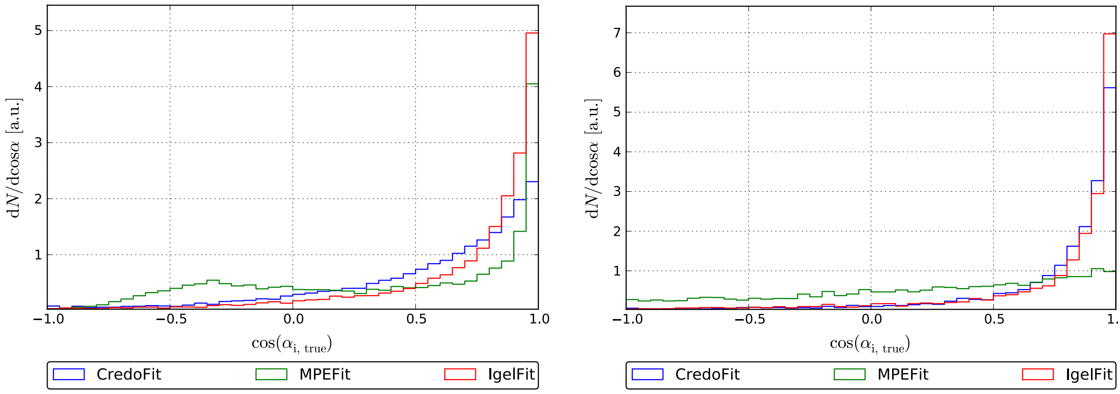

Figure 5.26: Projected directional resolution $\cos(\alpha_{\mathrm{i,\,true}}) = \vec{n}_{\mathrm{i}} \cdot \vec{n}_{\mathrm{true}}$ of different reconstructions for atmospheric muons (left) and astrophysical electron neutrinos (right) at level 4.

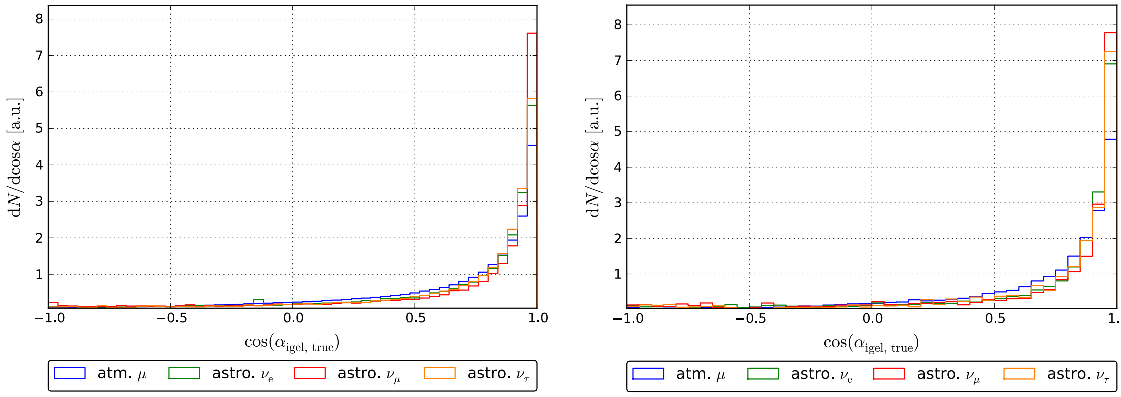

Figure 5.27: Projected directional resolution $\cos(\alpha_{\mathrm{igelfit,\,true}}) = \vec{n}_{\mathrm{igelfit}} \cdot \vec{n}_{\mathrm{true}}$ of the Igelfit for all datasets at levels 3 (left) and 4 (right).

The Igelfit yields the best results for all datasets at level 4 with a resolution of $\Delta\alpha = 36.9^\circ$ for atmospheric muons and $\Delta\alpha = 25.8^\circ$ for all astrophysical neutrinos. The MPEFit has a resolution of $\Delta\alpha = 60.0^\circ$ for atmospheric muons and $\Delta\alpha = 72.5^\circ$ for astrophysical neutrinos. At level 4 the MPEFit yields a much worse resolution, since it is not optimized for the reconstruction of cascade-like events. The summarized directional resolutions of the Igelfit for all datasets are shown in Fig. 5.27 at levels 3 and 4. The resolution is about the same for all datasets and slightly improves at level 4 due to the higher quality of the event selection and the increased number of track directions of the Igelfit. As already discussed, the resolution is slightly worse for atmospheric muons, better for electron and tau neutrinos and best for muon neutrinos, since as per construction the Igelfit can handle events best which contain both a track and a cascade. These events are observed for contained charged current interactions of muon neutrinos. The resolution still is good for pure cascades such as the charged current interactions of the electron and the tau neutrinos. For tau neutrinos this is at least true if the energy is low enough as not to observe a double bang.

		atm. μ		**astro.** ν_e		**astro.** ν_μ		**astro.** ν_τ	
		$\Delta\cos\alpha$	$\Delta\alpha$	$\Delta\cos\alpha$	$\Delta\alpha$	$\Delta\cos\alpha$	$\Delta\alpha$	$\Delta\cos\alpha$	$\Delta\alpha$
Level 3	**Igelfit**	0.76	40.5°	0.80	36.9°	0.84	32.9°	0.84	32.9°
	Credo	0.52	58.7°	0.80	36.9°	0.68	47.2°	0.80	38.9°
	MPEFit	0.68	47.2°	0.20	78.5°	0.32	71.3°	0.24	76.1°
Level 4	**Igelfit**	0.80	36.9°	0.90	25.8°	0.90	25.8°	0.90	25.8°
	Credo	0.65	49.5°	0.85	31.8°	0.80	36.9°	0.85	31.8°
	MPEFit	0.50	60.0°	0.30	72.5°	0.30	72.5°	0.30	72.5°

Table 5.5: Angular resolution quoted as the median of the distributions shown in Fig. 5.25 and Fig. 5.26.

In conclusion, the Igelfit is a reconstruction tool which improves the directional resolution for cascade samples at high cut levels significantly. For the measurement of the diffuse neutrino flux this is very important as the Igelfit yields the zenith angle as a potentially powerful cut parameter. Furthermore, a good directional resolution of neutrino-induced cascades is important for any analysis searching for astrophysical point sources such as gamma ray bursts and supernova remnants. The directional resolution obtained from the Igelfit, however, is not good enough for this application. It has been shown that the Igelfit yields at least four potential cut parameters. Their cut efficiencies will be discussed at levels 3 and 4 in the following chapter.

6. Results of the Igelfit

The Igelfit as a new hybrid reconstruction tool for tracks and cascades has been described in the previous chapter. The implementation, the reconstruction performance and the resolution of the Igelfit have been discussed. In this chapter the results obtained from the Igelfit are presented. In the first section the potential of the cut parameters derived from the Igelfit is discussed with respect to the cut efficiencies at the common cascade level 3 and the custom level 4. In the second section further potential applications are described. The cascade factor obtained from the Igelfit could possibly be used for neutrino flavor identification as well as for composition studies of the cosmic ray flux.

6.1 Event Selection

In this section the event selection with the goal to obtain a purer cascade sample is explained. Since this sample is only used to study the cut parameters derived from the Igelfit, a full cut optimization is omitted. In the first part the cut parameters and values used to define the customized level 4 are explained. In the second part the cut efficiencies of the Igelfit variables are determined and the results are discussed by a comparison to standard cascade variables.

6.1.1 Cut Parameters used to define Level 4

The first step to define a custom cascade level 4 is another run of the Credo reconstruction with eight iterations. Since the cut parameters used to define level 3 are calculated using the the Credo reconstruction with one iteration, this is repeated. The cut parameters as described in Sec. 4.3.3 and 4.3.4 are:

- reduced log-likelihood of the CascadeLlh vertex reconstruction (rlogl),
- tensor of inertia eigenvalue ratio (q),
- fill ratio (f),
- containment of the vertex of the Credo reconstruction,
- veto on the first DOM hit on the DOM hit with the maximum charge.

The reduced log-likelihood of the CascadeLlh vertex reconstruction from level 2 is used as a quality criterion. The tensor of inertia eigenvalue ratio and the fill ratio, respectively, are recalculated using a cleaned series of pulses and the vertex of the Credo reconstruction with eight iterations. The cuts are used to select cascade-like events and thereby tightened. The vertex of the Credo reconstruction is required to be contained inside the detector. A veto technique is employed by demanding that the first DOM hit and the DOM hit with the maximum charge do not occur at the edges of the detector.

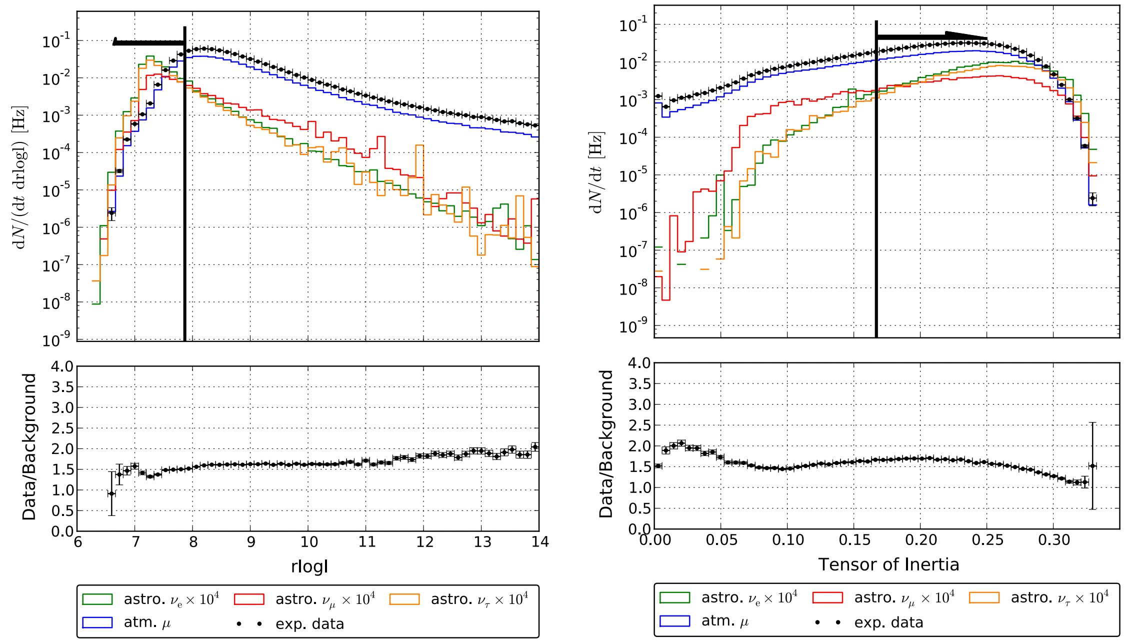

Figure 6.1: The distributions of the reduced log-likelihood from the CascadeLlh vertex reconstruction (left) and the tensor of inertia eigenvalue ratio (right) at level 3. The cuts are indicated.

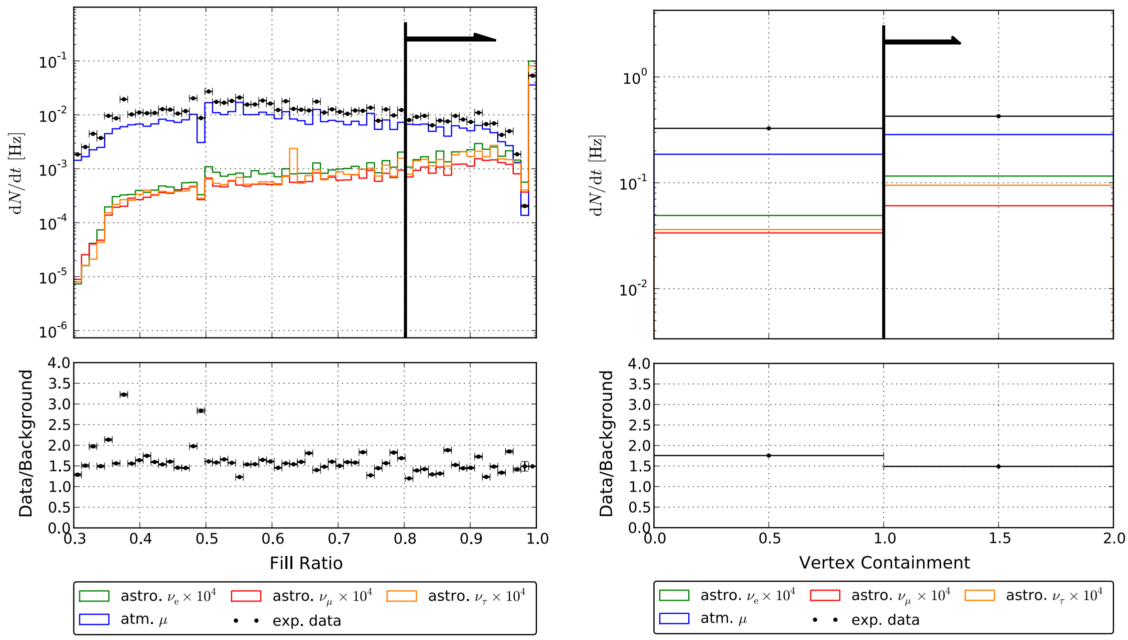

Figure 6.2: The distributions of the fill ratio (left) and the containment criterion of vertex of the Credo reconstruction (right) at level 3. The cuts are indicated.

The distributions of the cut parameters are plotted in Fig. 6.1 - 6.5. For each distribution the absolute event rates are shown. The astrophysical neutrino events are modeled with an E^{-2} flux and normalized to $4 \cdot 10^{-8}\ \mathrm{GeV\,cm^{-2}\,s^{-1}\,sr^{-1}}$. Since the background of atmospheric muons is much larger, the astrophysical neutrino distributions are scaled by a factor of 10^4. Below each distribution, the agreement between data and simulation is shown. For an ideal cut parameter it should stay constant for at least the range which is relevant for a potential cut. Furthermore, if the simulation were perfect, this constant factor should be equal to one. It has already been stated in Sec. 4.4 that this is not the case and that the trigger rate for experimental data is approximately a factor 1.6 greater than for simulated data.

In Fig. 6.1 (left) the reduced log-likelihood from the CascadeLlh vertex reconstruction is plotted. It is lower for neutrino-induced cascades in comparison to atmospheric muons. A possible cut could be at rlogl ≤ 7.8 where the background rate drops below its peak. In the right figure the tensor of inertia eigenvalue ratio is shown. The background distribution is very cascade-like and peaks at $q \simeq 0.25$. Still, it has a broad tail towards low values. A possible cut could be at $q \geq 0.2$ to find a good balance between discarding background but keeping signal events.

The fill ratio is plotted in Fig. 6.2 (left). The peak for both signal and background is at $f \simeq 1$. However, atmospheric muons have a much broader tail down to small values. A possible cut could be at $f \geq 0.8$ where still enough signal events are kept. In the right figure the vertex containment of the Credo reconstruction is shown. The vertex is contained if its x and y coordinates are inside the most outer polygon as shown in Fig. 6.3 and $|z| \leq 500$ m. The fraction of well-reconstructed cascades increases by using contained events only (see Sec. 6.1.2).

In Fig. 6.4 the distributions of the first DOM hits are shown, split in vertical (left) and horizontal layers (right). The vertical layers are numbered starting with 0 at the center strings and ending with 5 at the outer strings (see Fig. 6.3). The DOMs per string are numbered from 1 to 60. The horizontal layers are divided into five segments: layer 0 for DOMs 1 - 4, layer 1 for DOMs 5 - 8, layer 2 for DOMs 9 - 52, layer 3 for DOMs 53 - 56 and layer 4 for DOMs 57 - 60. These values are chosen to see the impact of possible cuts on these regions. The event rate is obviously the highest for the layers which contain the greatest number of DOMs, i.e. the outer most vertical layer and the middle horizontal layer. A possible cut could be to discard events which have the first DOM hit at the outer most vertical layer and at the lowest and highest horizontal layers. That way even a perfectly contained and cascade-like looking event will be filtered if the first DOM hit is at the edge of the detector to account for the possibility that this might in fact have been a muon which left no further track marks.

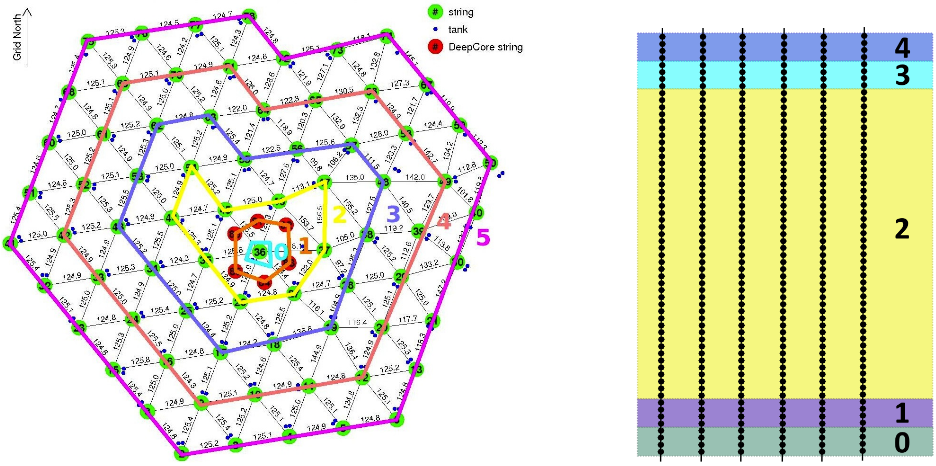

Figure 6.3: Segmentation of the IC79 detector into vertical (left) and horizontal layers (right).

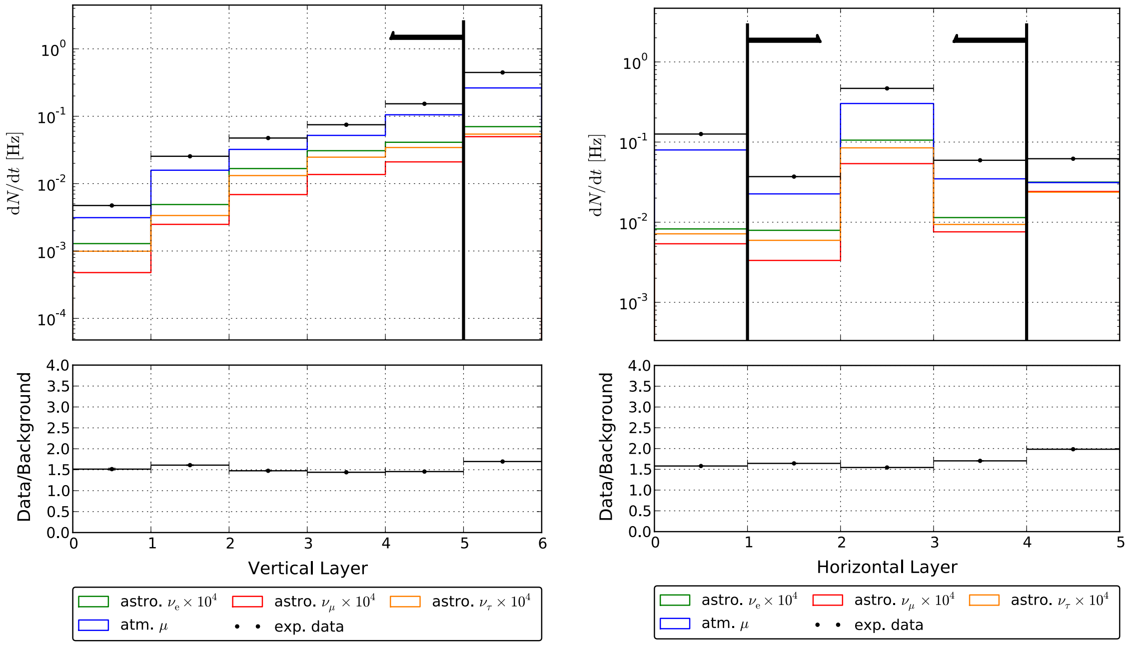

Figure 6.4: The distributions of the first DOM hits for the vertical (left) and the horizontal layers (right) at level 3. The cuts are indicated.

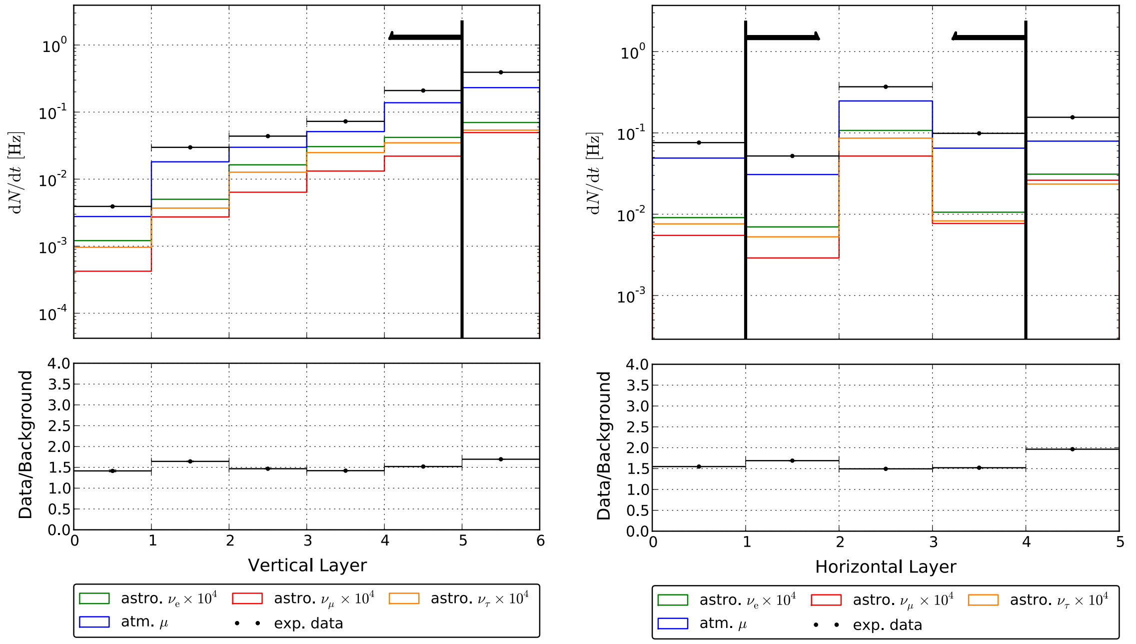

Figure 6.5: The distributions of the DOM hits with the maximum charge for the vertical (left) and the horizontal layers (right) at level 3. The cuts are indicated.

The distributions of the DOM hits with the maximum charge are plotted in Fig. 6.5 for the vertical (left) and the horizontal layers (right). The description is the same as for the distribution of the first DOM hits. The possible cut values on the vertical and horizontal layers are the same as well. The argument with the maximum DOM hit is to define an even stricter containment criterion where not only the reconstructed cascade vertex has to be inside the detector but also the maximum detected charged should not be at the edges of the detector. This cut increases the quality of cascade-like events, since the reconstruction of events at the edge of the detector are less precise than the reconstruction of well-contained events.

The cut values used to define level 4 are obtained by an optimization of the $S/\sqrt{B}$ estimator for each cut parameter individually, where S is the distribution of astrophysical electron neutrinos and B the distribution of atmospheric muons:

reduced log-likelihood: rlogl ≤ 7.678
fill ratio: $f \geq 0.802$
tensor of inertia eigenvalue ratio: $q \geq 0.167$
vertex containment: x and y inside the polygon $\wedge$ $|z| \leq 500$ m
veto on the first DOM hit: vertical layer ≤ 4 $\wedge$ $1 \leq$ horizontal layer ≤ 3
veto on the maximum DOM hit: vertical layer ≤ 4 $\wedge$ $1 \leq$ horizontal layer ≤ 3

These cut values are not fully optimized. In particular, they are applied consecutively, where a full cut optimization would be based on developing a boosted decision tree. Also, the cuts are applied without considering any energy dependence, i.e. in contrast to the level 3 processing these cuts are not turned off for energies above 10 TeV (c.f. Sec. 4.4). The reason is that the focus of this study is the behavior of the cut parameters from the Igelfit at different cut levels. Since there was no commonly defined cascade level 4 for IC79 at the time of this study, a simple but quite realistic cut level needed to be defined.

The event rates at level 3 and at level 4, after applying the aforementioned cuts consecutively, are listed in Tab. 6.1. The background rate is suppressed by around 98.5% and the total signal efficiency is 33.1%. A full cut optimization including the energy dependence would most likely give a higher signal efficiency although the obtained value is high enough for the focus of this study. The discrepancy of the trigger rate for experimental and simulated data stays approximately constant. Since level 4 only applies lose cuts, the background rate is still about 1 000 times greater than the expected signal rate.

	Experimental Data	**Atmospheric μ**	**Astrophysical ν_e**
Level 3 Rate	$6.7 \cdot 10^{-1}$ Hz	$4.7 \cdot 10^{-1}$ Hz	$1.6 \cdot 10^{-5}$ Hz
Level 4 Rate	$9.9 \cdot 10^{-3}$ Hz	$7.7 \cdot 10^{-3}$ Hz	$5.3 \cdot 10^{-6}$ Hz
Cut Efficiency	1.5%	1.6%	33.1%

Table 6.1: Event rates and cut efficiencies at level 3 and level 4 for experimental data, atmospheric muons (background) and astrophysical electron neutrinos (signal).

The distributions of the potential cut parameters from the Igelfit are shown at level 3 and at level 4 in Figs. 6.6 - 6.9. The cascade factor looks very different at level 4 while the zenith angle does not change in shape. This is expected and will be discussed in more detail in the following section. The distribution of the total deposited energy lacks high-energy events, in particular for muon simulations, since the level 4 cuts are not optimized with respect to the energy. Therefore, the distributions for both atmospheric muons and astrophysical neutrinos lack statistics at higher energies. The distribution of the likelihood ratio of atmospheric muons falls off faster at level 4 which has a positive effect on the cut efficiency as will be discussed in the following section.

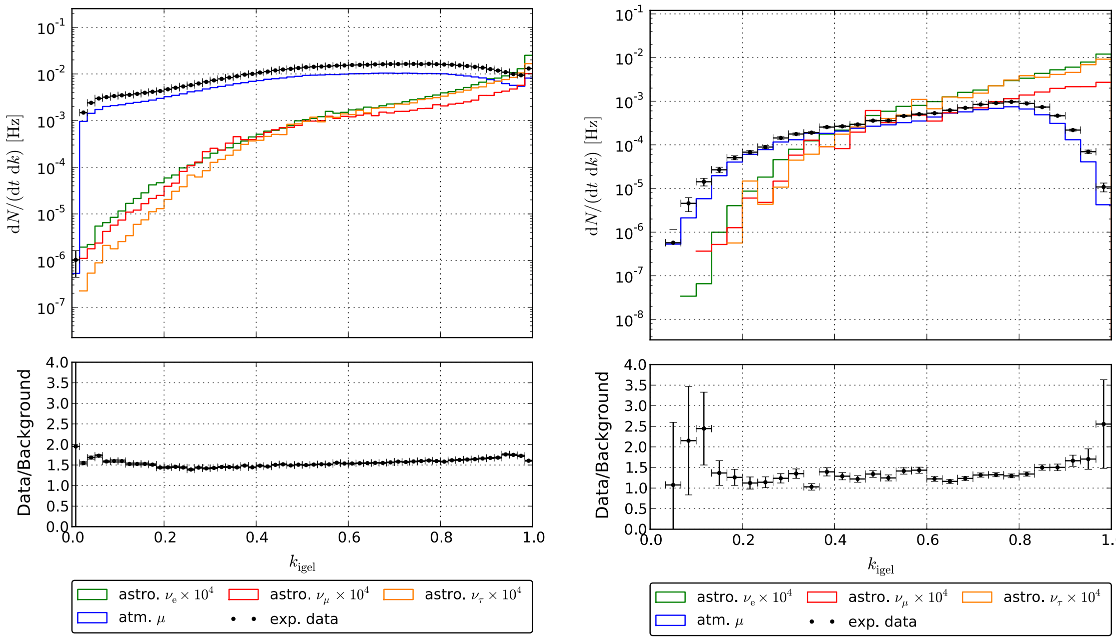

Figure 6.6: The distributions of the cascade factor from the Igelfit at level 3 (left) and at level 4 (right).

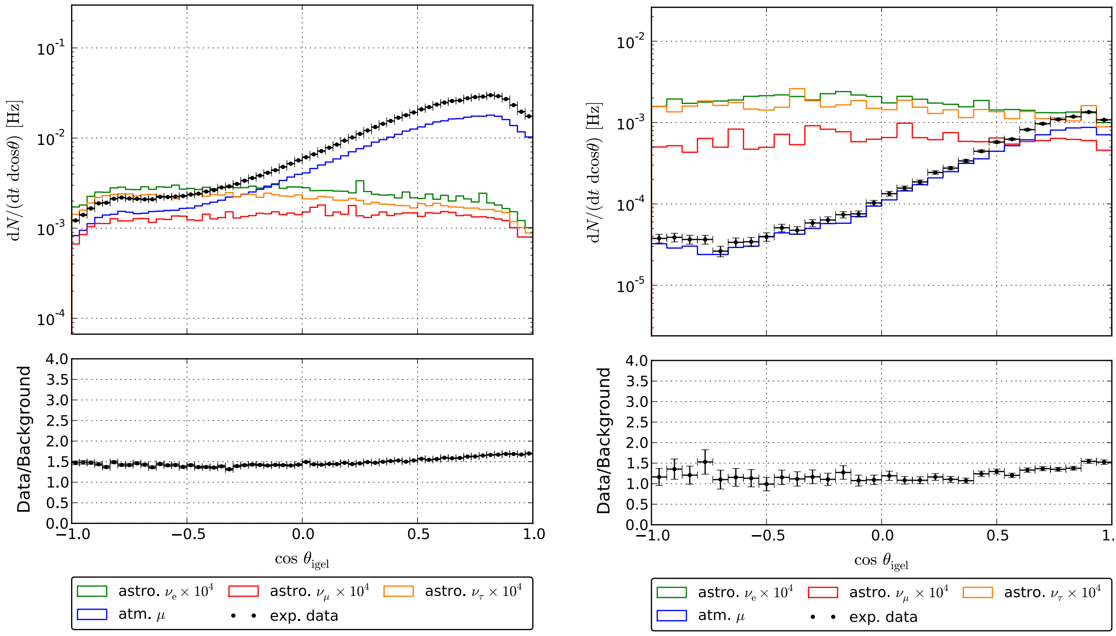

Figure 6.7: The distributions of the zenith angle from the Igelfit at level 3 (left) and at level 4 (right).

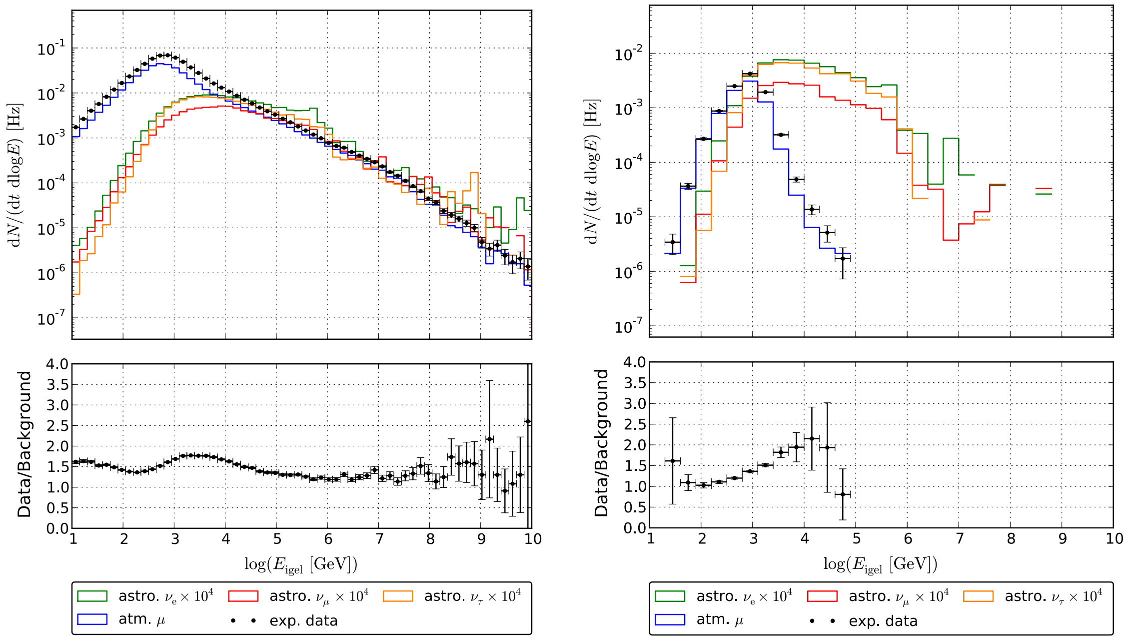

Figure 6.8: The distributions of the total energy from the Igelfit at level 3 (left) and at level 4 (right).

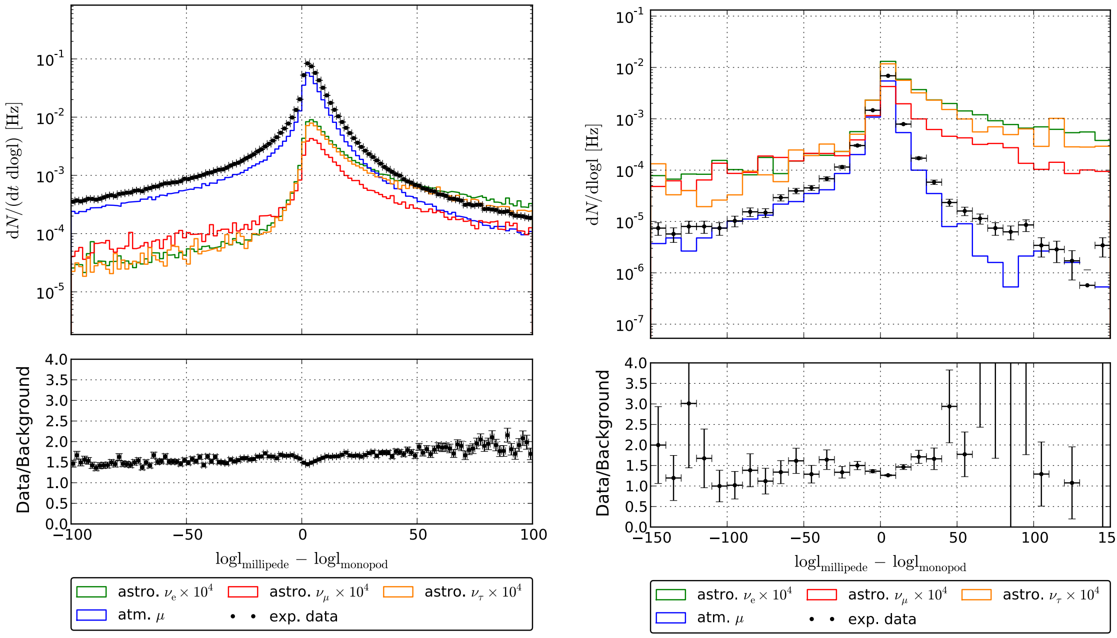

Figure 6.9: The distributions of the likelihood ratio from the Igelfit at level 3 (left) and at level 4 (right).

6.1.2 Cut Efficiencies of the Igelfit Variables

In the last the section the cascade level 4 has been defined by using several cascade variables from established reconstruction algorithms. The resulting distributions of the four potential cut parameters k_{igel}, $\cos\theta_{\text{igel}}$, E_{igel} and $\text{logl}_{\text{millipede}} - \text{logl}_{\text{monopod}}$ derived from the Igelfit have been shown for levels 3 and 4. In this section the change in the distributions of the cascade factor and the zenith angle (as two examples) with respect to the level 4 cuts will be discussed in more detail. It will be concluded that compared to cut parameters from other reconstruction algorithms all four cut parameters derived from the Igelfit have the potential to improve the discrimination between signal and background even at higher cut levels.

The distribution of the cascade factor changes a lot when applying consecutive cuts. The development of the cascade factor is plotted in Fig. 6.10 for background (left) and signal (right) with respect to each cut. The first distribution (no cuts) is equivalent to level 3. The level 4 cuts are applied consecutively until the last cut (tensor of inertia) is reached which is equivalent to level 4. The distributions at levels 3 and 4 are separately shown again in Fig. 6.11 and 6.12, respectively, in comparison with the cascade factor obtained from the Millipede reconstruction seeded with the true vertex and direction and with track of the MPEFit. The reconstruction of the MPEFit yields a track which can be used as fixed seed for the Millipede reconstruction. Thereby a cascade factor from another reconstruction algorithm is obtained as a reference.

There are several conclusions to be drawn. First, the peak of the background distribution only moves slightly to a larger value from $k_{\text{igel}} \simeq 0.7$ to $k_{\text{igel}} \simeq 0.8$. This is reasonable considering the majority of muon events at higher cut levels are expected to look more cascade-like. Second, the tail of the distribution to lower values becomes much flatter with each cut. This is also understandable because the track-like events with lower values are filtered out by the level 4 cuts. And third, the misreconstructed events in the highest bin ($k = 1$) are practically completely eliminated. The last result can be seen by comparing Fig. 6.11 and 6.12 and is particularly important, since this is the critical signal regime. Also, the agreement between k_{reco} and k_{igel} increases significantly at level 4 whereas the cascade factor from the MPEFit does not describe k_{reco} well in any case. The shape of the signal distribution does not change much. This is expected, since the cuts are chosen to retain the signal events. The very few misreconstructed events with a small cascade factor are filtered out by the level 4 cuts. The agreement between k_{reco} and k_{igel} is equally good for both cut levels and the cascade factor from the MPEFit, again, does not describe k_{reco} well.

The shape of the zenith angle distribution does not change much when applying consecutive cuts. This can be concluded from Fig. 6.13 for background (left) and signal (right). For both background and signal the zenith angle distribution does not change its shape but is only scaled down with each cut. This is reasonable, since it is not expected that the direction is correlated to how cascade-like an event looks. In Fig. 6.14 and 6.15 the distributions are plotted separately for levels 3 and 4. The true zenith angle and the reconstructed zenith angle of the Igelfit agrees except for a few misreconstructed events. For comparison the zenith angle of the Credo reconstruction with eight iterations is shown because it is the prevalent way of reconstructing the cascade direction. It can be concluded that the Credo reconstruction gives worse results for the separation of background and signal. Atmospheric muons are mostly misreconstructed which is actually expected from a pure cascade reconstruction. However, there are also many misreconstructed neutrino-induced cascades which in both figures can be seen by means of the overpopulation of the lowest $\cos\theta$ bin. The Igelfit clearly delivers an improvement of the directional resolution compared to existing reconstructions.

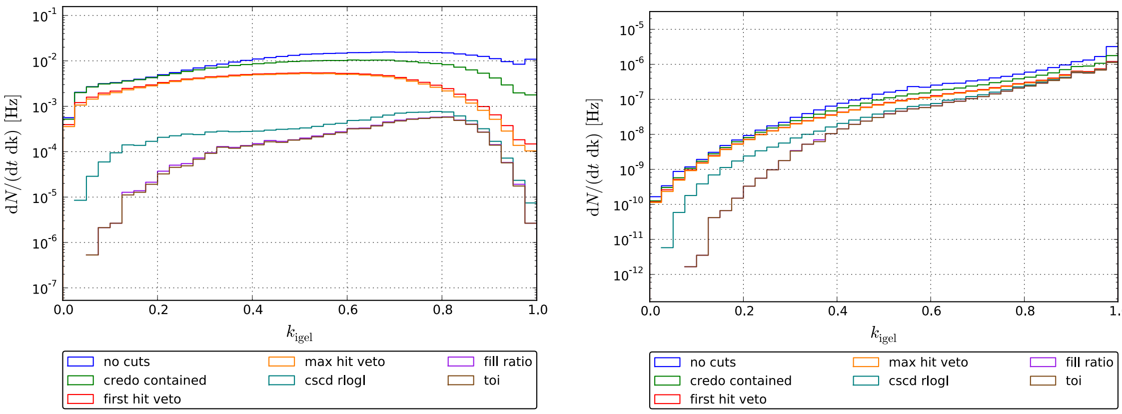

Figure 6.10: The distribution of the cascade factor from the Igelfit for the cumulative level 4 cuts for background (left) and signal (right).

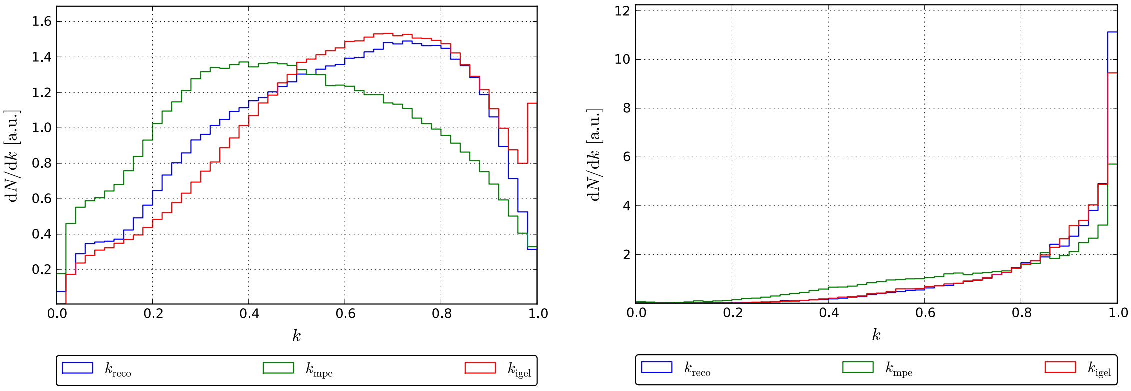

Figure 6.11: The distributions of the cascade factor from different reconstructions for background (left) and signal (right) at level 3.

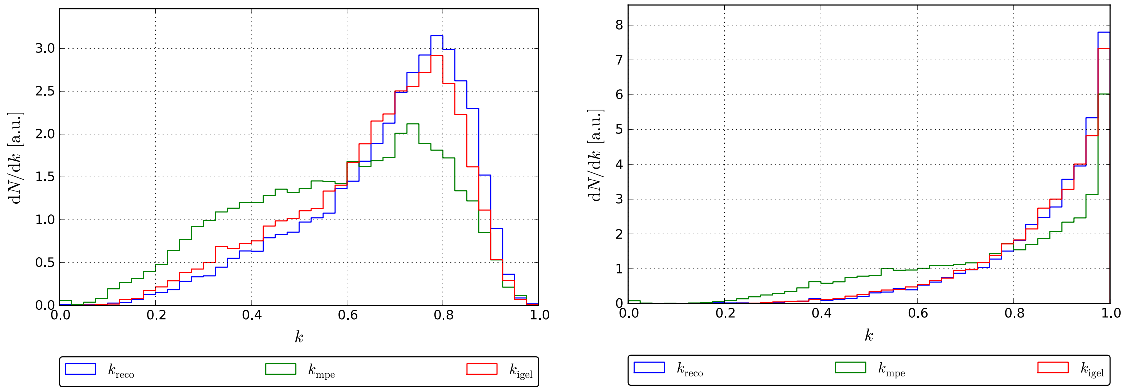

Figure 6.12: The distributions of the cascade factor from different reconstructions for background (left) and signal (right) at level 4.

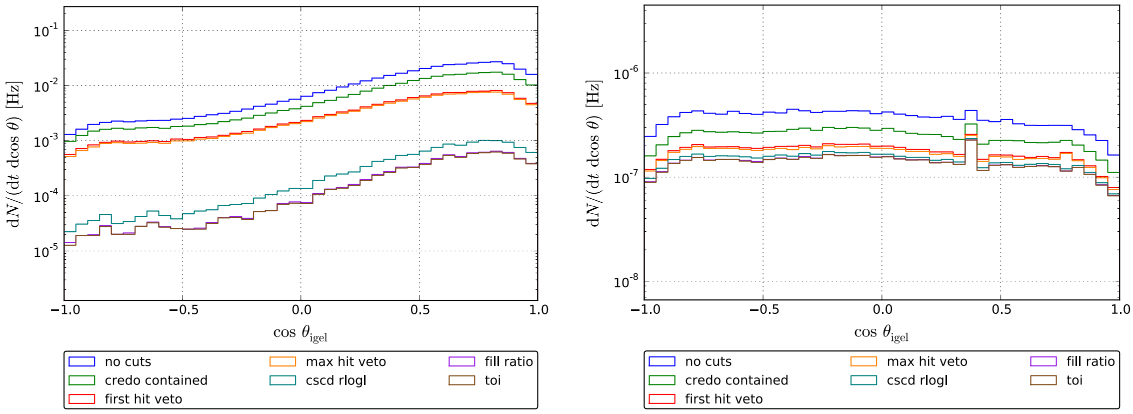

Figure 6.13: The distribution of the zenith angle from the Igelfit for the cumulative level 4 cuts for background (left) and signal (right).

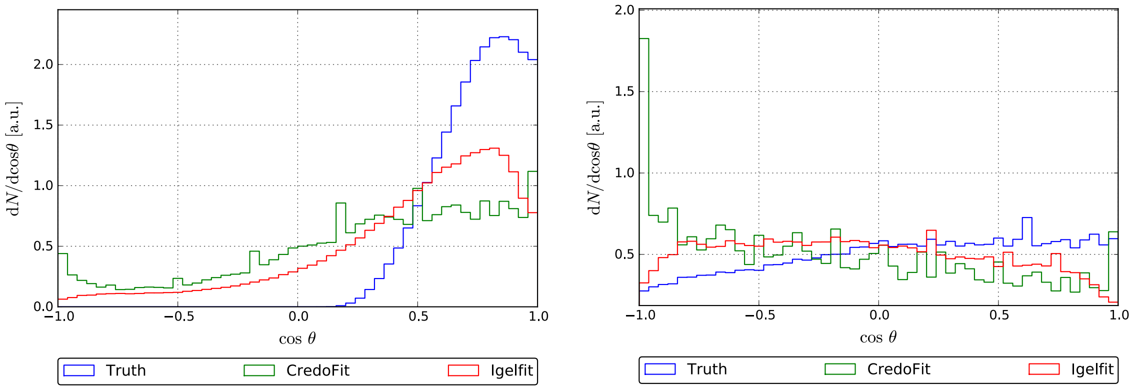

Figure 6.14: The distributions of the zenith angle from different reconstructions for background (left) and signal (right) at level 3.

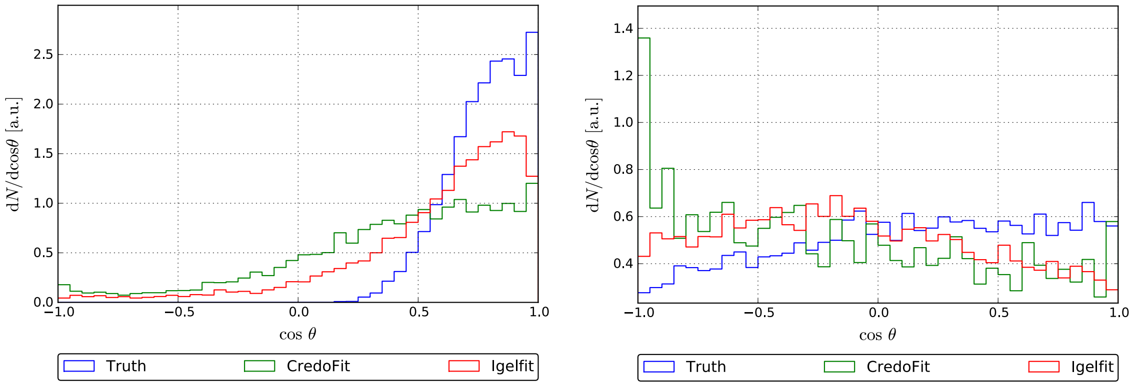

Figure 6.15: The distributions of the zenith angle from different reconstructions for background (left) and signal (right) at level 4.

The question remains whether the potential cut parameters can be effectively used for the discrimination between background and signal and, hence, whether the Igelfit is valuable for the cascade analysis. To answer this question one needs to take a look at the cut efficiencies. The signal efficiency ε_s is plotted against the background efficiency ε_b for different cut parameters at levels 3 and 4 in Fig. 6.16 - 6.18. The efficiency for a certain cut is calculated by counting the number of remaining events and dividing it by the total number of events. This is repeated for a variety of cut values separately for signal and background events resulting in the distributions shown. All curves go through the points $(1,1)$, i.e. no cut is applied and all signal and background events remain, and $(0,0)$, i.e. the cut being so tight that all signal and background events are discarded. A cut is useless if it produces a cut efficiency curve below the bisecting line. The wider the plateau of the curve is, the more effectively the cut can be applied.

The cut efficiencies of the Igelfit parameters and the cascade variables used to define level 4 are plotted in Fig. 6.16. The reduced log-likelihood from the CascadeLlh reconstruction is the most powerful cut parameter, as indicated before. Also, the fill ratio still is the second most effective cut parameter. The cut parameters k_igel and $\mathrm{logl}_\mathrm{millipede} - \mathrm{logl}_\mathrm{monopod}$ of the Igelfit are better than the tensor of inertia but worse than the variables mentioned before. This changes drastically at level 4. Obviously, the cut parameters used for the level 4 filter become less effective. It is, however, valuable that the cut parameters from the Igelfit improve. Although the reduced log-likelihood still has the better cut efficiency over a wide range, the cascade factor and the likelihood ratio give the better result in the critical cut regime. For example, if one demands a further background suppression of 98% at level 4 the reduced log-likelihood would only retain about 8% of the signal events. The cascade factor, however, would have a signal efficiency of over 50% for the same background suppression and is similar for the likelihood ratio. Hence, k_igel and $\mathrm{logl}_\mathrm{millipede} - \mathrm{logl}_\mathrm{monopod}$ are expected to become valuable cut parameters for the cascade analysis.

In Fig. 6.17 the cut efficiencies of the zenith angle from the MPEFit, the Credo reconstruction and the Igelfit are shown. The Igelfit yields the best results in both cases. Although a cut on the zenith angle of the MPEFit is effective at a high background suppression, due to the bad resolution for neutrino-induced cascades it is not recommended to be employed (c.f. Sec. 5.4.3). The Igelfit has a better resolution and far less misreconstructed up-going muon events. Therefore, $\cos\theta_\mathrm{igel}$ might in fact become useful for very pure cascade samples.

The cut efficiencies of the total energy derived from the Millipede reconstruction using the MPEFit as seed, from the Credo reconstruction and from the Igelfit are plotted in Fig. 6.18. The energy obtained from the Millipede reconstruction using the MPEFit as fixed seed results in the most effective cut parameter, since the MPEFit does a better job in reconstructing track-like muons. The energy as cut parameter becomes more effective at level 4. It could be used to filter atmospheric muons at energies below 10 TeV. The cut efficiency of the MPEFit decreases because the majority of events look cascade-like. Since the cascade vertex from the Credo reconstruction is used as vertex seed for the Igelfit, both reconstructions yield similar cut efficiencies for the total energy. Hence, no benefit from E_igel is expected besides a slightly different approach to measure the energy.

In conclusion, the cascade factor and the likelihood ratio turn out to be valuable cut parameters for the cascade analysis. The search for neutrino-induced cascades could also benefit from the zenith angle due to the improved directional resolution (c.f. Sec. 5.4.3). A proposed cut optimization should be developed in dependence of the energy similar to the level 3 filter (c.f. Sec. 4.4) Although it is important to obtain the total energy from the fit, there is no direct benefit compared to the energy of the Credo reconstruction. Hence, the Igelfit is able to provide three powerful cut parameters for future analyses.

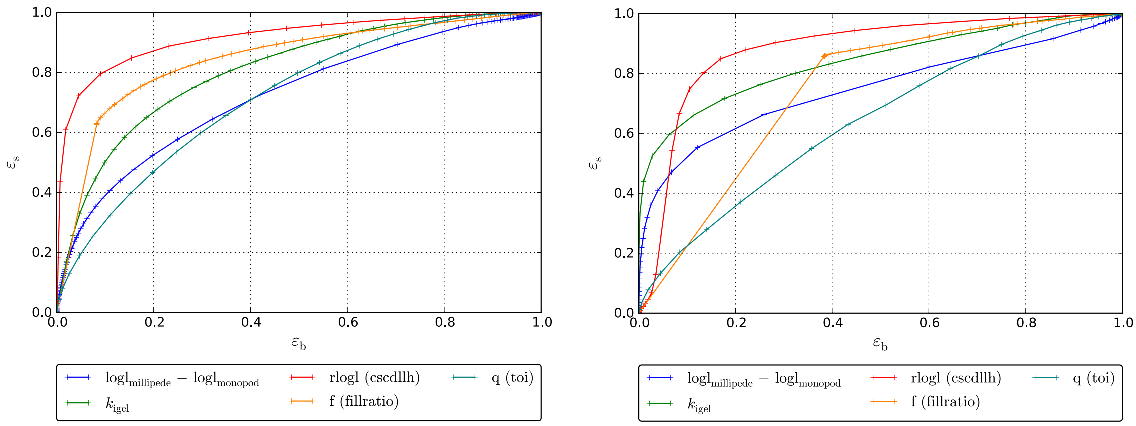

Figure 6.16: Cut efficiencies for different cut parameters at level 3 (left) and at level 4 (right).

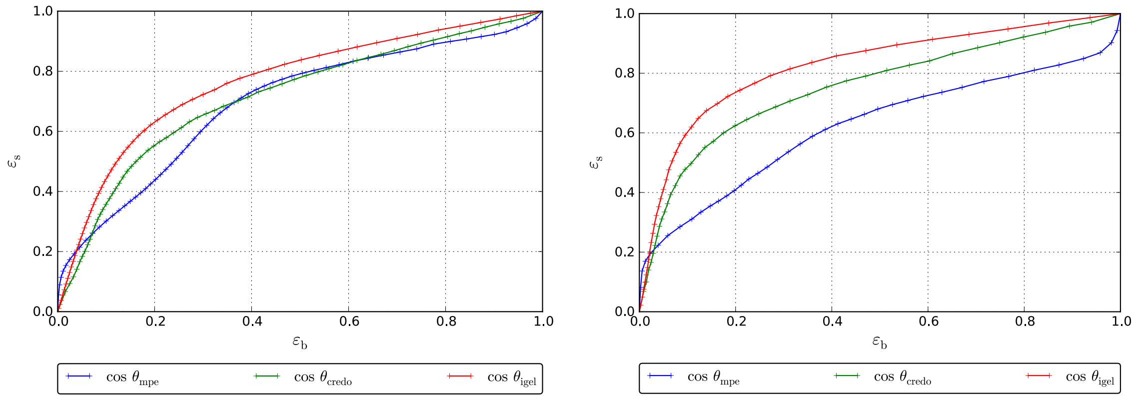

Figure 6.17: Cut efficiencies for the zenith angle from different reconstructions at level 3 (left) and at level 4 (right).

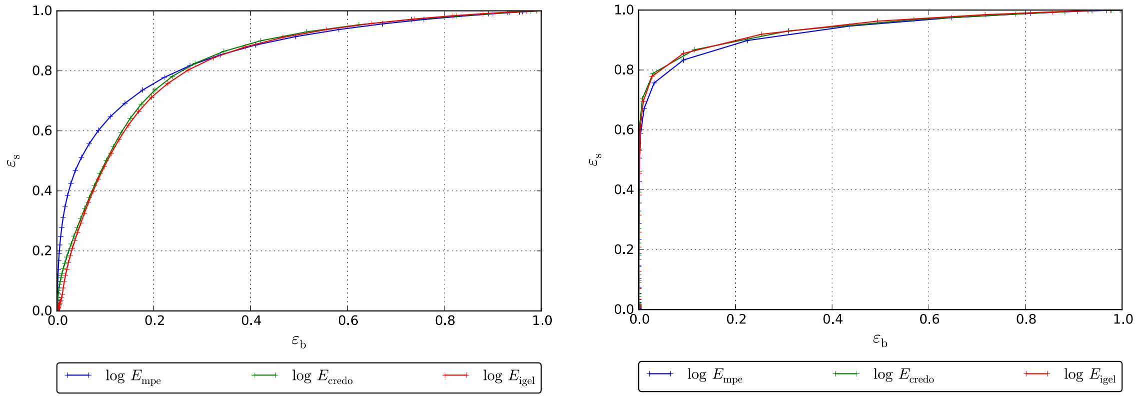

Figure 6.18: Cut efficiencies for the total energy from different reconstructions at level 3 (left) and at level 4 (right).

6.2 Further Applications

The cascade factor was introduced in Sec. 5.2.2 as a way to quantify how cascade-like an event looks. It was proposed in Sec. 6.1.2 to potentially use the cascade factor from the Igelfit as a cut parameter for the cascade analysis. One feature of the cascade factor that has not been explicitly stated so far is that it can be calculated for any reconstruction algorithm which reconstructs vertex and direction of an event. Consequently, the cascade factor can be used to study neutrinos in very pure cascade samples but also to study muons for samples containing clean tracks.

This section is about two potentially interesting applications of the cascade factor. Since detailed studies would be beyond the scope of this thesis, only the main idea is presented. The first application would be to study the distribution of the cascade factor on a very pure sample of neutrino-induced cascades. The goal is to find small differences in the shape of the distribution for the different neutrino flavors. Possibly, this would allow for flavor identification. The second application is to study the cascade factor on a large sample of muons with respect to their primaries. Differences in the shape of the distribution would be associated with the composition of the cosmic ray flux.

6.2.1 Neutrino Flavor Identification

The possibility to identify the flavor of a neutrino event is important for many analyses such as the study of neutrino oscillations. The cascade factor quantifies the total energy loss of the secondary shower particles along the incident neutrino direction. For all neutrino flavors a peak at $k = 1$ is expected due to the neutrino-induced cascade, i.e. the hadronic shower from the interaction with a nucleus in the ice. A pure hadronic cascade is expected in equal numbers and shape for all neutral current interactions. The charged current interactions, however, are different depending on the neutrino flavor. An electron neutrino produces an electron in the charged current interaction which loses its complete energy in an electromagnetic shower at the same location as the hadronic shower. A muon neutrino produces a muon which (depending on the energy) leaves a track in the detector starting at the location of the hadronic cascade. A tau neutrino produces a tau lepton which immediately decays into leptons and hadrons thus producing a second mixed shower in the incident hadronic shower from the ice nucleus. At very high energies the tau can propagate far enough to cause the double bang signature where the primary cascade and the secondary cascade from the tau decay can be resolved. The energy loss distribution and, hence, the cascade factor is different in all three cases.

In Fig. 6.19 the true cascade factor is plotted separately for a pure neutrino sample of all flavors for the neutral and charged current interactions and for all interactions. The range of the cascade factor that is shown is limited to $k \in [0.4, 1.0]$, since cascade events predominantly occur at $k_{\text{true}} \simeq 1$. The widening of the distribution to small values is due to the ionization correction which was introduced in the definition of the cascade factor in Eq. 5.1. The distributions of the neutral interactions are equal for all three flavors, as expected. The charged current interactions of the electron and the tau neutrino are approximately equal as well. A slight difference in the shape can be spotted for the highest bin. For a double bang signature at high energies the Millipede reconstruction could be able to resolve the two subsequent cascades via the reconstructed energy losses if their distance is greater than the vertex resolution. Consequently, the cascade factor would drop significantly to smaller values, depending on how the tau neutrino energy is split between both cascades. The missing tau neutrino events at the highest bin of the distribution would be shifted towards smaller values and evenly distributed.

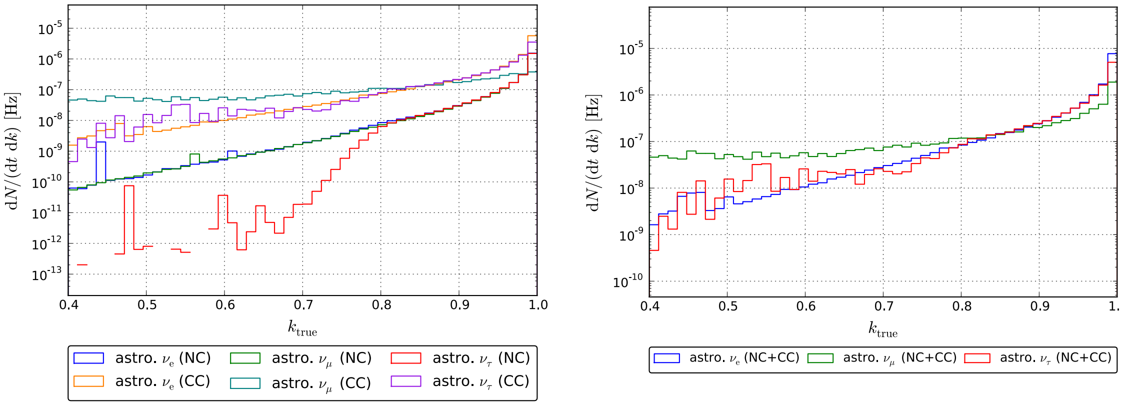

Figure 6.19: True cascade factor for NC and CC interactions (left) and for all interactions (right) for all three flavors at level 3.

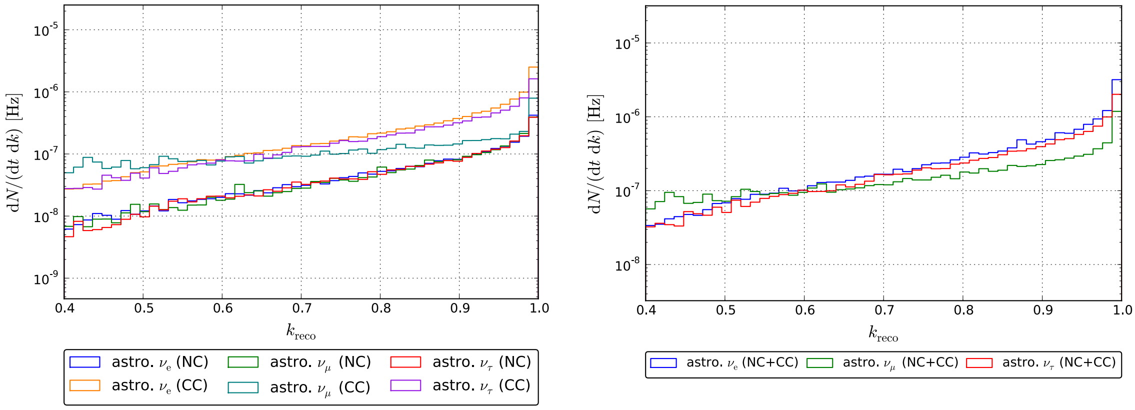

Figure 6.20: Reconstructed cascade factor for NC and CC interactions (left) and for all interactions (right) for all three flavors at level 3.

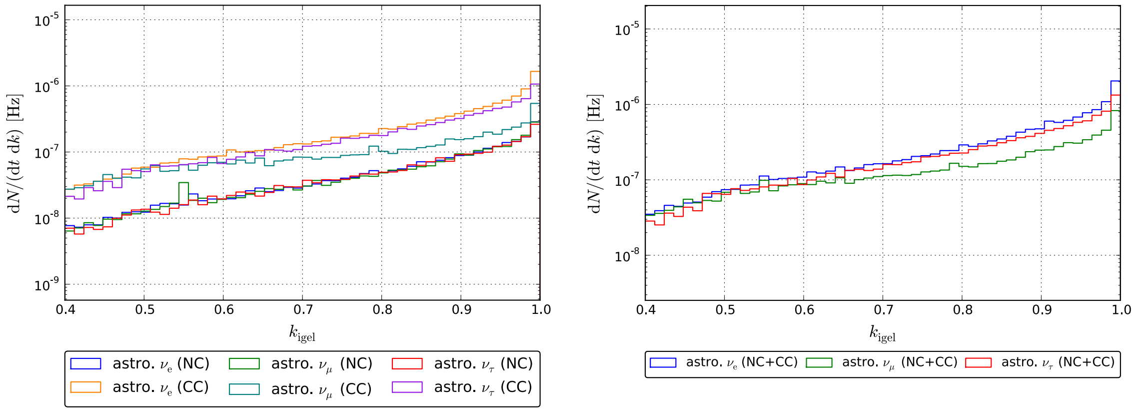

Figure 6.21: Cascade factor from the Igelfit for NC and CC interactions (left) and for all interactions (right) for all three flavors at level 3.

The charged current interaction of the muon neutrino clearly separates from the other neutrino flavors. As expected, the distribution of the cascade factor is much flatter due to the produced muon which generates a track-like energy loss distribution and, hence, smaller values of k_{true}. Since it is not possible to distinguish the neutral current interactions for each flavor, one needs to look at the sum of both interaction channels for each flavor as shown in the right plot of Fig. 6.19. Although the distribution of the muon neutrino still stands out and the differences between all flavors in the highest bin remain the differences become more subtle.

The same distributions are plotted for the reconstructed cascade factor from the true seed and from the Igelfit in Fig. 6.20 and 6.21, respectively. The differences become much more subtle due to the limited resolution of the reconstruction. Still, the shape of the distribution for the muon neutrinos is reconstructed relatively well. An optimization of the muon neutrino channel with respect to the cascade factor from the Igelfit could be promising and the result could potentially be a three composition fit for a number of measured neutrino events to identify the flavor with a certain confidence.

Obviously, there are a lot of obstacles with this application. The neutral current interactions are irreducible and cannot be resolved for different flavors. Most importantly, the distributions shown are only for neutrinos without any background of atmospheric muons at level 3. A pure cascade sample is hard enough to achieve and even then the statistics would most likely be too low to obtain a significant result. Furthermore, the resolution of the cascade factor is not good enough to retain the subtle differences between the flavors well enough.

Still, this application has potential with respect to a new neutrino detector called PINGU which is being planned [CC12]. It is supposed to work like DeepCore (c.f. Sec. 3.1) but with an even higher instrumentation density and a higher quantum efficiency of the photo detectors. Consequently, the spatial resolution would be much better and, hence, the energy loss distribution by the Millipede reconstruction would be much more precise. With PINGU the cascade factor from the Igelfit might become sensitive enough to allow for flavor identification.

6.2.2 Cosmic Ray Composition

The composition of the cosmic ray flux is studied in detail by IceTop (c.f. Sec. 3.1). Another method could be to analyze the energy loss distributions of muons associated with cosmic ray primaries. The idea is that the cascade factor can be used to study the composition of the cosmic ray flux by reconstructing muons from the cosmic ray shower. Protons are very light compared to iron and penetrate the atmosphere much deeper before interacting while iron already interacts at a greater height. Consequently, if iron interacts with the atmosphere the depth of the extensive air shower is longer and more muons sharing parts of the initial cosmic ray energy are produced. If a cosmic ray proton interacts with the atmosphere, the shower depth is much shorter. In this case there are less muons produced in the shower and, hence, the probability to generate a single highly energy muon is greater than for iron primaries.

The distribution of the cascade factor is expected to peak at low values for muons produced in the interaction of iron primaries and at high values for muons from cosmic ray protons. This is due to the increasing probability that a muon undergoes a catastrophic energy loss if the muon is highly energetic. Furthermore, if a single muon traverses the detector the catastrophic energy loss causes the whole event to look cascade-like. This is different for muon bundles. Even if a bundle contains many high energetic muons and even if more than one muon undergoes a catastrophic energy loss in the detector, the event will still look rather track-like because these energy losses will predominantly be distributed evenly along the tracks of the bundle.

This study is based on the muon sample at cascade level 3 because this sample contains many cascade-like muon events but also still has many track-like events. It was concluded in Sec. 5.4.3 that, at level 3, the MPEFit has a better resolution for muons than the Igelfit. The number of misreconstructed events is reduced by demanding a quality criterion of the MPEFit reconstruction. For this first approach, the reduced log-likelihood of the MPEFit is used to select events with $\mathrm{rlogl} < 7.7$.

The true cascade factor is shown for the total muon rate and separately for muons from proton and iron primaries in Fig. 6.22. The distribution for iron primaries peaks at low values and the distribution of proton primaries at higher values. The distributions shown are normalized to compare the shapes. The total rate of muons from iron primaries is much lower due to the lower fraction of iron nuclei in the cosmic ray flux. Still, the total distribution for muons at level 3 has two peaks around $k_{\mathrm{true}} \simeq 0.1$ and $k_{\mathrm{true}} \simeq 0.8$ where the former can be explained by the iron and the latter by the proton contribution of the cosmic ray flux.

Comparing the true distribution to the reconstructed cascade factor from the true seed and from the MPEFit in Fig. 6.23 and 6.24, respectively, a shift of the distribution solely due to the reconstruction becomes obvious. The shift of the distribution towards greater values causes the highest bin $(k = 1)$ to be slightly overpopulated compared to the true distribution. Still, this bin also contains very few cascade-like events from the interaction of iron primaries which are caused by single highly energetic muons. The distribution of the cascade factor from the MPEFit retains the most important features from the reconstructed truth. In particular, the shape of the iron contribution does not change much. This is reasonable because these are track-like events which the MPEFit is able to reconstruct well. Some cascade-like events from the proton contribution, however, are misreconstructed by the MPEFit which causes the distribution of muons from hydrogen primaries to flatten. Consequently, due to the MPEFit and Millipede reconstructions the shape differences for the proton distribution become more subtle compared to the truth. However, they still seem significant enough to attempt a measurement by a two component fit to the total distribution which will be subject to future studies.

Another feature of the relation between the cascade factor and the cosmic ray composition arises from the energy dependence. In Fig. 6.25 the true cascade factor is plotted against the true primary energy for the proton and iron contributions. The event regions are clearly separated with large values of k_{true} and small values of E_{primary} for protons and vice versa for iron. The primary energy cannot be measured with IceCube. Instead the total deposited energy from the Millipede reconstruction for muon tracks can be used. In Fig. 6.26 k_{reco} is plotted against E_{reco}. Both quantities are obtained from the reconstructed energy losses using the Millipede algorithm with the true vertex and direction seed. The different event regions are much closer together as the deposited energy is much lower than the primary energy. The Millipede reconstruction causes the regions to widen as already discussed in Sec. 5.4.1. It can be concluded from Fig. 6.27 that the MPEFit reconstruction agrees with the the distribution of the reconstructed truth and with experimental data.

In conclusion, the proposed application of the cascade factor to study the composition of the cosmic ray flux looks very promising. Using the cascade sample at level 3 with a clean set of muon tracks, this approach could indeed be sensitive to the contribution of protons and iron in the cosmic ray flux. A possible improvement could be to optimize the cascade sample at level 3 for well-reconstructed muons for both track-like and cascade-like events. This could be achieved by combining the results from the MPEFit and the Igelfit reconstructions to remove misreconstructed events. For cascade-like events this could be possible by demanding a certain quality criterion, e.g. that the reconstructed vertices of both reconstructions need to agree within ten meters or the directions within ten degrees.

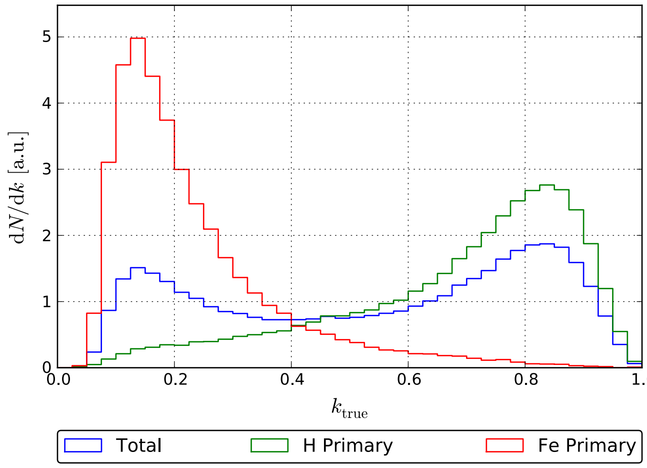

Figure 6.22: True cascade factor for the total muon rate and the separation into muons with H and Fe primaries at level 3.

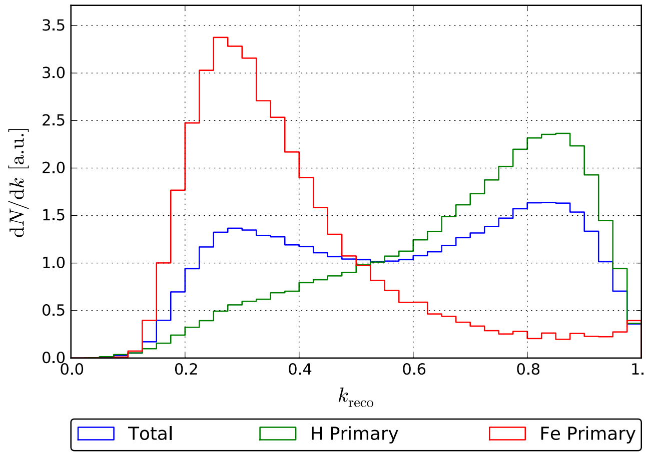

Figure 6.23: Reconstructed cascade factor from the Millipede reconstruction seeded with the true vertex and direction for the total muon rate and the separation into muons with H and Fe primaries at level 3.

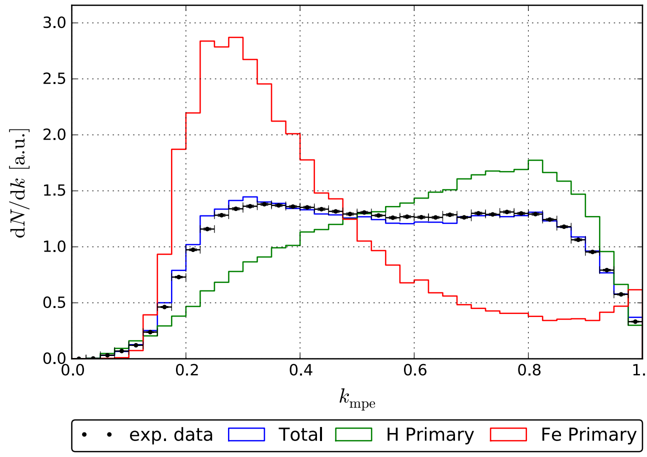

Figure 6.24: Reconstructed cascade factor from the Millipede reconstruction seeded with the track from the MPEFit for the total muon rate and the separation into muons with H and Fe primaries at level 3.

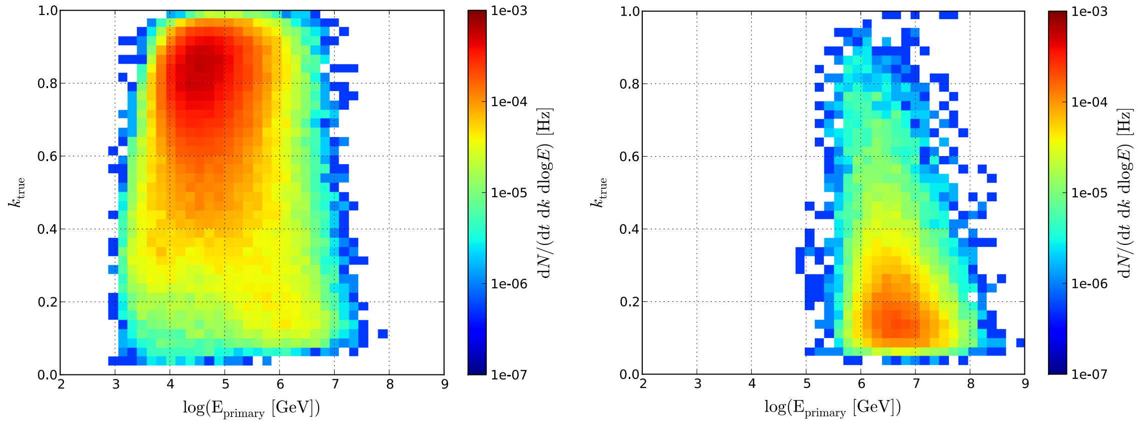

Figure 6.25: True cascade factor in dependence of the true primary energy for muons with H (left) and Fe (right) primaries at level 3

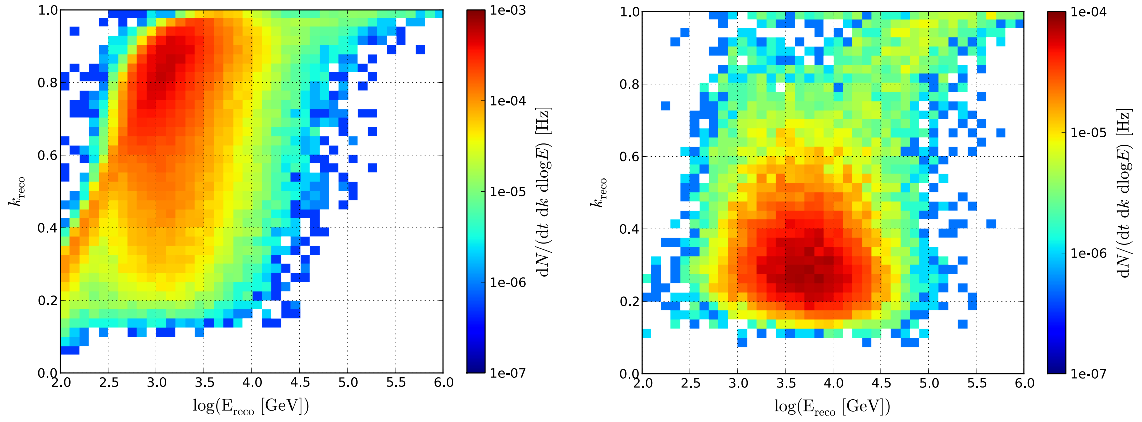

Figure 6.26: Reconstructed cascade factor in dependence of the total deposited energy from the Millipede reconstruction seeded with the true vertex and direction for muons with H (left) and Fe (right) primaries at level 3.

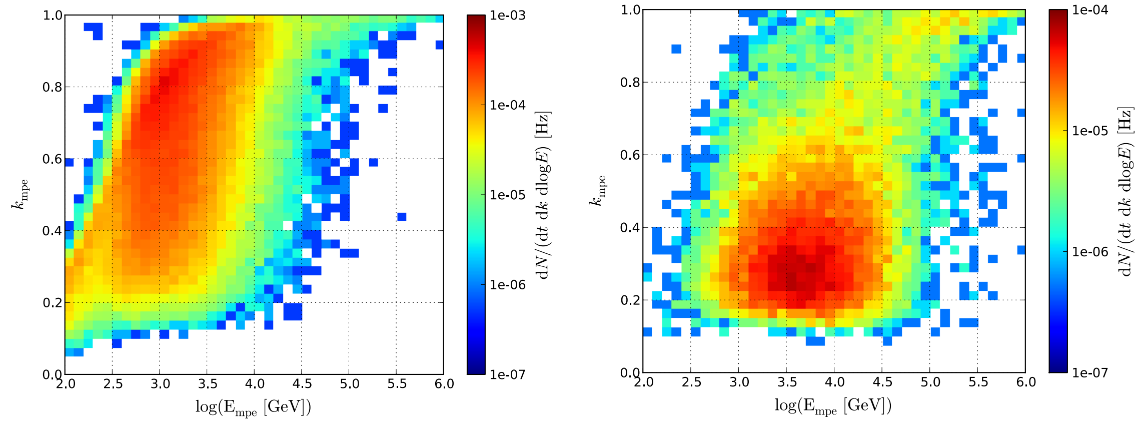

Figure 6.27: Reconstructed cascade factor in dependence of the total deposited energy from the Millipede reconstruction seeded with the track from the MPEFit for muons with H (left) and Fe (right) primaries at level 3.

7. Summary

The sources of the cosmic ray flux containing particles with energies up to 10^{20} eV are still unknown. In most models it is assumed that cosmic rays are accelerated in moving shock fronts which are expected to occur in sources such as GRBs. Associated with cosmic rays, these models also predict a neutrino flux with an E^{-2} spectrum. The IceCube neutrino observatory was built to search for astrophysical neutrinos. It is located at the geographic South Pole and utilizes 1 km^3 of the glacial ice to form a particle detector. Optical modules detect Cherenkov light created by secondary particles in neutrino-induced cascades. Although a recent measurement of two high-energy cascade events with the IceCube detector hint at the discovery of first astrophysical neutrinos [Ish12], it cannot be concluded with absolute certainty yet.

The goal of this thesis was to provide a new reconstruction tool which is helpful in the search for neutrino-induced cascades in the IceCube detector. It was shown that the different energy loss distributions along a track can be used for an event classification which is quantified by the cascade factor. The Millipede algorithm was used to reconstruct the simulated energy losses. It was concluded that the cascade factor can be employed as a new quantity to describe how cascade-like an event looks. Furthermore, the Igelfit was introduced as a new hybrid tool which combines a cascade and a track reconstruction. It uses a reconstructed cascade vertex as fixed anchor point for a multitude of different track directions. For each track direction the Millipede algorithm tries to reconstruct the energy losses along the track which explain the light distribution in the detector best. The fit result is the track hypothesis which maximizes the likelihood. It was shown that the Igelfit yields at least four potential cut parameters, i.e. the cascade factor k_{igel} and the total deposited energy E_{igel} from the reconstructed energy losses, the zenith angle $\cos\theta_{\mathrm{igel}}$ from the track and a likelihood ratio $\mathrm{logl}_{\mathrm{millipede}} - \mathrm{logl}_{\mathrm{monopod}}$ comparing the track to the cascade hypothesis.

The results of the Igelfit were discussed by comparing signal and background datasets at different cascade levels. It was concluded that the cut parameters of the Igelfit still have good cut efficiencies after the existing cut parameters from other reconstruction algorithms were used to obtain a purer cascade sample. In particular, the cascade factor and the likelihood ratio have great potential to discriminate signal and background at high cut levels. Furthermore, it was demonstrated that the Igelfit has a better directional resolution than existing cascade and track reconstructions at higher cut levels. It was shown that the Igelfit works equally well for both signal and background whereas the designated track and cascade reconstructions, MPEFit and Credo, only do in their respective regimes.

Finally, two more potential applications of this study were discussed. It was shown that the cascade factor of the Igelfit has the potential to be used for flavor identification. However, it seems that the current purity of cascade samples and the resolution in IceCube are not good enough for this application to work. This method might become useful for future particle detectors with an increased resolution like PINGU and, in fact, could already be used to study cascade samples from DeepCore, the low-energy extension of IceCube.

The second application of the cascade factor was to study the composition of the cosmic ray flux. The energy loss distribution of muons from cosmic ray protons is slightly different than for muons from iron nuclei. Since this method uses atmospheric muons which are measured in vast numbers, the application is much closer to being usable than the neutrino flavor identification. The development of both applications was beyond the scope of this thesis but could be promising for future analyses.

In conclusion, the approach to use the energy loss distributions for the classification of events has great potential. The emerging cascade factor can be used for different applications, in particular as a cut parameter for the cascade analysis. The Igelfit is a new reconstruction tool that combines track and cascade reconstruction algorithms. It employs the reconstruction of energy losses which yields the cascade factor directly from the reconstruction. The directional resolution for cascade-like events could be improved using the Igelfit.

Future endeavors include ongoing optimizations of the Igelfit reconstruction and a full cut optimization employing the new cut parameters. The complete IceCube detector in its full configuration with 86 strings, an increasingly larger experimental dataset and the combined advancement of different analyses at high cut levels show great promise for the discovery of astrophysical neutrinos in the near future.

A. Implementation of the MCMillipede Module

The distribution of the energy losses of a muon along its track can be used for the classification of the event as described in Sec. 5.2. Many muons produced in the air shower come in bundles which, typically, contain between two and fifty muons. Since it is not possible to distinguish single muons from muon bundle events in IceCube and the Millipede reconstruction works with a single track, the simulated muon bundle events need to be adapted to this situation. The *MCMillipede* module was implemented specifically for this purpose.

Each simulation file has a Monte Carlo tree called *I3MCTree* which contains the full information (time, vertex, direction and energy) of all primary and secondary cascades. Primary cascades are considered to be neutrino-induced and secondary cascades come from the stochastic losses of a muon. The implemented algorithm choses the track which contains the most energetic cascade and projects all secondary cascades from the other tracks within the bundle onto this track. It makes sure to only include cascades which are contained within the cube boundary a. There are three steps in this procedure. The first is to define the track, the second to project all secondary cascades onto this track and the last step is to bin the track and to construct one cascade in each bin which has the total energy of all projected cascades in this bin.

Definition of the track: The track is simply given by the vertex and direction of the most energetic cascade. Let the vertex be $\vec{v} = (v_x, v_y, v_z)$ and let the direction be $\vec{d} = (\cos\varphi\sin\theta, \sin\varphi\sin\theta, \cos\theta)$ with the zenith angle θ and the azimuth angle φ. Then the track can be parameterized via $\alpha \in \mathbb{R}$

$$\vec{r}_{\mathrm{t}} = \begin{pmatrix} v_x \\ v_y \\ v_z \end{pmatrix} + \alpha \begin{pmatrix} \cos\varphi\sin\theta \\ \sin\varphi\sin\theta \\ \cos\theta \end{pmatrix} . \tag{A.1}$$

Now the start and stop point of the track needs to be found. They are defined as the intersections with a cube of dimension $-a \leq x, y, z \leq a$ centered at the origin of the IceCube coordinate center. The surface of the cube is parameterized by six (infinite) planes

$$\vec{r}_{1,2} = \begin{pmatrix} \pm a \\ 0 \\ 0 \end{pmatrix} \quad \text{and} \quad \vec{r}_{3,4} = \begin{pmatrix} 0 \\ \pm a \\ 0 \end{pmatrix} \quad \text{and} \quad \vec{r}_{5,6} = \begin{pmatrix} 0 \\ 0 \\ \pm a \end{pmatrix} . \tag{A.2}$$

The intersections of the track with each of the six planes are given by $\vec{r}_i = \vec{v} + \alpha_i \vec{d}$ with

$$\alpha_{1,2} = \frac{\pm a - v_x}{\cos\varphi\sin\theta} \quad \text{and} \quad \alpha_{3,4} = \frac{\pm a - v_y}{\sin\varphi\sin\theta} \quad \text{and} \quad \alpha_{5,6} = \frac{\pm a - v_z}{\cos\theta} . \tag{A.3}$$

The two intersections with the actual cube (and not the infinite planes) are found by demanding $|r_{i,x}| \leq a$ and $|r_{i,y}| \leq a$ and $|r_{i,z}| \leq a$ for *all* components of one intersection $\vec{r}_i$.

Depending on the z component of the intersection ($z \geq 0$ or $z < 0$) and on the zenith angle θ of the seed track ($0^\circ \leq \theta \leq 90^\circ$ or $90^\circ < \theta \leq 180^\circ$), the start and stop points of the track, $\vec{r}_{\mathrm{start}}$ and $\vec{r}_{\mathrm{stop}}$, are determined by assigning the correct intersections. The track length is given by $l = |\vec{r}_{\mathrm{stop}} - \vec{r}_{\mathrm{start}}|$.

Projection of cascades onto the track: The next step is to project all secondary cascades onto the previously defined track via the projection operator

$$P = \begin{pmatrix} d_x^2 & d_x d_y & d_x d_z \\ d_x d_y & d_y^2 & d_y d_z \\ d_x d_z & d_y d_z & d_z^2, \end{pmatrix} \tag{A.4}$$

where $\vec{d}$ is the direction vector from Eq. (A.1) with $|\vec{d}| = 1$. For an arbitrary cascade at position $\vec{r}_{\mathrm{c}}$ in the muon bundle the projected location of the cascade is given by

$$\vec{r}_{\mathrm{c}}\,' = P(\vec{r}_{\mathrm{c}} - \vec{r}_{\mathrm{start}}) + \vec{r}_{\mathrm{start}}. \tag{A.5}$$

First the cascade position is shifted by the starting point of the track, then it is is projected onto the track and then shifted back. The resulting cascade position is then on the track.

Track segmentation: The last step is to divide the track into segments. With the bin size Δl this gives $n = l/\Delta l$ track segments. The segment which the projected cascade belongs to is determined by $i = |\vec{r}_{\mathrm{c}}\,' - \vec{r}_{\mathrm{start}}|/\Delta l$ with $i = 1, \ldots, n$. For all cascades whose projections are contained within the cube defined by a the energy is summed for each bin and a virtual cascade with the sum of the energies is put into the center of each segment.

The result is written into a vector of *I3Particle* objects, each representing a single cascade located at the center of the track segment with information on energy, vertex, direction and timing taken from the projected cascades. The total track length is l and the number of segments with bin size Δl is n. The result can be used to compare the true energy losses to the reconstructed obtained by the Millipede reconstruction with the true seed (vertex and direction). The module was written in a way that for future references the boundary does not need to be a cube but can also be a cylinder. The track length is then defined by the intersections with that cylinder.

Bibliography

This bibliography includes some references such as internal reports or wiki articles which are only accessible for members of the IceCube collaboration. These references were only included if the work performed by the author was not documented in another way. If access is required, please refer to the author of this thesis or to another member of the IceCube collaboration.

[AMA12] AMANDA Collaboration. The AMANDA II Experiment. `http://amanda.uci.edu/`, August 2012.

[ANT12] ANTARES Collaboration. The ANTARES Experiment. `http://antares.in2p3.fr/`, August 2012.

[B^+10] Ryan C. Bay et al. South Pole Paleowind From Automated Synthesis of Ice Code Records. *Journal of Geophysical Research (Atmospheres)*, 115:D14126, 2010.

[Bar08] Roger Barlow. *Statistics: A Guide to the Use Of Stastistical Methods in the Physical Sciences*. John Wiley & Sons, 2008.

[BDM12] Imre Bartos, Basudeb Dasgupta, and Szabolcs Márka. Probing the Structure of Jet Driven Core-Collapse Supernova and Long Gamma Ray Burst Progenitors with High Energy Neutrinos. *arXiv:1206.0764v1 [astro-ph.HE]*, 2012.

[Bec08] Julia K. Becker. High-energy neutrinos in the context of multimessenger physics. *Physics Reports*, 458:173–246, 2008.

[BG99] Lars Bergström and Ariel Goobar. *Cosmology and Particle Astrophysics*. J. Wiley & Sons, 1999.

[Boe12] David Boersma. Gulliver. `http://wiki.icecube.wisc.edu/index.php/Gulliver`, April 2012.

[Bou96] Paul Bourke. Distributing Points on a Sphere. `http://paulbourke.net/geometry/spherepoints/`, June 1996.

[BZ10] Gerhard Bohm and Guenter Zech. *Introduction to Statistics and Data Analysis for Physicists*. Verlag Deutsches Elektronen-Synchrotron, 2010.

[CC12] Ken Clark and Doug F. Cowen. IceCube/DeepCore and IceCube/PINGU: Prospects for Few-GeV Scale ν Physics in the Ice. *Nuclear Physics B Proceedings Supplement*, 00:1–6, 2012.

[Chi11] Dmitry Chirkin. Study of South Pole ice transparency with IceCube flashers. `http://icecube.wisc.edu/~dima/work/WISC/ppc/spice/paper/a.pdf`, March 2011.

[Chi12] Dmitry Chirkin. Feature Extraction of IceCube Waveforms. `http://www.ifh.de/~kislat/www/icerec/docs/docs_material/FE.pdf`, August 2012.

[CLR$^+$56] Cowan Clyde L., Jr., Frederick Reines, et al. Detection of the Free Neutrino: a Confirmation. *Science*, 124 no. 3212:103–104, 1956.

[CR04] Dmitry Chirkin and Wolfgang Rhode. Propagating Leptons Through Matter with Muon Monte Carlo (MMC). *ArXiv High Energy Physics*, 0407075, 2004.

[D'A11] Michelangelo D'Agostino. AtmCscdEnergyReco Module. `http://www.ifh.de/~kislat/www/icerec/docs/V03-03-01/doxygen/AtmCscdEnergyReco/index.html`, January 2011.

[Day12] Daya Bay Collaboration. Observation of electron-antineutrino disappearance at Daya Bay. *ArXiv High Energy Physics*, 1203.1669v2, 2012.

[DHH68] Raymond Davis, Don S. Harmer, and Kenneth C. Hoffman. Search for Neutrinos from the Sun. *Physical Review Letters*, 20:1205, 1968.

[DV12] Juan Carlos Diaz-Velez. Weights in CORSIKA Simulation Data. `http://wiki.icecube.wisc.edu/index.php/Weights_in_CORSIKA_Simulation_Data`, April 2012.

[ERS08] Rikard Enberg, Mary H. Reno, and Ina Sarcevic. Prompt Neutrino Fluxes from Atmospheric Charm. *Physical Review D*, 78:043005, 2008.

[Fer49] Enrico Fermi. On the Origin of the Cosmic Radiation. *Physical Review*, 75:1169–1174, 1949.

[Fin07] Chad Finley. Weighting NeutrinoGenerator Events with OneWeight in IceSim 2.0. `https://docushare.icecube.wisc.edu/dsweb/Get/Document-44937/OneWeight.pdf`, October 2007.

[Fra11] Anna Franckowiak. *Searching for High-Energy Neutrinos from Supernovae with IceCube and an Optical Follow-up Program*. PhD thesis, Rheinische Friedrich-Wilhems-Universität Bonn, 2011.

[Gai90] Thomas K. Gaisser. *Cosmic Rays and Particle Physics*. Cambridge University Press, 1990.

[GBH08] Sean Grullon, David Boersma, and Gary Hill. Photonics-based Log-Likelihood Reconstruction in IceCube. `http://internal.icecube.wisc.edu/reports/data/icecube/2008/07/001/icecube_200807001_v3.pdf`, June 2008.

[GGM08] Maria C. Gonzalez-Garcia and Michele Maltoni. Phenomenology with Massive Neutrinos. *Physics Reports*, 460:1–129, 2008.

[GK05] Askhat Gazizov and Marek Kowalski. ANIS: High Energy Neutrino Generator for Neutrino Telescopes. *Computer Physics Communications*, 172:203–213, 2005.

[GQRS98] Raj Gandhi, Chris Quigg, Mary Hall Reno, and Ina Sarcevic. Neutrino Interactions at Ultrahigh Energies. *Physical Review D*, 58:093009, 1998.

[Gre66] Kenneth Greisen. End to the Cosmic-Ray Spectrum? *Physical Review Letters*, 16:748–750, 1966.

[Gre11] Michael Greene. CscdLlh Documentation. `http://www.ifh.de/~kislat/www/icerec/docs/V03-03-01/doxygen/cscd-llh/index.html`, January 2011.

[Gru11] Sean Grullon. Tensor of Inertia Code Documentation. `http://www.ifh.de/~kislat/www/icerec/docs/V03-03-01/doxygen/tensor-of-inertia/index.html`, January 2011.

[H^{+}87] Kazuto Hirata et al. Observation of a Neutrino Burst from the Supernova SN1987A. *Physical Review Letters*, 58:1490–1493, 1987.

[HÖ3] Jörg R. Hörandel. On the knee in the energy spectrum of cosmic rays. *Astroparticle Physics*, 19:193–220, 2003.

[H^{+}07] Morihiro Honda et al. Calculation of atmospheric neutrino flux using the interaction model calibrated with atmospheric muon data. *Physical Review Letters D*, 75:043006, 2007.

[Hes12] Victor F. Hess. Über Beobachtungen der durchdringenden Strahlung bei sieben Freiballonfahrten. *Physikalische Zeitschrift*, 13:1084–1091, 1912.

[Hil84] Anthony M. Hillas. The Origin of Ultra-High-Energy Cosmic Rays. *Annual Review of Astronomy and Astrophysics*, 22:425–444, 1984.

[HK10] Francis Halzen and Spencer Klein. Invited Review Article: IceCube: An instrument for neutrino astronomy. *Review of Scientific Instruments*, 81:081101, 2010.

[HM84] Francis Halzen and Alan D. Martin. *Quarks and Leptons: An Introductory Course in Modern Particle Physics*. J. Wiley & Sons, 1984.

[HMWY10] Svenja Hümmer, Michele Maltoni, Walter Winter, and Carlos Yaguna. Energy dependent Neutrino Flavor Ratios from Cosmic Accelerators on the Hillas Plot. *Astroparticle Physics*, 34:205–224, 2010.

[HP09] Dieter Heck and Tanguy Pierog. Extensive Air Shower Simulation with CORSIKA: A User's Guide. `http://www-ik.fzk.de/corsika/usersguide/usersguide.pdf`, April 2009.

[HRR03] Andreas Haungs, Heinigerd Rebel, and Markus Roth. Energy spectrum and mass composition of high-energy cosmic rays. *Reports on Progress in Physics*, 66:1145–1206, 2003.

[Ice01] IceCube Collaboration. IceCube Preliminary Design Document. `www.icecube.wisc.edu/science/publications/pdd/pdd.pdf`, 2001.

[Ice06] IceCube Collaboration. Optical Properties of Deep Glacial Ice at the South Pole. *Journal of Geophysical Research*, 111:D13203, 2006.

[Ice09] IceCube Collaboration. The IceCube Data Acquisition System: Signal Capture, Digitization and Timestamping. *Nuclear Instruments and Methods in Physics Research A*, 601:294–316, 2009.

[Ice11] IceCube Collaboration. Measurement of the Atmospheric Neutrino Energy Spectrum from 100 GeV to 400 TeV with IceCube. *Physical Review Letters D*, 83:012001, 2011.

[Ice12a] IceCube Collaboration. An absence of neutrinos associated with cosmic-ray acceleration in gamma-ray bursts. *Nature*, 484:351–354, 2012.

[Ice12b] IceCube Collaboration. IceCube Construction Timeline. `http://www.icecube.wisc.edu/science/timeline`, August 2012.

[Ice12c] IceCube Collaboration. IceCube Gallery. `icecube.wisc.edu/gallery/view/140`, August 2012.

[Ish12] Aya Ishihara. Search for ultra-high energy cosmic neutrinos with the IceCube neutrino detector. `http://www.icrr.u-tokyo.ac.jp/icrr_seminar/seminars12/20120830_Ishihara.pdf`, August 2012.

[Jac75] John D. Jackson. *Classical Electrodynamics*. J. Wiley & Sons, 1975.

[K+95] Katsuji Koyama et al. Evidence for shock acceleration of high-energy electrons in the supernova remnant SN1006. *Nature*, 378:255–258, 1995.

[Kam08] KamLAND Collaboration. Precision Measurement of Neutrino Oscillation Parameters with KamLAND. *Physical Review Letters*, 100:221803, 2008.

[KAS12] KASCADE Collaboration. KASCADE - Grande. `http://www-ik.fzk.de/KASCADE/`, May 2012.

[KAT01] KATRIN Collaboration. A next Generation Tritium Beta Decay Experiment with sub-eV Sensitivity for the Elctron Neutrino Mass. *ArXiv High Energy Physics*, 0109033, 2001.

[Kay81] Boris Kayser. On the Quantum Mechanics of Neutrino Oscillation. *Physical Review D*, 24:110–116, 1981.

[Kow03] Marek Kowalski. *Search for Neutrino-induced Cascades with the AMANDA-II Detector*. PhD thesis, Humboldt-Universität zu Berlin, 2003.

[Lan11] Hagar Landsman. Linefit Module. `http://www.ifh.de/~kislat/www/icerec/docs/V03-03-01/doxygen/linefit/index.html`, January 2011.

[LMo07] Johan Lundberg, Predrag Miocinovic, and Kurt Woschnagg others. Light Tracking Through Ice and Water - Scattering and Absorption in Heterogeneous Media with PHOTONICS. *Nuclear Instruments and Methods in Physics Research A*, 581:619–631, 2007.

[MAG12] MAGIC Collaboration. The Magic Telescopes. `http://wwwmagic.mppmu.mpg.de/`, September 2012.

[Mal12] Robert S. Mallozzi. The BATSE Gamma Ray Burst Catalogs. `http://gammaray.msfc.nasa.gov/batse/grb/catalog/`, July 2012.

[Mid08] Eike Middell. Reconstruction of Cascade-Like Events in IceCube. Master's thesis, Humboldt-Universität zu Berlin, 2008.

[Mid12] Eike Middell. IC40 Atmospheric Flux Cascade Analysis. `http://wiki.icecube.wisc.edu/index.php/IC40_Atmospheric_Flux_Cascade_Analysis`, August 2012.

[Mig08] Emilio Migneco. Progress and latest results from Baikal, Nestor, NEMO and KM3NeT. *Journal of Physics: Conference Series*, 136:022048, 2008.

[MNS62] Ziro Maki, Masami Nakagawa, and Shoichi Sakata. Remarks on the Unified Model of Elementary Particles. *Progress of Theoretical Physics*, 28:870, 1962.

[MP98] Rabindra N. Mohapatra and Palash B. Pal. *Massive Neutrinos in Physics and Astrophysics*. World Scientific, 1998.

[MP09] Eike Middell and Sebastian Panknin. Request for the Cascade Online Filter. `https://docushare.icecube.wisc.edu/dsweb/Get/Document-48361/2009_TFT_Proposal_Cascade_Filter.pdf`, January 2009.

[Pan96] Dirk Pandel. Bestimmung von Wasser- und Detektorparametern und Rekonstruktion von Myonen bis 100 TeV mit dem Baikal-Neutrinoteleskop NT-72. Master's thesis, Humboldt-Universität zu Berlin, 1996.

[Pan11] Sebastian Panknin. *Search for Neutrino-Induced Cascade Events in the IceCube Detector*. PhD thesis, Humboldt-Universität zu Berlin, 2011.

[Par06] Particle Data Group. Review of Partice Physics: Neutrino Mass, Mixing, and Flavour Change. *Journal of Physics G*, 33, 2006.

[Par08] Particle Data Group. Particle Physics Booklet, July 2008.

[Pau30] Wolfgang Pauli. Offener Brief an die Gruppe der Radioaktiven bei der Gauvereins-Tagung zu Tübingen. `http://microboone-docdb.fnal.gov/cgi-bin/RetrieveFile?docid=953;filename=pauli%20letter1930.pdf`, December 1930.

[Per09] Donald Perkins. *Particle Astrophysics*. Oxford University Press, 2009.

[Pet97] Bradley M. Peterson. *An Introduction to Active Galactic Nuclei*. Cambridge University Press, 1997.

[Pie10] Pierre Auger Collaboration. Measurement of the energy spectrum of cosmic rays above 10^{18} eV using the Pierre Auger Observatory. *Physical Letters B*, 685:239–246, 2010.

[Pon57] Bruno Pontecorvo. Mesonium and anti-mesonium. *Sov. Phys. JETP*, 6:429, 1957.

[Pon68] Bruno Pontecorvo. Neutrino Experiments and the Problem of Conservation of Leptonic Charge. *Sov. Phys. JETP*, 26:984, 1968.

[PR99] Lara Pasquali and Mary H. Reno. Tau Neutrino Fluxes from Atmospheric Charm. *Physical Review D*, 59:093003, 1999.

[PS92] Raymond J. Protheroe and Anthony P. Szabo. High energy cosmic rays from active galactic nuclei. *Physical Review Letters*, 69:2885–2888, 1992.

[Ren06] Mary H. Reno. Neutrino Cross Sections at HERA and Beyond. *Nucl.Phys.Proc.Suppl*, 151:255–259, 2006.

[Rou07] Cécil Roucelle. Documentation for the DOMCalibrator Module. `http://internal.icecube.wisc.edu/reports/data/icecube/2007/09/001/icecube_200709001_v1.pdf`, September 2007.

[Rut11] Doug Rutledge. Project Docs for Fill Ratio. `http://www.ifh.de/~kislat/www/icerec/docs/V03-03-01/doxygen/fill-ratio/index.html`, January 2011.

[Sch05] Stefan Schlenstedt. The IceCube Reconstruction IceRec. `http://glacier.lbl.gov/icecube/meetings/2005/marchmeeting/UPLOADS/FILE064.RcKY1a_stefan-icerec.pdf`, March 2005.

[Sch10] Olaf Schulz. SLC Hit Cleaning. `http://wiki.icecube.wisc.edu/index.php/SLC_hit_cleaning`, November 2010.

[Seu09] Suruj Seunarine. 2010 Request for Online Cascade Filter. `https://docushare.icecube.wisc.edu/dsweb/Get/Document-52559/2010_TFT_CascadeFilter.pdf`, December 2009.

[SNO01] SNO Collaboration. Measurement of the Rate of $\nu_e + d \rightarrow p + p + e^-$ Interactions produced by ^{8}B Solar Neutrinos at the Sudbury Neutrino Observatory. *Physical Review Letters*, 87:071301, 2001.

[Sok10] Pierre Sokolsky. Final Results from the High Resolution Fly's Eye (HiRes) Experiment. In *XVI International Symposium on Very High Energy Cosmic Ray Interactions*, 2010.

[Sup98] Super-Kamiokande Collaboration. Evidence for Oscillation of Atmospheric Neutrinos. *Physical Review Letters*, 81:1562–1567, 1998.

[TB11] Ignacio Taboada and Erik Blaufuss. TFT 2011 Season Planning. `http://wiki.icecube.wisc.edu/index.php/TFT_2011_Season_Planning`, May 2011.

[Ter10] Teresa Montaruli and Christine Lewis and Juan Carlos Diaz-Velez. NeutrinoFlux Service for IceTray. `http://www.icecube.wisc.edu/~tmontaruli/neutrinoflux/NeutrinoFlux.html`, November 2010.

[Toa11] Pat Toale. CLast Documentation. `http://www.ifh.de/~kislat/www/icerec/docs/V03-03-01/doxygen/clast/index.html`, January 2011.

[Voi08] Bernhard Voigt. *Sensitivity of the IceCube Detector for Ultra-High Energy Electron-Neutrino Events*. PhD thesis, Humboldt-Universität zu Berlin, 2008.

[vS12a] Jakob van Santen. IC79 Cascade Level 3. `http://icecube.wisc.edu/~jvansanten/docs/cascadel3_ic79/`, August 2012.

[vS12b] Jakob van Santen. Monopod Reconstruction and Resolution Estimates. `https://docushare.icecube.wisc.edu/dsweb/Get/Document-61906/2012-08-15.pdf`, August 2012.

[W$^+$12] Kurt Woschnagg et al. Dust Logger. `http://wiki.icecube.wisc.edu/index.php/Dust_logger`, August 2012.

[Wal10] Marius Wallraff. Design, Implementation and Test of a New Feature Extractor for the IceCube Neutrino Observatory. Master's thesis, Rheinisch-Westfaelische Technische Hochschule Aachen, March 2010.

[WB99] Eli Waxman and John Bahcall. High Energy Neutrinos from Astrophysical Sources. *Physical Review D*, 59:023002, 1999.

[Wei08] Steven Weinberg. *Cosmology*. Oxford University Press, 2008.

[Whi11] Nathan Whitehorn. Chasing the Millipede's Tail. `http://anacreon.physics.wisc.edu/~nwhitehorn/millipede-muoncall-20110606.pdf`, June 2011.

[Wos08] Kurt Woschnagg. The New Ice Model AHA. `http://wiki.icecube.wisc.edu/index.php/Aha`, May 2008.

[Wos11] Kurt Woschnagg. Atmospheric Neutrino Fluxes. `http://wiki.icecube.wisc.edu/index.php/Atmospheric_neutrino_fluxes`, November 2011.

[Wos12] Kurt Woschnagg. Coordinate System:. `http://wiki.icecube.wisc.edu/index.php/Coordinate_system`, July 2012.

[WRM08] Xiang-Yu Wang, Soebur Razzaque, and Peter Mészáros. On the Origin and Survival of Ultra-High-Energy Cosmic-Ray Nuclei in Gamma-Ray Bursts and Hypernovae. *The Astrophysical Journal*, 677:432–440, 2008.

[ZK66] Georgiy T. Zatsepin and Vadim Alexeevich Kuzmin. Upper Limit of the Spectrum of Cosmic Rays. *Journal of Experimental and Theoretical Physics Letters*, 4:78, 1966.

List of Figures

List of Tables

Danksagung

An erster Stelle möchte ich Herrn Prof. Dr. Marek Kowalski dafür danken, dass er mir die Möglichkeit gegeben hat, an einem spannenden Thema zu arbeiten und dass er meine Begeisterung für die Astroteilchenphysik geweckt hat. Außerdem möchte ich ihm ganz besonders dafür danken, dass er mir bereits sehr früh ermöglicht hat, die Kollegen in Zeuthen und die restliche IceCube Kollaboration beim Frühjahrsmeeting in Berkeley kennenzulernen. Ich möchte mich zudem bei Herrn Prof. Dr. Jochen Dingfelder dafür bedanken, dass er sich die Zeit für das Zweitgutachten dieser Arbeit nimmt und für die stetige persönliche Betreuung, durch die ich während eines Forschungspraktikums in seiner Arbeitsgruppe viel lernen konnte. Ganz besonders möchte ich mich zudem bei ihm für die kontinuierliche Unterstützung bei allen anderen Fragen und Bitten danken.

Ich möchte den IceCubern meiner Arbeitsgruppe für die kontinuierliche Unterstützung bei allen Fragen und Problemen danken, insbesondere Andreas Homeier, Lukas Schulte und Markus Voge. Unter den Cascaderos aus Zeuthen möchte ich mich ganz besonders bei Eike Middell bedanken, der sich immer die Zeit genommen hat, mir bei Sackgassen auszuhelfen und Probleme ausführlich zu diskutieren. Außerdem möchte ich mich bei den IceCubern aus Madison für die Unterstützung und bereitwillige Beantwortung aller Fragen aus der Ferne bedanken, insbesondere bei Jakob van Santen und bei Nathan Whitehorn. Ganz herzlich bedanke ich mich bei allen Korrekturlesern, insbesondere bei Lukas Schulte, Andreas Homeier, Markus Voge, Sebastian Böser, Alexander Stasik und Richard Hanson. Dank der Verbesserungsvorschläge konnte ich selbst beim Korrigieren der Arbeit noch eine Menge dazulernen. Zuletzt möchte ich Matthias Kerschhaggl danken, ohne den ich den Weg in dieses spannende Forschungsgebiet und in diese Arbeitsgruppe voraussichtlich nicht gefunden hätte.

Ich bedanke mich bei den Sprechern der Bonn-Cologne Graduate School of Physics and Astronomy, insbesondere bei Herrn Prof. Dr. Wermes, für die großartige Unterstützung bereits während des Masterstudiums in Form von zusätzlichen Lehrveranstaltungen, für die Möglichkeit, ein Forschungspraktikum durchzuführen, und für die finanzielle Unterstützung, die mir zum größten Anteil die Teilnahme am IceCube Kollaborationsmeeting in Berkeley ermöglicht hat.

Zuletzt möchte ich mich ganz herzlich bei meinen Eltern bedanken, die mich bis zuletzt über viele Jahre hinweg unterstützt und mir immer großes Vertrauen entgegen gebracht haben. Meinen Freunden danke ich für die großartige Zeit, die ich mit ihnen neben dem Studium teilen konnte. Ich danke ihnen außerdem für die Unterstützung und den Zuspruch für mein Studium, aber auch für die ermahnenden Worte, ab und zu auch mal weniger zu arbeiten. Ein großes Dankeschön gilt zudem meiner Mutter und meinem Bruder für ihre bereitwillige Unterstützung in den stressigen letzten Tagen des Studiums.

Eigenständigkeitserklärung

Ich versichere, dass ich diese Arbeit selbständig verfasst und keine anderen als die angegebenen Quellen und Hilfsmittel benutzt sowie die Zitate kenntlich gemacht habe.

Bonn, den 27. September 2012 Marcel Usner